8-2022

Use of a Trial Function Method to Semi-analytically Simulate Matrix Diffusion in Heterogeneous and Fractured Media

Kien Trung Pham
Clemson University, kienpham89@gmail.com

Use of a trial function method to semi-analytically simulate matrix diffusion in heterogeneous and fractured media

---

A Dissertation
Presented to
the Graduate School of
Clemson University

In Partial Fulfillment
of the Requirements for the Degree
Doctor of Philosophy
Environmental Engineering & Earth Sciences

---

by
Kien T. Pham, P.E.
August 2022

Accepted by:
Dr. Ronald W. Falta, Committee Chair
Dr. Larry Murdoch
Dr. Kevin Finneran
Dr. Joe Rossabi

DEDICATION

Con xin kính tặng luận án Tiến sĩ này làm quà tri ân mẹ Bích, bố Cương, chị My, anh Mykel, vợ Trương Siêu và gia đình hai họ Phạm-Vũ. Sáu năm đèn sách thật dài nhưng con đã đi được hết quãng đường này nhờ sự ủng hộ toàn tâm toàn lực của bố, mẹ, và gia đình. Con tự hào khi được tiếp nối truyền thống khoa bảng của cụ tổ nhà họ Phạm, Chiêu Hổ tiên sinh Phạm Đình Hổ.

To Steve, my American dad, who was emotionally moved when I decided to do a PhD, who always knows the value of education, and who at times believed more in this journey than I did .

To my wife Chao, who heard about the trials and tribulations of this dissertation as much as my advisor, who kept me well-fed in the final stages of my dissertation, and who forgave my long hours at work.

To those immigrants who are pursuing the highest degree in a country that is yet to be their home.

Acknowledgments

I am the author of this dissertation but after these acknowledgements you will not find the use of the pronoun "I" again. It is "we" from here on because none of the work would have been possible without the guidance of my advisor, Dr. Ronald W. Falta. He is the one with the vision, with the technical leadership and the one who acquired the funding that made this dissertation possible. As a part of our research team, I have to thank Noelia Muskus, a fellow researcher and a friend, whose 3-D heterogeneous numerical models kick-started my own research in the subject.

I acknowledge the participation of my committee members. I thank Dr. Larry Murdoch, for teaching me how to relate flow and transport to the basic principles of mass conservation and continuity. Larry expanded my knowledge on the shortcoming of the dual-porosity model using dimensionless parameters and from his detailed comments on the first draft of this dissertation, I have become a more concise communicator of science. I want to thank Dr. Kevin Finneran for noticing my work ethics in his classes and appreciating it enough to be on my committee while modeling is perhaps not his favorite research subject. The knowledge that Kevin imparted on me about in-situ bio-remediation makes me not only a better researcher but also a more well-rounded consultant. Finally, I want to thank Dr. Joe Rossabi, who meticulously commented on my research proposal, an earlier version of this dissertation. Joe's PhD journey set an example of how to succeed during and after working in the Falta's Research Group. I have made unsolicited calls to Joe for his knowledge about the remediation industry and have had drinks on his tabs at many hydrogeological symposiums. Joe is not only a committee member but also a mentor whom I will continue to rely on as I join him in Raleigh, North Carolina.

I acknowledge the support from the Department of Environmental Engineering and Earth Sciences. They provided me with a well-positioned workspace in the middle of the Clemson campus, a few doors down from Ron, which made a big difference for my progress. Dr. David Freedman, the Chair, has proved to me early on that he has got my back when it comes to resources and administrative support. I thank Briana Peele, the office manager of the department in Brackett Hall, who was rarely unable to allocate resources to answer my questions. I thank Lori Alexander for her assistance in ordering equipment when Ron and I needed.

Prior to Clemson, I was fortunate to have influences who steered my career toward environmental engineering and toward research. The first is Dr. Brian Swenty at the University of

Evansville. Dr. Swenty instilled in me the importance of licensure, and he is the reason why I took the PE exam before becoming a PhD student. Dr. Swenty is my first research advisor, and our research project on eutrophication at Hoehn Lake truly began my research interest in environmental problems. Dr. Chris Hochwender is the other influence who first taught me about CERCLA and RCRA, the two pieces of legislation that created the professional field I am working in today. At Arcadis, I have to thank Alain Hebert, who supported my decision to leave consulting and pursue a graduate degree. As a Senior Vice President, he was able to ensure I transitioned smoothly from the many projects I had at Arcadis to graduate school. He is truly the manager everyone wishes to have.

Other than the mission to advance the science, I hope to make the people whom I have got to thank proud of the work I am about to present.

Contents

List of Tables

List of Figures

Chapter 1

General Introduction

Groundwater, an important natural resource, can be impacted by anthropogenic contaminants that reach the subsurface. Matrix diffusion is a subsurface transport process that often controls the time to reach clean-up goals for groundwater at many contaminated sites. When a contaminant mass first enters groundwater, it moves under the influence of advective and dispersive processes. Simultaneously, where low-permeability (low-K) material is present, the mass diffuses into the low-K material and remains there until a remedial action or natural attenuation causes the concentration to be higher in the low-K material than in the high-permeability (high-K) one. At that point, the mass diffuses out of the low-K material in a matrix diffusion process (Freeze & Cherry, 1979; Gillham et al., 1984; Mackay & Cherry, 1989). Matrix diffusion can be much slower than advection, and it is this trickling release of the contaminant mass from the low-K material that can keep the dissolved concentration in the groundwater above regulatory standards for decades (Mackay & Cherry, 1989; B. L. Parker et al., 1994; Esposito & Thomson, 1999; Chapman & Parker, 2005; B. L. Parker et al., 2012; Seyedabbasi et al., 2012; Sale et al., 2013)

To effectively manage groundwater at a contaminated site, stakeholders need the capability to accurately predict the movement of the contaminant mass as it undergoes matrix diffusion. This dissertation focuses on an equivalent porous media (EPM) approach to achieve that objective. The EPM approach simulates diffusion between high-K and low-K materials using an equivalent gridblock where the heterogeneities are defined using bulk properties. The alternative is to utilize a fine numerical mesh, where materials of contrasting permeabilities are explicitly specified, and matrix diffusion is simulated by maintaining a small length scale. The EPM approach is compelling because

models of this type are not created on a fine discretized grid. While EPM models tend to run more efficiently than numerical models with a fine mesh, their accuracy depends on how they approximate matrix diffusion (Long et al., 1982; Pankow et al., 1986; Berkowitz et al., 1988; Schwartz & Smith, 1988; McKay et al., 1993; Falta & Wang, 2017; Muskus & Falta, 2018; Pham & Falta, 2022).

One of those EPM models is the semi-analytic trial function model (Falta & Wang, 2017; Muskus & Falta, 2018), which is also the modeling engine behind the toolkit REMChlor-MD (Farhat et al., 2018). The name of the model refers to the use of a trial function from heat conduction (Vinsome & Westerveld, 1980) to analytically solve for the concentration in the low-K material using the concentration in the high-K material, which is simulated numerically. The analytical trial function is updated at every timestep and in every gridblock with discretization only in the high-K domain. The semi-analytic model resolves the matrix diffusion mass flux using the gradient of the trial function and then, it adds the flux as a source/sink term in the traditional advection-dispersion equation, which can be solved using routine numerical methods. The hypothesis underlying this dissertation is that the semi-analytic model is an efficient and accurate model to simulate matrix diffusion.

The dual-porosity model is the other EPM model of focus in this dissertation. Researchers have used the dual-porosity model since the 1960s to explain non-Gaussian tracer breakthrough curves in porous media cores (Barenblatt et al., 1960; Deans, 1963; Coats & Smith, 1964). The model divides the modeling domain into a mobile subdomain, where advection and dispersion are dominant, and an immobile one, where only diffusion is active. The dual-porosity model moderates the mass transfer between the mobile and the immobile domains by using a first-order mass transfer coefficient. Implicit within the use of this coefficient is the assumption that matrix diffusion can be simulated using a linear driving force model. Researchers have highlighted the shortcoming of that assumption (Adams & Gelhar, 1992; Boggs et al., 1992; Haggerty & Gorelick, 1995; Feehley et al., 2000; Guan et al., 2008), and we further study that limitation of the dual-porosity model in this dissertation.

We compare the effectiveness of the semi-analytic trial function model and the dual-porosity model, in a series of three manuscripts. In the first manuscript (Chapter 2), accepted for publication by the journal *Advances in Water Resources*, we compare the two EPM models in a system of parallel fractures, where an analytical solution by Sudicky and Frind (1982) is used as a benchmark. In the second manuscript (Chapter 3), to be submitted in collaboration with Dr. Beth Parker's research

group at the University of Guelph, we establish the utility of the semi-analytic model relative to the dual-porosity model in 2-D and 3-D discrete fracture networks (DFNs). The DFNs are generated and transport simulated in a finely discretized numerical model called HydroGeoSphere (Therrien & Sudicky, 1996; Aquanty Inc., 2021). In the third manuscript (Chapter 4), we compare the semi-analytic model and the dual-porosity model in two granular material distributions generated by using a transitional probability geostatistical software called TPROGS (Carle, 1999). The transport for those material distributions is simulated using a fine-grid MT3DMS model (Zheng & Wang, 1999). In addition to testing the semi-analytic model in various settings, we also evaluate an option to improve this model by using a variable diffusion area in Chapter 5.

Chapter 2

Parallel Fractures

2.1 Introduction

Groundwater is susceptible to a variety of contaminants, including chlorinated solvents and per- and polyfluoroakyl substances. Those contaminants often form extended dissolved plumes that persist for several decades following their release (Mackay & Cherry, 1989; B. L. Parker et al., 1994, 1997; Esposito & Thomson, 1999; O'Hara et al., 2000; C. Liu & Ball, 2002; Falta, 2005; B. L. Parker et al., 2008; Sale et al., 2013). A primary cause of plume persistence is a process known colloquially as matrix diffusion, whereby a contaminant diffuses from low-permeability zones to high-permeability zones during a loading period (Chapman & Parker, 2005; B. L. Parker et al., 2008). In the loading period, the contaminant is released and moves by advection through relatively high permeability zones and diffuses into relatively low permeability zones. When clean water flows through the high-permeability zones in an unloading period, the concentration gradient reverses, causing diffusion from the low permeability matrix back into the high permeability zone. The word "matrix" in this process refers to the low-permeability rock adjacent to a permeable fracture. However, matrix diffusion can be used more generally to describe the mass transfer between zones of contrasting permeability. For example, in a sand aquifer, the matrix can be a clay or silt lens. Matrix diffusion is particularly important in highly heterogeneous saturated zones, where the porosity of the low-permeability areas can be larger than the porosity of the high-permeability material, allowing the contaminant to be loaded in large volume in the matrix (B. L. Parker et al., 1994; Ball et al., 1997; B. L. Parker et al., 1997; Esposito & Thomson, 1999; B. L. Parker et al., 2004, 2008; Rasa et al.,

2011).

2.1.1 Previous analytical approaches

Analytical solutions capable of simulating matrix diffusion are available for a single fracture (Tang et al., 1981), discrete-multiple parallel fractures (Sudicky & Frind, 1982), and a well-mixed layered sand-silt system (Sudicky et al., 1985) with nonreactive and reactive tracers (Starr et al., 1985). The analytical solution for a single fracture (Tang et al., 1981) was recently expanded by allowing for variable advective velocity and dispersion in multiple fracture channels (L. Liu et al., 2018) . A response function was used to specifically capture the fine-scale mass exchange between the fracture and the matrix in cases when the Peclet number is large and diffusion is limiting. However, in exchange for improvements to the single fracture solution, the solution using the response function only works for non-sorbing solutes and at high flow rates (L. Liu et al., 2018). Two-dimensional (2-D) analytical solutions are available for systems consisting of two semi-infinite high-permeability and low-permeability layers (Sale et al., 2008; Farhat et al., 2012). In the case when a finite source exponentially depletes from aquitards bounded by no flux boundaries, a one-dimensional (1-D) analytical solution for both the loading and unloading periods showed good correspondence with experimental data during the loading of the source and after complete source depletion (Yang et al., 2019).

Analytical solutions give exact concentration profiles efficiently but a new solution needs to be developed whenever the geometry or boundary condition changes.

2.1.2 Dual-porosity model to simulate matrix diffusion

An alternative to utilizing analytical solutions is to simulate matrix diffusion using numerical models with spatial and temporal discretization. Numerous researchers succeeded at using this type of fine-grid numerical model to capture heterogeneity and matrix diffusion at a small scale (Pruess, 1985; B. L. Parker et al., 2008; Chapman et al., 2012; Sale et al., 2013; Farhat et al., 2020). Among the numerical codes available, MT3DMS is a popular choice in the United States, capable of modeling the advective, dispersive and diffusive transport of multiple species (Zheng & Wang, 1999). MT3DMS has gained wide use because it is directly compatible with the three-dimensional (3-D) finite-difference groundwater flow model, MODFLOW, developed by the U.S. Geological Survey

(Harbaugh, 2005). Typically, one uses MODFLOW to generate steady-state or transient flow fields and then, uses MT3DMS to simulate the transport of the solute within a flow field. To specifically tackle matrix diffusive systems without spatial and temporal discretization, Zheng and Wang (1999) included an option to simulate solute transport using a dual-porosity model.

The dual-porosity model is conveniently embedded in MODFLOW/MT3DMS numerical codes, is mathematically intuitive, and is numerically efficient. The dual-porosity model was proposed as an alternative modeling approach to capture the tailing and asymmetry of effluent concentration profiles which the classical ADE could not simulate (Deans, 1963; Coats & Smith, 1964). Conceptually, the model separates the subsurface into two domains. In one domain, transport is advectively mobile while in the other, it is assumed to be stagnant or immobile. The interaction between the two domain is dominated by molecular diffusion, which is treated as a mass transfer process and moderated by a first-order mass transfer coefficient (Deans, 1963; Coats & Smith, 1964; Zheng & Wang, 1999; Zheng & Bennett, 2002). The mass transfer coefficient circumvents the need to spatially discretize the grid to capture matrix diffusion, which allows a numerical dual-porosity model to run more efficiently than others. The dual-porosity transport equations are given in Section 2.2.1.

The first-order mass transfer coefficient is the crux of the dual-porosity model and perhaps its primary weakness. The coefficient is a challenging parameter to quantify (Haggerty & Gorelick, 1995; Perina, 2022). Researchers have attempted to analytically express the mass transfer coefficient using physical parameters (de Vries et al., 2017) or to approximate it based on integral transformation using infinite series (Rao et al., 1980) and moment analyses (J. C. Parker & Valocchi, 1986; Goltz & Roberts, 1987). Several empirical formulas to estimate the mass transfer coefficient using physical properties of the porous media are available (Swami et al., 2018). A notable effort was taken by van Genuchten (1985) to define the mass transfer coefficient for platy, columnar, and prismatic aggregate systems. van Genuchten (1985) utilized geometry-dependent shape factors and known analytical solutions of transport between aggregates of simple shapes such as spherical, cylindrical, and rectangular aggregates to derive first-order mass transfer coefficients of more generic aggregate systems. The result is a first-order rate expression for generic aggregates that has equivalent diffusion characteristics to the expression for the simpler shapes. An expression of the first-order mass transfer coefficient based on van Genuchten (1985)'s efforts was shown to produce accurate results in one system of parallel fractures (Neville, 2006), where the fracture spacing was small and only the

loading period was considered. We are not aware of previous works in the literature where the time-dependency of the dual-porosity's mass transfer coefficient is tested over both loading and unloading periods of diffusion and over a range of fracture spacing. Generally, with the exception of simple geometries as van Genuchten (1985) evaluated, the mass transfer coefficient does not have a direct physical interpretation and has been treated as a calibrating parameter (Neville, 2006).

One of the most influential studies of the mass transfer coefficient is the series of macrodispersion experiments (MADE) at the Columbus Air Force Base in Mississippi, where the dual-porosity model was used to simulate the observed field data. The site is highly heterogeneous, with significant variance in hydraulic conductivity and with preferential flow paths present among low-permeability silt and clay lens (Adams & Gelhar, 1992; Boggs & Adams, 1992; Boggs et al., 1992). Feehley et al. (2000) applied the dual-porosity model to qualitatively replicate the 3-D tritium tracer plumes at the MADE site. When they applied a high mass transfer coefficient to simulate the plume mass, they were able to match the observed relative mass closer to the source but were unable to match the observed data further downstream. The opposite happened when they applied a low mass transfer coefficient because the low mass transfer coefficient caused the dual-porosity model to underestimate the relative mass closer to the source. Guan et al. (2008) explored this behavior further and concluded that the mass transfer coefficient is time-dependent, and it changes with the location of the evolving tracer plume.

Solute movement through layered porous media was tested in 30 sets of tank experiment readings (Swami et al., 2018). The experiment confirmed that a single mass transfer coefficient produced breakthrough curves matching observed data at some cross sections downstream but not all. When the mass transfer coefficients were averaged at different locations using an asymptotic distance-dependent relationship, the fit of the dual-porosity model to the observed data improved. In another recent effort, a 3-D analytical solution to the dual-porosity model with first-order reactions and sorption was developed (Perina, 2022) . Similar to previous analytical approaches, assumptions to the model domain simplify the mass transport equations and make them solveable via Laplace transforms and inverse Fourier transforms. The analytical solution is sensitive to the volume of mobile materials present, especially when the mass transfer coefficient is low (Perina, 2022). The time-dependence of the mass transfer coefficient in the dual-porosity model can likely be overcome by using multiple mass transfer coefficients and/or multiple volume weighted porosities for the low-permeability zones (Haggerty & Gorelick, 1995). Given the difficulty in defining a single mass

transfer coefficient and the lack of the multi-rate model implementation in popular numerical codes, these approaches have not been often utilized in practice.

Developments in applied mathematics recently have offered researchers an alternative to the classical ADE by using fractional derivatives and fractal dimensions (Allwright & Atangana, 2018; Allwright et al., 2021). A fractional derivative is an operator that does not follow the usual integer-order. Integer-order derivatives can only capture the change of a function over one quantity whereas a fractional derivative can represent the change of multiple quantities in a fractal space (Allwright & Atangana, 2018). Direct applications of fractal calculus to the dual-porosity model have been limited to flow models (Xu et al., 2016, 2017; Herrera-Hernández et al., 2018), and not mass transport, except for a specific case of cylindrical two-zone medium (Khuzhayorov et al., 2020). The dual-porosity concept was circumvented completely in one case (Allwright et al., 2021), and fractal derivatives were adapted directly to the 1-D classical ADE. In place of the mass transfer coefficient, a fractal dimension parameter and a fractal order were used to moderate various degree of diffusion. The newly developed fractal ADE can only be solved numerically (Allwright & Atangana, 2019). While this novel fractal advection-dispersion model is promising, it can only simulate 1-D mass transport at the moment, which limits its application in full-scale field tests. In sensitivity analyses of the model, the model was highly sensitive to the fractal parameters, showing a few tenths variation in the fractal dimension can lead to exponential change in advection and dispersion of the solute. Adding to the challenge of calibrating the fractal model is the disconnect between the two fractal parameters and the usual hydrogeological field data that are typically utilized to characterize the subsurface.

2.1.3 Semi-analytic model

The reason the dual-porosity model is such a compelling approach is because it is not constrained to the assumptions of analytical solutions, and the underlying concept of separating the local diffusive flux from the rest of the mass fluxes is intuitive. The model is also easily accessible via the numerical code MT3DMS, which is often packaged with MODFLOW in a single convenient user interface (Aquaveo, 2019). However, its mass transfer coefficient is challenging to estimate and scale-dependent in space and time.

There is a need for an alternative that can capture matrix diffusive effects as efficiently as the dual-porosity model while not relying on the first-order time-dependent mass transfer coeffi-

cient. The alternative we evaluate here is a semi-analytic model that was originally developed by petroleum engineers to compute conductive heat flux from a permeable reservoir to an impermeable caprock (Vinsome & Westerveld, 1980). The model combines analytical and numerical modeling by only numerically discretizing the high permeability zones in the aquifer while solving for the conductive heat flux semi-analytically using a temperature dependent source/sink term computed in each gridblock and at every time step (Vinsome & Westerveld, 1980; Pruess & Wu, 1988, 1993). Observing that heat conduction is analogous to contaminant diffusion, Bear et al. (1994) and Falta and Wang (2017) adapted the method to simulate transient matrix diffusion of contaminants in semi-infinite low-permeability layers. Muskus and Falta (2018) expanded the method's capability to simulate finite embedded heterogeneities. The current implementation of the model has been successfully tested in both heterogeneous and fractured aquifer systems, and in cases where multiple solutes undergo first-order parent-daughter decay reactions.

We are motivated to study the semi-analytic model's ability to approximate matrix concentration in parallel fractures of varying spacing and how it compares to the dual-porosity model in the same setting. A well-known analytical solution for parallel fractures is available to be utilized as a benchmark (Sudicky & Frind, 1982). Testing the semi-analytic model in parallel fractures is an important first step before the model can be tested in more complex fractured systems such as discrete fracture networks (Chapter 3) and 3-D parallel fractures (Chapter 5).

This work will be organized as follows: in Section 2.2, we discuss the mathematical structure of the dual-porosity model, including its characteristic diffusion time and introduce the semi-analytic model; in Section 2.3, we describe the methodology and results of the comparison between the dual-porosity model, the semi-analytic model and an analytical solution in cases where the fracture spacing is varied; and in Section 2.4, we show the results of the cases where the decay rates and adsorption are varied.

2.2 Matrix Diffusion Models

2.2.1 Dual-porosity model

2.2.1.1 Coupled transport equations and mass transfer coefficient via shape factor

The dual-porosity model is implemented as an optional feature in MT3DMS to simulate transport in fractured media or highly heterogeneous porous media (Zheng & Wang, 1999). In our simulations, we assumed a homogeneous and constant groundwater velocity field flowing in x-direction with contaminant decay only in the aqueous phase. Given those assumptions, the coupled dual-porosity model equations can be written as (Zheng & Wang, 1999; Zheng & Bennett, 2002):

$$V_f \phi_f R \frac{\partial C}{\partial t} + (1 - V_f)\phi_l R_l \frac{\partial C_l}{\partial t} = V_f \phi_f (D_x \frac{\partial^2 C}{\partial x^2} + D_y \frac{\partial^2 C}{\partial y^2} + D_z \frac{\partial^2 C}{\partial z^2}) - \frac{\partial}{\partial x}(v_x C) - \lambda \phi_f V_f C - \lambda_l \phi_l (1 - V_f) C_l \tag{2.1}$$

$$(1 - V_f)\phi_l R_l \frac{\partial C_l}{\partial t} = \beta (C - C_l) - (1 - V_f)\lambda_l \phi_l C_l \tag{2.2}$$

The subscript l in Equations 2.1 and 2.2 symbolizes parameters of the low permeability domain. Parameters without any subscript or with the subscript f are those of a fracture or a high permeability material. Equation 2.1 relates the mass balance in both the high-permeability and low-permeability domains to the net mass inflows from advective, dispersive, and first-order decay processes. Equation 2.2 describes the rate of the diffusive mass transfer between the two domains. In Equation 2.1, the volume fraction V_f is the ratio of the volume of highly permeable materials to the total volume. This parameter specifies the degree of heterogeneity and is the same parameter that was introduced by Muskus and Falta (2018). The mobile porosity is defined as the product of the volume fraction and the porosity in the high permeability regions:

$$\begin{aligned} \phi_m &= V_{void,f}/V \\ &= V_f \phi_f \end{aligned} \tag{2.3}$$

The equation parameter $V_{void,f}$ represents the volume of the void space in the high-permeability materials whereas V is the total volume of both the low-permeability and high-permeability materials. Unlike the mobile porosity ϕ_m, which is defined over the total volume, the high-permeability porosity

ϕ_f is a material property that describes the actual porosity of the high-permeability materials.

Similarly, the immobile porosity is the product of the volume fraction of the low permeability materials and the porosity in those regions:

$$\begin{aligned} \phi_{im} &= V_{void,l}/V \\ &= (1 - V_f)\phi_l \end{aligned} \tag{2.4}$$

The equation parameter $V_{void,l}$ is defined as the volume of the void space in the low-permeability materials while the parameter ϕ_l describes the actual porosity in the low-permeability materials.

The sum of the mobile and immobile porosity is the total porosity: $\phi_m + \phi_{im} = V_f\phi_f + (1 - V_f)\phi_l = \phi$, which is also the ratio of the total void space in both domains over the total volume. Those porosity definitions are consistent with how Zheng and Wang (1999) had defined them previously. The retardation factors in the low permeability and high permeability materials are R_l and R. Retardation factors are utilized to account for the effects of sorption in the mass balance. The aqueous mass concentrations in the low permeability and high permeability materials are C_l and C. The 3-D dispersion coefficients are D_x, D_y, and D_z. Those coefficients control the horizontal, vertical, and transverse spread of the contaminant in porous media. The x-direction Darcy velocity is v_x, which is a volumetric flux of water. The first-order decay rates in the low and high permeability materials are λ_l and λ. The decay rates control how fast a contaminant can degrade in the model.

In Equation 2.2, the mass transfer between the two domains is moderated by the mass transfer coefficient β, which is typically utilized as a calibrating parameter by practitioners (Neville, 2006). An approach by van Genuchten (1985) to estimate transport in plane-sheet aggregates using a first-order rate model was used to develop a mathematical expression for β.

van Genuchten (1985) recognized that first-order rate models such as the dual-porosity model can be used to approximate transport in a system of plane-sheet aggregates, which is analogous to a system of parallel fractures. He further observed that the mass transfer coefficient in the dual-porosity model is a function of a shape factor, which was defined as the ratio of the dimensionless time of the parallel fractured system over the dimensionless time of the dual-porosity model. The dual-porosity dimensionless time was found by integrating Equation 2.2 for an initial condition of zero concentration in the matrix and a boundary condition of fracture concentration at unity. The

dimensionless time of the parallel fractured system is known from an analytical solution of heat conduction in a solid bounded by parallel planes (Carslaw & Jaeger, 1959). van Genuchten (1985) observed that when the two dimensionless times are plotted to varying concentration in the matrix, one could glean from the plot a shape factor that would give a dual-porosity matrix concentration equivalent to the analytical matrix concentration. The resulting expression is:

$$\beta = \frac{3\tau_l D\phi_l(1 - V_f)}{(a/2)^2} \tag{2.5}$$

where, τ_l is the tortuosity factor of the low-permeability material. In porous media, the chemical particles undergoing diffusion do not typically follow a linear path so the tortuosity factor is used to account for more realistic channels through which the chemical diffuses. The parameter D is the molecular diffusion coefficient, and a is the fracture spacing. The formula in Equation 2.5 is tested extensively in this work and referred to as the shape factor formula of the first-order mass transfer coefficient.

2.2.1.2 Characteristic diffusion time of the dual-porosity model

From the literature (Feehley et al., 2000; Swami et al., 2018) and from our analysis of the dual-porosity model, it has been observed that the dual-porosity method would work in some cases, such as one system of parallel fractures shown by Neville (2006), but would not work as well in others such as the MADE site (Guan et al., 2008). Bear and Cheng (2010) suggested that the dual-porosity method is only valid when the concentration difference between the fracture and the matrix has reached a quasi-steady state. They gave a mathematical expression of when that steady-state occurs but their formula did not utilize an effective diffusion coefficient. We built on their work by seeking an improved mathematical expression of the characteristic diffusion time for the dual-porosity model.

The derivation of the characteristic diffusion time begins with the governing equation of a solute diffusing into a low-permeability matrix and the dual-porosity equation in the low-permeability domain (Figure 2.1). Boundary conditions are applied to the governing equation so the finite and semi-infinite matrix mass fluxes can be analytically solved. The same boundary conditions are applied to the dual-porosity equation in the low-permeability domain to derive the dual-porosity mass flux. The relationship between the semi-infinite analytical mass flux and the dual-porosity

mass flux results in the characteristic diffusion time. We validate the characteristic diffusion time expression by comparing the analytical mass flux in a finite matrix to the dual-porosity mass flux.

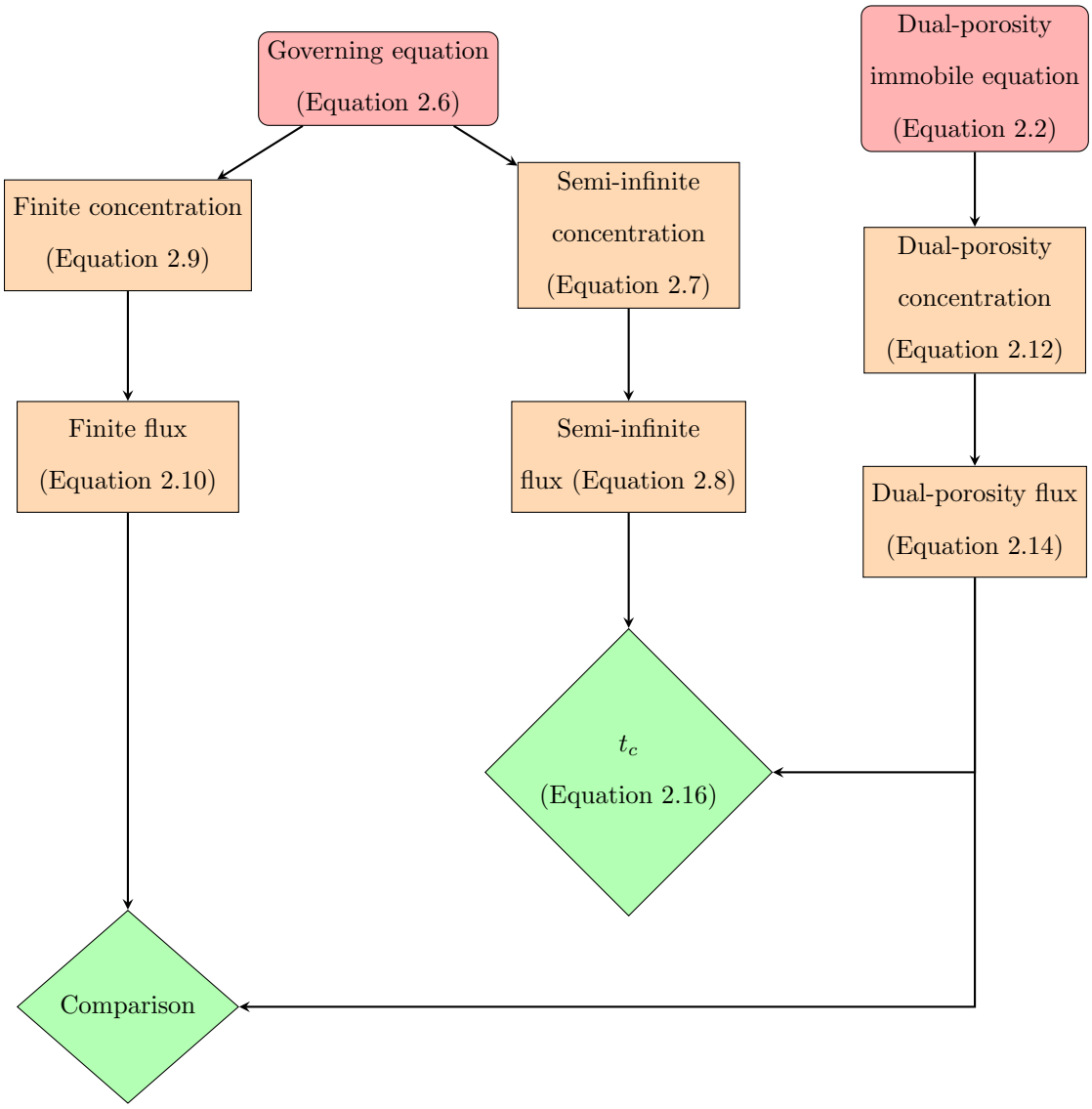

Figure 2.1: Dual-porosity characteristic diffusion time derivation flow chart

Consider a system of parallel fractures where the fracture aperture is b, and a is the fracture spacing (Figure 2.2).

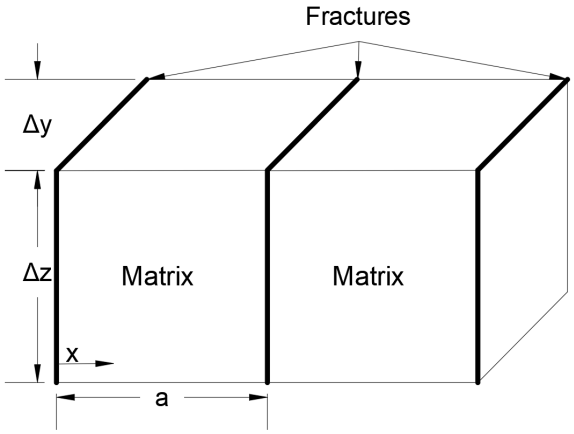

Figure 2.2: A series of vertical parallel fractures.

The fractures are orientated for vertical flow through the fracture apertures but they could be horizontal instead. During an idealized loading period, the aqueous concentration in the fracture is held at a constant concentration C_0. The transient concentration of a chemical diffusing into finite or semi-infinite matrix can be described by the governing equation:

$$R_l \frac{\partial C_l}{\partial t} = \tau_l D \frac{\partial^2 C_l}{\partial x^2} \tag{2.6}$$

When the matrix is semi-infinite, Crank (1975) gave a solution to Equation 2.6, satisfying the initial condition of $C_l = 0$ for $x > 0$ when $t = 0$ and the boundary conditions of $C_l = C_0$ at the matrix-fracture interface ($x = 0$) and $C_l = 0$ at $x = \infty$:

$$C_l^{\mathrm{sf}} = C_0 \mathrm{erfc} \frac{x}{2\sqrt{\kappa t}} \tag{2.7}$$

where $\kappa = \tau_l D / R_l$, and C_l^{sf} is the concentration of a chemical diffusing into a semi-infinite matrix. The equation parameter κ is essentially an effective diffusion coefficient adjusted for sorption and tortuosity. The semi-infinite mass flux F_l^{sf} entering the matrix was found by taking a derivative of Equation 2.7 with respect to x, evaluating it at the matrix interface ($x = 0$), and applying Fick's first law:

$$F_l^{\mathrm{sf}} = \frac{\phi_l \tau_l D C_0}{\sqrt{\pi \kappa t}} \tag{2.8}$$

When the matrix is finite in a system as shown in Figure 2.2, the diffusion of a chemical

into the matrix is analogous to the conduction of heat over a finite region. Powers (1979) provided a solution satisfying the boundary conditions of $C_l = C_0$ at both interfaces of the matrix at $x = 0$ and $x = a$, and an initial condition of $C_l = 0$ when $t = 0$:

$$C_l = C_0 - \frac{2}{\pi}\sum_{n=1}^{\infty}\frac{C_0 - C_0(-1)^n}{n} sin(\frac{n\pi}{a}x)e^{-(\frac{n\pi}{a})^2\kappa t} \tag{2.9}$$

The analytical diffusion mass flux was found by taking the derivative of Equation 2.9 with respect to x and evaluating it at the matrix interface, $x = 0$, and applying Fick's first law:

$$F_l = \frac{2\phi_l\tau_l D}{a}\sum_{n=1}^{\infty}[C_0 - C_0(-1)^n]e^{-(\frac{n\pi}{a})^2\kappa t} \tag{2.10}$$

The semi-infinite mass flux in Equation 2.8 was utilized to approximate the characteristic diffusion time of the dual-porosity model in a finite matrix system. To find the dual-porosity mass flux, we applied the boundary condition of $C = C_0$ in the fracture to the dual porosity mass transfer equation (Equation 2.2), which then becomes:

$$\frac{\partial C_l}{\partial t} = \frac{\beta C_0}{(1 - V_f)\phi_l R_l} - \frac{\beta}{(1 - V_f)\phi_l R_l}C_l - \frac{\lambda_l}{R_l}C_l \tag{2.11}$$

Equation 2.11 is a linear ordinary differential equation that can be solved by applying an initial condition of $C_l = 0$ when $t = 0$ and using the integration factor method, which gives the solution:

$$C_l^{dp} = \frac{\beta C_0}{\beta + \lambda_l\phi_l(1 - V_f)}(1 - e^{-\frac{\beta+\lambda_l\phi_l(1-V_f)}{(1-V_f)\phi_l R_l}t}) \tag{2.12}$$

The dual-porosity mass discharge was found by multiplying the derivative of Equation 2.12 with respect to time with the matrix volume, matrix porosity, and the matrix retardation factor:

$$\begin{aligned}\dot{m}_l = \frac{dM_l}{dt} &= R_l\phi_l(1 - V_f)V\frac{dC_l}{dt} \\ &= \beta C_0 V e^{-\frac{\beta+\lambda_l\phi_l(1-V_f)}{(1-V_f)\phi_l R_l}t}\end{aligned} \tag{2.13}$$

where $V = a\Delta z\Delta y$ is the total volume. The dimension a is used in the x-direction for repeated parallel fractures as shown in Figure 2.2. The dual-porosity mass flux for a finite matrix system

was finally obtained by dividing the dual-porosity mass discharge in Equation 2.13 over the cross-sectional areas of the fracture on both sides of the matrix: $A = 2\Delta z \Delta y$. The dual-porosity mass flux with the mass transfer coefficient expressed via the shape factor formula (Equation 2.5) and with the assumption of no decay is:

$$F_l^{dp} = \frac{6\phi_l(1-V_f)\tau_l D C_0}{a} e^{\frac{-12\kappa}{a^2}t} \tag{2.14}$$

Setting Equation 2.8 equal to Equation 2.14, squaring both sides and isolating the time variable yields an expression that can be solved for the time when the two solutions match:

$$te^{-24\kappa t/a^2} = \frac{a^2}{36\pi\kappa} \tag{2.15}$$

Note that the fracture aperture is typically several orders of magnitude smaller than the fracture spacing so the volume fraction was omitted from Equation 2.15. Equation 2.15 is in the canonical form of the Lambert W function (Corless et al., 1996): $ye^y = x$. For a real number $x \geq 0$, there are two roots to Equation 2.15: $y_1 = W_0(x)$ and $y_2 = W_{-1}(x)$. The smaller root along the principal branch $W_0(x)$ of the Lambert W function is the characteristic diffusion time at which the dual-porosity model using the shape factor formula of the mass transfer coefficient matches the analytical solution:

$$t_c = \frac{-W_0(-2/3\pi)a^2}{24\kappa} \approx \frac{a^2}{85.4\kappa} \tag{2.16}$$

Spatially, for the dual-porosity model, the location of the solute in the matrix relative to the maximum diffusion distance i.e., half the fracture spacing, at the characteristic diffusion time is a dimensionless quantity $2\sqrt{\kappa t_c}/a = 0.22$. So, regardless of the fracture spacing, the parallel fractures system passes the dual-porosity's characteristic diffusion time when the chemical's front has penetrated 22% of the maximum matrix distance. The characteristic diffusion time is shown as a function of fracture spacing from 0.1 m to 10 m in Figure 2.3, using $\tau_l = 0.1$, $R_l = 1$, and $D = 0.0316\ m^2/yr$ (representative of trichloroethylene, TCE).

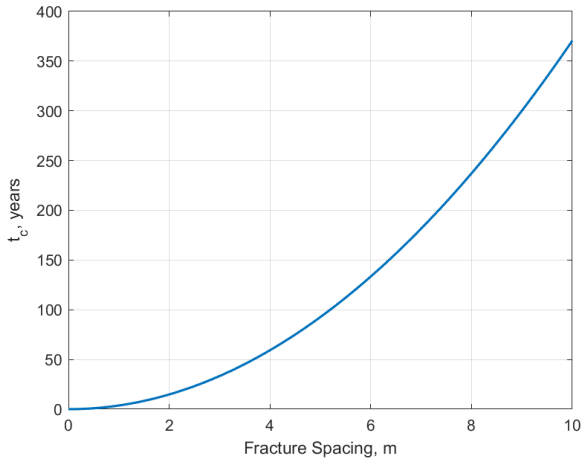

Figure 2.3: Characteristic diffusion time of the dual-porosity model with the shape factor formulation of the mass transfer coefficient in parallel fractures at spacing between 0.1 m and 10 m, for $\kappa = 0.00316\ m^2/yr$.

At fracture spacing less than 1 m, the characteristic diffusion time is less half a month, which is the time for the matrix concentration in the finite matrix to behavior similarly to the concentration in a semi-infinite matrix. When the characteristic diffusion time is fast, the assumptions of the dual-porosity hold. However, the characteristic diffusion time increases as the square of the fracture spacing so when the parallel fractures are far apart, the time to an equivalent semi-infinite matrix concentration can be over 350 years as shown in Figure 2.3 when the spacing is 10 m.

We validated the effectiveness of the characteristic diffusion time expression (Equation 2.16) by comparing the dual-porosity mass flux over a finite matrix region (Equation 2.14) to the analytical solution (Equation 2.10). In Figure 2.4, we show the characteristic time of the dual-porosity method, the analytical solution matrix mass flux, and the dual-porosity mass flux, for three cases of fracture spacing at 0.1 m, 2 m, and 10 m, with $\kappa = 0.00316\ m^2/yr$:

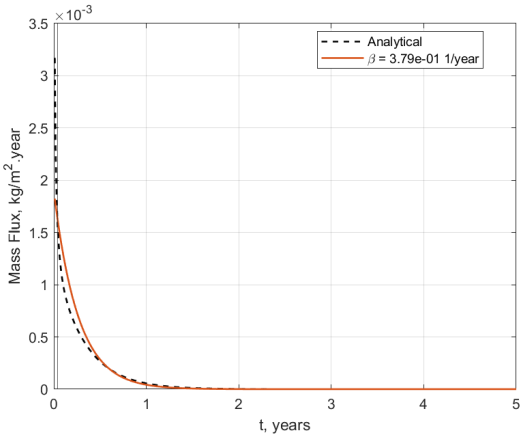

(a) 0.1 m fracture spacing and $t_c = 0.04$ years

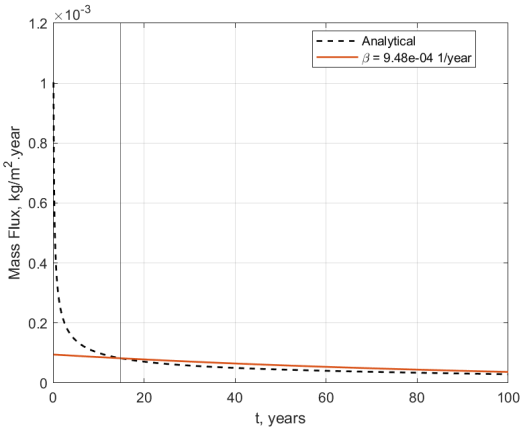

(b) 2 m fracture spacing and $t_c = 15$ years

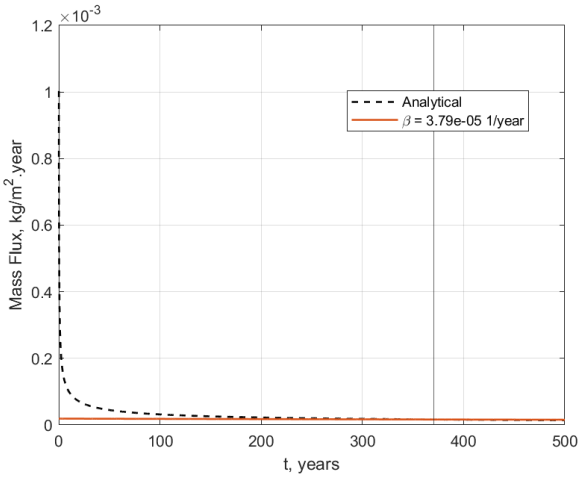

(c) 10 m fracture spacing and $t_c = 371$ years

Figure 2.4: Dual-porosity matrix mass flux (Equation 2.14) compared to analytical solution matrix mass flux (Equation 2.10) in three fracture spacing cases of 0.1 m, 2 m, and 10 m. The characteristic diffusion time is marked by a vertical line crossing the x axis in each fracture spacing case.

The dual-porosity mass flux was computed using the shape factor formula of the mass transfer coefficient (Equation 2.5) and assuming the matrix tortuosity τ_l of 0.1, porosity ϕ_l of 0.1, diffusion coefficient D of 0.0316 m^2/yr and negligible volume fraction V_f. The dual-porosity method (red line in Figure 2.4) is effective at matching the analytical solution (black-dashed line) at the smallest fracture spacing case because the characteristic diffusion time is two orders of magnitude smaller than the total simulation time. As the fracture spacing was increased, the dual-porosity mass flux was only satisfactory at times beyond the characteristic diffusion time. At fracture spacing greater than 10 m, the dual-porosity method cannot simulate the analytical mass flux for at least 371 years, depending on κ.

2.2.2 Semi-analytic trial function model

The semi-analytic trial function model is an adaptation of the Vinsome and Westerveld method in petroleum engineering to compute heat flux from a permeable reservoir to an impermeable rock (Vinsome & Westerveld, 1980; Falta & Wang, 2017; Muskus & Falta, 2018). Muskus and Falta (2018) developed a 3-D finite difference model in Fortran that includes the semi-analytic model, assuming a uniform flow field, called REMChlor-MD. A graphical user interface for the Fortran code is available and can be downloaded free of charge (Farhat et al., 2018).

The semi-analytic model can simulate matrix diffusion into semi-infinite aquitards and into embedded low permeability zones. The method was tested in both heterogeneous porous media and parallel fractures with first-order parent-daughter decay reactions (Muskus & Falta, 2018). For a gridblock of volume V, the method uses three modeling parameters: the volume fraction V_f, the diffusion area A_{md}, and the characteristic diffusion length L_{md}. From a volume balance of the low permeability material, these parameters can be related, reducing the number of unknown parameters to two:

$$(1 - V_f)V = A_{md}L_{md} \tag{2.17}$$

In a system of parallel fractures, no calibration is required for the semi-analytic diffusion parameters because they can be computed directly using the known fracture spacing a and the aperture b. The diffusion length and the volume fraction can be computed as:

$$L_{md} = \frac{a - b}{2} \tag{2.18}$$

$$V_f = \frac{b}{a} \tag{2.19}$$

When the diffusion length and the volume fraction are known, the diffusion area A_{md} can be computed directly using Equation 2.17.

In a heterogeneous porous media system, if the volume fraction of the high permeability materials can be reliably estimated, only either the diffusion area or the characteristic diffusion length is needed to simulate matrix diffusion.

2.2.3 Dimensionless analysis of dual-porosity and semi-analytic trial function models

The time-dependency of the dual-porosity model was studied further in a non-dimensional analysis, where the dimensionless mass stored in a dual-porosity matrix was compared to the dimensionless analytical mass stored in a semi-finite and a finite matrix. This analysis also includes a dimensionless mass stored of the semi-analytic trial function model.

Three dimensionless parameters were used: the dimensionless distance ξ, the dimensionless time T, and the dimensionless concentration Θ.

$$\xi = \frac{x}{\ell} \tag{2.20}$$

$$T = \frac{Dt}{\ell^2} \tag{2.21}$$

$$\Theta = \frac{C_l}{C_0} \tag{2.22}$$

The diffusion distance toward the center of the matrix was scaled to the maximum diffusion distance e.g. half the fracture spacing in a system of parallel fractures, $\ell = a/2$ (Equation 2.20). The dimensionless time was scaled to the characteristic diffusion time of the system, ℓ^2/D (Equation 2.21). Finally, the matrix concentration was scaled to the constant fracture concentration C_0 (Equation 2.22). The effects of porosity, tortuosity, and retardation were not considered in this non-dimensional analysis.

Substituting those dimensionless parameters into the semi-infinite matrix concentration (Equation 2.7) gives a dimensionless concentration:

$$\Theta_{\text{sf}} = \text{erfc}(\frac{\xi}{2\sqrt{T}}) \tag{2.23}$$

Similarly, the dimensionless concentration for a finite matrix was obtained from Equation 2.9 :

$$\Theta_F = 1 - \frac{2}{\pi}\sum_{n=1}^{\infty}\frac{1-(-1)^n}{n} sin(\frac{n\pi}{2}\xi) e^{-(n\pi/2)^2 T} \tag{2.24}$$

For the dual-porosity model, Equation 2.12 was simplified to exclude the effects of decay, porosity, and retardation with the mass transfer coefficient β expressed as the reciprocal of the

characteristic diffusion time: $C_l^{\mathrm{dp}} = C_0(1 - e^{Dt/\ell^2})$. In dimensionless form, the dual-porosity matrix concentration is:

$$\Theta_{\mathrm{dp}} = 1 - e^{-T} \tag{2.25}$$

The three dimensionless concentrations were utilized to compute three matrix mass stored expressions. The matrix mass stored is defined as the ratio of the matrix mass over the cross-sectional area of the matrix: $M/A = C_0\ell^3/\ell^2 = C_0\ell$. The matrix mass stored also equals the integral of the concentration over the matrix domain: $M/A = \int_0^\infty C_l dx$. In dimensionless form, the matrix mass stored for any given concentration is:

$$M^* = \frac{1}{C_0\ell}\int_0^1 \Theta d\xi \tag{2.26}$$

By integrating the dimensionless concentrations of a semi-infinite matrix, a finite matrix, and a dual-porosity model using Equation 2.26, we expressed the dimensionless mass stored for the analytical solutions and the dual-porosity model:

$$M_{\mathrm{sf}}^* = \frac{2\sqrt{T}}{\sqrt{\pi}} \tag{2.27}$$

$$M_F^* = 1 - \frac{8}{\pi^2}\sum_{n=1}^{\infty}\frac{1-(-1)^n}{n^2} sin^2(\frac{\pi n}{4}) e^{-(n\pi/2)^2 T} \tag{2.28}$$

$$M_{\mathrm{dp}}^* = 1 - e^{-T} \tag{2.29}$$

For the trial function model, the matrix concentration is integrated internally for a matrix a^3 in size. To replicate the same constant concentration boundary condition for the comparison, a large Darcy velocity was entered. The volume fraction, diffusion length, and matrix diffusion area were computed Equations 2.17 through 2.19. The trial function matrix mass outputs were normalized by the total mass entering the matrix C_0a^3, and the simulation times were normalized by the characteristic diffusion time ℓ^2/D.

In a plot of the mass stored as function of the dimensionless time, the semi-infinite mass stored (blue line in Figure 2.5) increased at a rate faster than the dual-porosity mass stored (red dashed line in Figure 2.5). This means using the dual-porosity model will yield a higher mobile mass relative to the semi-infinite solution at early times.

The semi-infinite mass stored as a function of dimensionless time followed the finite mass stored curve (yellow line in Figure 2.5) closely for $T < 0.4$.

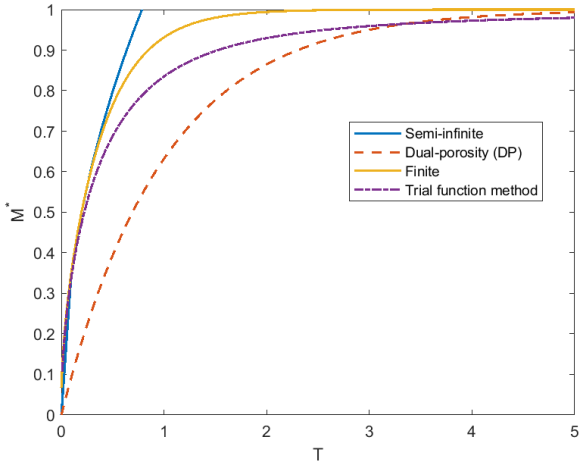

Figure 2.5: Semi-infinite, finite, and dual-porosity mass stored

A relative error was computed to quantify the error between the dual-porosity mass stored and the finite analytical solution: $R = (M_F^* - M_{\text{dp})/M_F^*}$. The dual-porosity model's relative error was less than 0.1 at $T > 2.27$. In a system of large characteristic distance, a large dimensionless time translates to a large simulation time. For a fracture spacing of 4 m and a diffusion coefficient of 0.0316 m^2/yr, the T value of 2.27 corresponds to 287 years, which is longer than a typical transport simulation. For $T < 0.1$ or about 13 years (when $a = 4$ and $D = 0.0316$), the dual porosity model's error was more than 0.75. When the fracture spacing is 0.1 m, the dimensionless time of 2.27 is 0.2 years. In this case where the fractures are closer together, using the dual-porosity model will yield errors less than 0.1 for most of the simulation times.

The semi-analytic trial function method had errors less than 0.04 for $T < 0.1$, nearly 20 times smaller than the dual-porosity model in the same range of dimensionless time. The trial function mass stored deviated from the analytical solution at $T = 0.22$ (relative error of 0.06). The trial function mass stored was also slower to reach the equilibrium mass stored relative to the dual-porosity model. This is likely because the trial function method does not enforce the zero flux boundary condition at the center of the matrix (Muskus & Falta, 2018). The trial function's errors were in the 0.03 range for $T > 4$. Its maximum error over $0 < T < 5$ was 0.11.

The dual-porosity mass stored was calibrated by introducing a parameter ω to the expo-

nential term of the mass stored expression:

$$M^*_{\text{dp}} = 1 - e^{-\omega T} \tag{2.30}$$

Parameter ω adjusts the dual-porosity mass discharge curve similarly to a mass transfer coefficient. When using $\omega = 3$, the dual-porosity model (dashed red line in Figure 2.6) followed the finite analytical solution more closely than the uncalibrated curve over $0 < T < 5$.

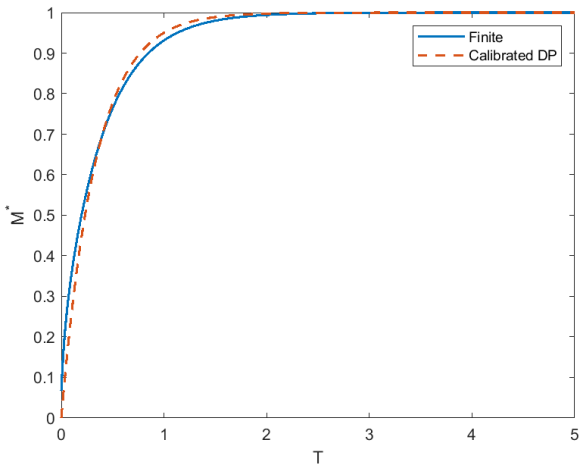

Figure 2.6: Finite and calibrated dual-porosity mass stored

The dual-porosity error was reduced to less than 0.3 for $T < 0.1$ after calibration (red dashed line in Figure 2.7). The error of the calibrated dual-porosity model dropped to 0.02 by $t = 0.5$ and remained in that range for the rest of the dimensionless times. The trial function method had errors lower than the uncalibrated dual-porosity method without any calibration (yellow dashed dotted line in Figure 2.7).

The dual-porosity model is sensitive to changes in the calibrating parameter ω. Reducing ω from 3 (blue dashed line in Figure 2.8) to 0.1 (green dashed line) essentially linearized the mass stored curve. For simulations where the mass stored increased slowly over large range of dimensionless time, it may be necessary to use a small ω value to reproduce the peak mass stored. However, such a small ω may not be able to simulate the non-linear change in mass stored over time.

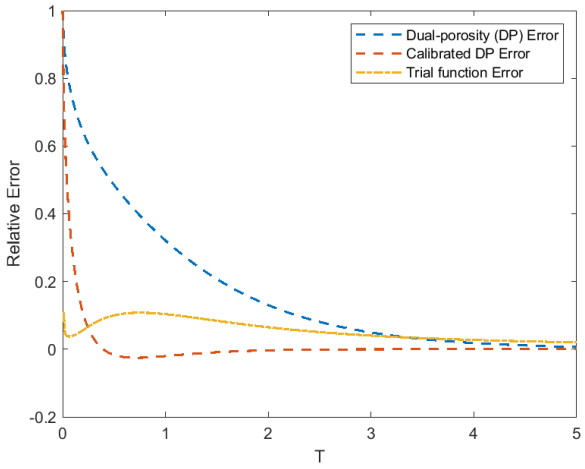

Figure 2.7: Realtive errors of dual-porosity and trial function models

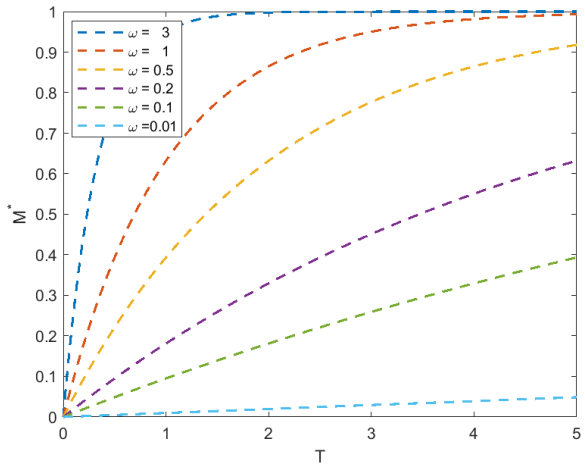

Figure 2.8: Dual-porosity mass stored for a range of ω

2.3 Varying Fracture Spacing Simulations

Muskus and Falta (2018) compared the semi-analytic model against an exact analytical solution for a porous media system of 1-D parallel fractures developed by Sudicky and Frind (1982). They solved a set of coupled equations: one for the advective, diffusive, and dispersive transport in fractures and another equation for only diffusive transport in the matrix. Adsorption and decay are also considered in both equations. Sudicky and Frind (1982) assumed that the fracture aperture is significantly smaller than the length and that complete mixing exists in the fractures. The coupled equations are solved by using Laplace transform and Crump numerical inversion. Sudicky and Frind (1982) coded the solution in a Fortran program called CRAFLUSH, which we used extensively in

the present work. CRAFLUSH has an accompanying program called CRAFIT, which automates the calibration of breakthrough curves from column experiments (Toran, 2000). In a previous test, where matrix diffusion almost completely dominated transport, the semi-analytic model compared favorably with the results from CRAFLUSH (Muskus & Falta, 2018).

In the current work, we have expanded the study of matrix diffusion in parallel fractures by testing a series of scenarios where the fracture spacing, adsorption, and solute decay rates were varied. In those test scenarios, the concentration simulated by the semi-analytic and dual-porosity models were compared to that of the analytical solution (Sudicky & Frind, 1982).

2.3.1 Simulations methodology

A 1-D numerical grid with 200 gridblocks of 1 m long in the x-direction was created. This grid uses an equivalent porous media approximation to represent parallel fractures (Long et al., 1982; Anderson, 1992). A range of fracture spacing from 0.1 m to 10 m was tested but the fracture aperture was fixed at b = 100 μm. The hydraulic conductivity in the fractures was computed to be $2.30 * 10^5$ m/yr using a well-known formula: $K_f = \rho g b^2 / 12\mu$ (Anderson, 1992), where the water density ρ is $1.00 * 10^3$ kg/m^3, the constant of gravitational acceleration g is 9.808 m^2/s, and the dynamic viscosity μ is $3.55 * 10^{-11}$ $N.yr/m^2$ (Munson et al., 2009). The pore velocity in the fracture was held at 100 m/yr. The hydraulic gradient for the system was set at 0.000435, which is the ratio of the velocity to the hydraulic conductivity in the fracture. The material porosity was set at $\phi_l = 0.1$ for the matrix. The mobile and immobile porosities were computed using Equation 2.3 and Equation 2.4.

As the fracture spacing increases, there is more low permeability material in the system so the volume fraction decreases (Figure 2.9). The equivalent porous media Darcy flux is the largest when the fractures are close together and vice versa (Figure 2.10). The largest equivalent porous media Darcy flux was 0.1 m/yr. The equivalent hydraulic conductivity tested ranges from 230.1 m/yr for a fracture spacing of 0.1 m to 2.301 m/yr for a fracture spacing of 10 m.

For each fracture spacing case, the pore velocity is a direct input in the analytical model (Sudicky & Frind, 1982) whereas, the semi-analytic model requires an equivalent porous media Darcy flux as an input. For the dual-porosity model as implemented in MT3DMS (Zheng & Wang, 1999), the Darcy flux is not a direct input so an equivalent flow field was generated first using MODFLOW (Harbaugh, 2005). A total of nine flow fields were simulated, one for each fracture spacing case.

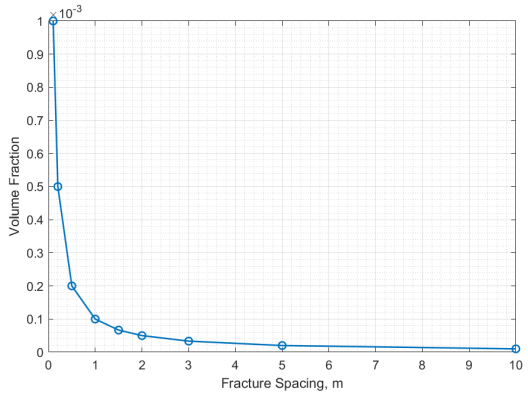

Figure 2.9: Volume fraction as a function of fracture spacing.

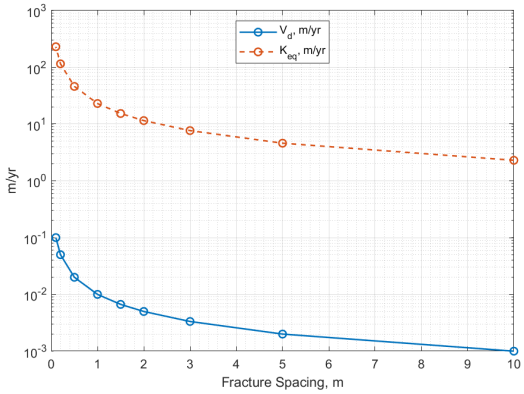

Figure 2.10: Equivalent porous media Darcy velocity and hydraulic conductivity as function of fracture spacing.

Each flow field was then used to simulate an equivalent Darcy velocity in the dual-porosity transport model. A flow field can be simulated in MODFLOW by setting head boundary conditions at the upstream and downstream of each flow model using an equivalent hydraulic conductivity and the same gradient of 0.000435.

After a flow model ran successfully in MODFLOW, a TCE source concentration of 100 mg/l was introduced at the upstream end of the fractured system. Advective loading of the source was enforced by setting the dispersivities in the source cells to a small value. The source was maintained for 50 years at 0.05 years timestep in each fracture spacing model and following complete source removal, clean water was flushed through the system for another 50 years.

A longitudinal plume dispersivity of 0.5 m or half of the gridblock spacing in the x-direction was used in the analytical solution. In the semi-analytic and dual-porosity models, advection terms were solved by the standard finite difference scheme with upstream weighting, which has an inherent numerical dispersivity value of 0.5 m, same as the value used in the analytical model (Sudicky & Frind, 1982).

Initially, neither decay nor adsorption was considered as fracture spacing was varied. Then, simulations were run where the fracture spacing was varied as the solute half-life decreases from a no decay condition to 10 years, 5 years, and 1 year. Finally, simulations were run where the fracture spacing was varied as the retardation factor was increased from 1 (no retardation) to 2 and 5. MODFLOW and MT3DMS models were set up using the graphical user interface Groundwater Modeling System (GMS) developed by Aquaveo (2019).

Table 2.1 summarizes the modeling parameters used for the fractured media experiments:

$0.1\ m < a < 10\ m$

Parameter	**Fracture**	**Matrix**
Fracture aperture, μm	100	-
Porosity	1.0	0.1
Tortuosity	0.1	
Retardation factor	1 or 2 or 5	
Pore velocity, m/yr	100	0
Diffusion coefficient, m^2/yr	0.0316	
Decay rate, $1/yr$	0 or 0.07 or 0.1 or 0.7	
Loading period, yr	50	
Flushing period, yr	50	

Table 2.1: Parameters used in fractured media experiments.

Fracture concentration profiles over distance from the source were plotted at four time periods, which were selected to study the system behavior before and after source removal and at high and low concentration gradients. To quantitatively evaluate the models, the root mean square errors (RMSEs) of the semi-analytic and dual-porosity concentrations in comparison to the analytical solutions were computed at each time period:

$$\text{RMSE}_j = \sqrt{\sum_{i=1}^{n} \frac{(A_i - S_i)^2}{n}}$$

where RMSE_j is the root mean square error for time period j (Singh et al., 2007). A_i is the analytical solution's concentration at a distance x_i. S_i is the simulated concentration of either the semi-analytic or the dual-porosity model, and n is the total number of simulated values along the x-direction. RMSEs at log scale were computed similarly:

$$\text{RMSE}_j\ (\log) = \sqrt{\sum_{i=1}^{n} \frac{[log(A_i) - log(S_i)]^2}{n}}$$

The normalized root mean squared errors (NRMSEs) were calculated by normalizing the

RMSEs by the range of concentrations from the source concentration (highest value) to the typical method detection limit of dissolved TCE, 0.001 mg/L (smallest value). Concentrations below 0.001 mg/L are not considered for analysis.

$$\text{NRMSE}_j = \frac{\text{RMSE}_j}{C_0 - C_{\text{MDL}}}$$
$$\text{NRMSE}_j \text{ (log)} = \frac{\text{RMSE}_j \text{ (log)}}{5}$$

Average NRMSEs of concentration profiles over the four time periods at linear and log scale were computed and are referred to as the marginal NRMSEs:

$$\text{Marginal NRMSE } = \frac{\sum_{j=1}^{4} \text{NRMSE}_j}{4}$$
$$\text{Marginal NRMSE (log)} = \frac{\sum_{j=1}^{4} \text{NRMSE (log)}_j}{4}$$

The average of those values i.e., the average marginal NRMSEs, were calculated for each fracture spacing case and for both the semi-analytic and the dual-porosity concentrations:

$$\text{Average marginal NRMSE} = \frac{\text{marginal NRMSE} + \text{marginal NRMSE (log)}}{2} \tag{2.31}$$

The average marginal NRMSE was used as a single metric to compare the effectiveness of the semi-analytic and the dual-porosity models in various fractured systems and under different conditions of plume decay and retardation.

2.3.2 Results of fractured media simulations

2.3.2.1 Semi-analytic model compared with analytical solution

Because of the simplified geometry of the parallel fractured system, all diffusion modeling parameters of the semi-analytic model were computed directly using Equations 2.17 through 2.19. For the dual-porosity model, the first-order mass transfer coefficient was estimated using the shape factor formula (Equation 2.5). Because the accuracy of the dual-porosity model depends on the characteristic diffusion time, the dual-porosity model was manually calibrated by adjusting the mass transfer coefficient until the lowest average marginal NRMSEs for all time periods was found.

Fracture concentration was simulated over a range of fracture spacing using the semi-analytic model, and the result was compared to the analytical solution.

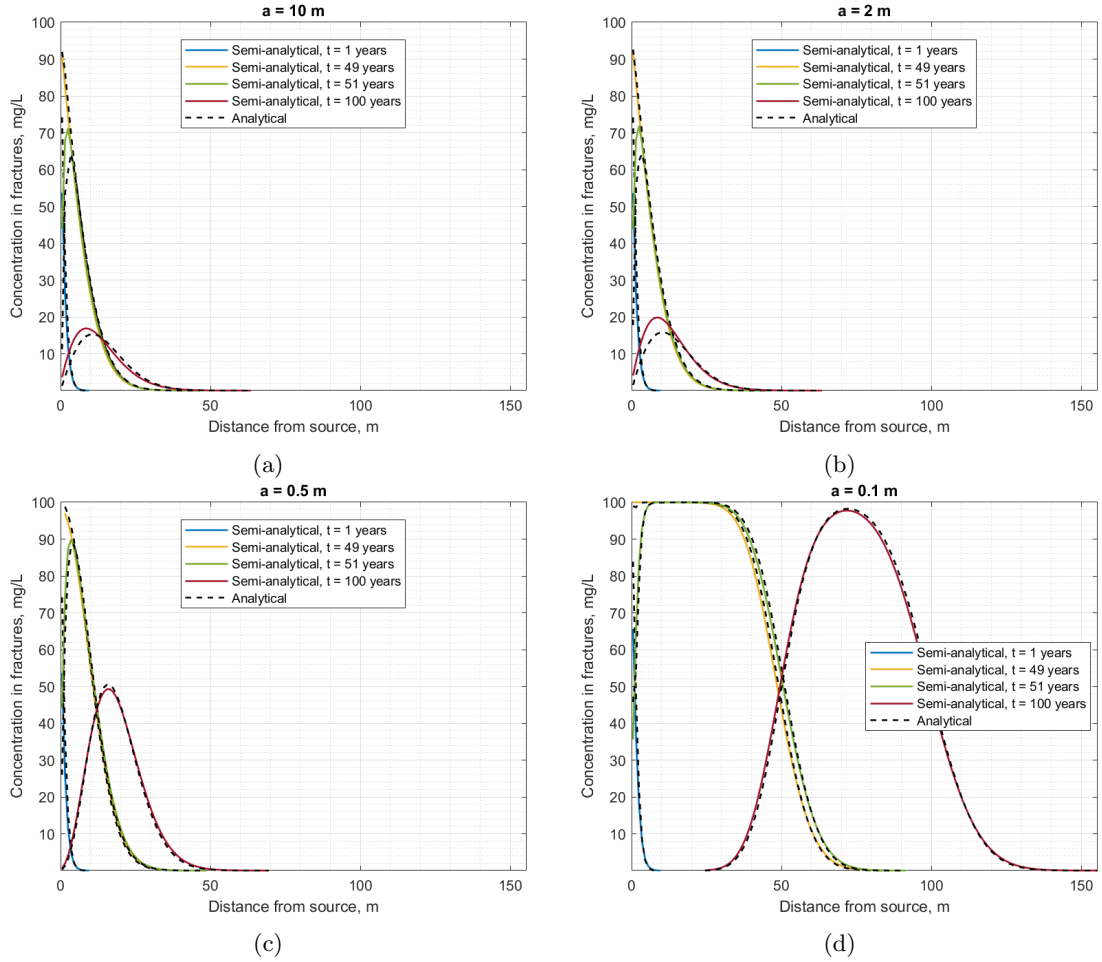

Figure 2.11: semi-analytic concentration profiles compared to analytical solution for fracture spacing a) 10 m; b) 2 m; c) 0.5 m; and d) 0.1 m.

The 1-year profiles (blue lines) of the loading period for the four fracture spacing cases are similar to one another (Figure 2.11). The semi-analytic model was able to match the exponential shape of the analytical loading curve. At 1 year, the longitudinal extents of both the analytical and the semi-analytic concentration profiles were at 10 m from the source in the four fracture spacing cases. At 49 years, the solute has only advanced a few tens of meters in spite of the 100 m/yr pore velocity. When the fracture spacing was 0.1 m (Figure 2.11d), the 49-year profile (yellow line) was similar to the shape of a system with a clear but retarded advective front. In this small fracture spacing case, the solute at source concentration was in the fractures for nearly 40 m before the

concentration dropped (Figure 2.11d). The advective front developed at 50 m from the source as the plume was moving at the apparent transport velocity of 1 m/yr, which is 100 times slower than the pore velocity in the fractures.

In the 51-year profiles (green lines in Figure 2.11), the clean water front is strongly retarded by matrix diffusion. The 100-year concentration profiles (purple lines) showed a rise in concentration in the absence of the source, and their peak concentrations varied inversely with the fracture spacing. At the smallest fracture spacing, the concentration profile resembles advective-dispersive transport with a high retardation factor.

The analysis of the concentration profiles indicates a good match between the analytical solution and the semi-analytic model over a range of fracture spacing. The semi-analytic model overestimated peak concentrations at large fracture spacing cases during the unloading period but as the spacing was decreased, the overestimation was less prominent.

2.3.2.2 Semi-analytic model compared with dual-porosity model

Before comparing the semi-analytic and the dual-porosity results under matrix diffusion, it was verified that the MT3DMS dual-porosity and the REMChlor-MD semi-analytic models produced the same results in the absence of matrix diffusion. The simulation of the matrix diffusion process was isolated from the simulation of other transport processes when comparing the two models.

To remove matrix diffusion effects, the semi-analytic model's matrix diffusion area A_{md} and the dual-porosity mass transfer coefficient β were set to zero.

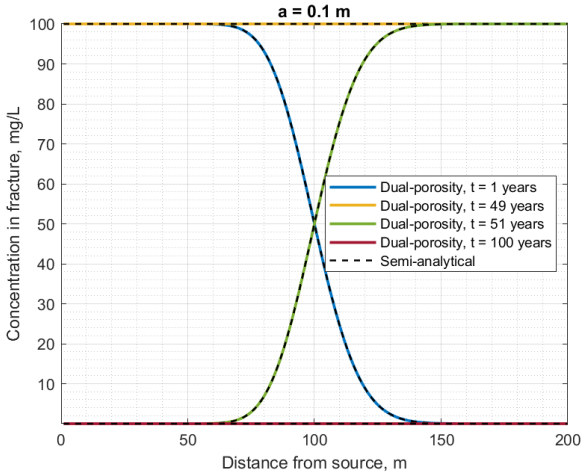

Figure 2.12: MT3DMS dual-porosity and REMChlor-MD concentration profiles without diffusion for fracture spacing of 0.1 m.

After one year, the advective front without matrix diffusion was at 100 m from the source, and it moved downgradient at the pore velocity of 100 m/yr (Figure 2.12). Following source removal, the 51-year profile mirrored the 1-year profile over the y-axis as the system switched from being loaded with a source to being flushed with clean water. In the absence of matrix diffusion, the clean water front also moves at the pore velocity of 100 m/yr.

The semi-analytic and dual-porosity profiles are essentially identical, indicating that the two models only differ in the way they simulate diffusive transport in the matrix. Although only the fracture spacing case of 0.1 m is shown here, the same analysis was repeated for all fracture spacing cases with the same result.

After verifying that the MT3DMS dual-porosity and the REMChlor-MD semi-analytic models produced identical concentration profiles in the absence of matrix diffusion, diffusion was considered in both models. For the semi-analytic model, the matrix diffusion area was changed from zero to a computed value (Equation 2.17). For the dual-porosity model, the mass transfer coefficient was computed first using the shape factor formula (Equation 2.5). Then, additional mass transfer coefficients were tested by trial and error to gauge the effects the coefficients had on the concentration profile and to calibrate a better fit to the analytical solution.

Semi-analytic and dual-porosity models are compared to the analytical solution over four time periods for the largest fracture spacing of 10 m (Figure 2.13).

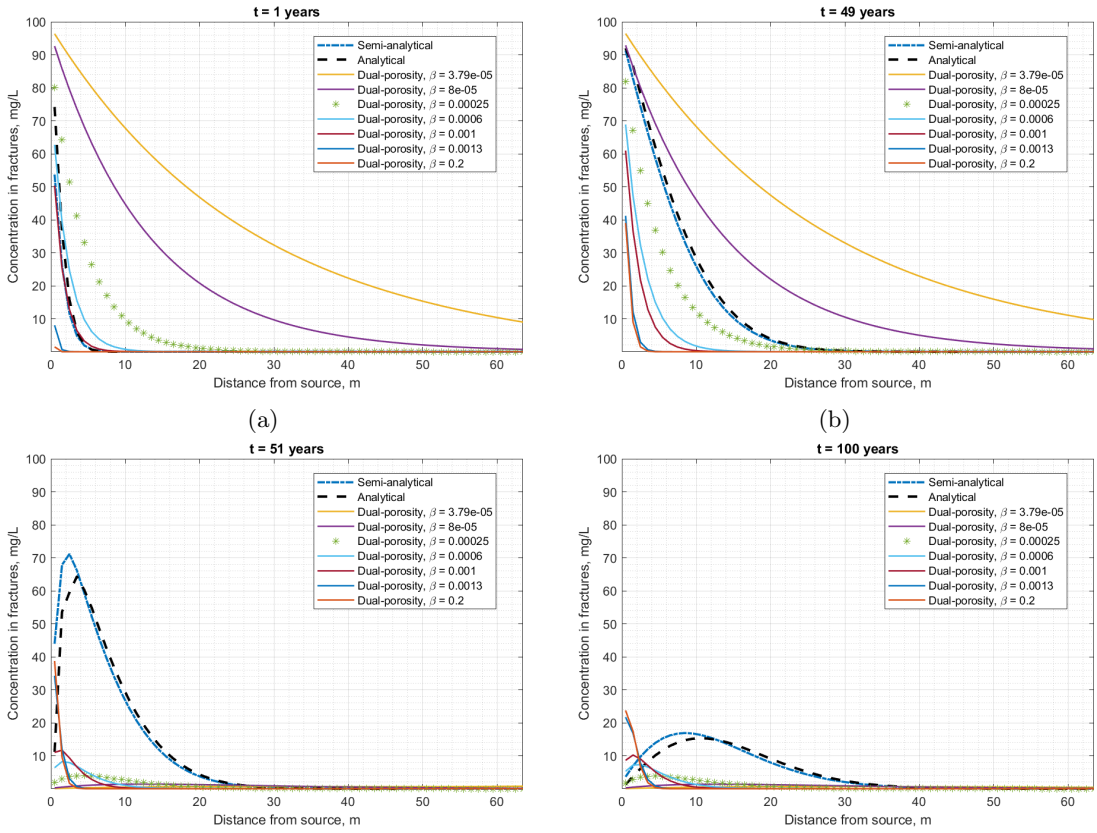

Figure 2.13: Fracture concentrations from dual-porosity, semi-analytic and analytical solutions at fracture spacing of 10 m at a) t = 1 years; b) 49 years; c) 51 years; and d) 100 years.

A high mass transfer coefficient simulates a high rate of mass transfer into the matrix and a low concentration profile. When the mass transfer coefficient was 0.2/yr, the concentration penetrated less than 1 m, causing the orange solid line to be barely visible after one year of source loading (Figure 2.13a). After 49 years, that profile was more visible but it was still the lowest concentration profile (Figure 2.13b). As the mass transfer coefficient was decreased, the dual-porosity concentrations were higher in the loading period because less mass was transferred to the matrix, leaving more mass in the fractures. The unloading profiles are directly related to the mass loading behavior. If a high mass transfer coefficient was used during the loading period, more mass was stored in the matrix and in the unloading period, more mass diffused out from the matrix. The mass transfer coefficient computed via the shape factor formula was unable to produce concentration profiles that match the analytical solution because the characteristic diffusion time of 371 years has not passed in all four time periods under consideration (see Figure 2.3).

Four orders of magnitude change of the mass transfer coefficients were tested via trial-and-error to improve the fit of the dual-porosity concentration profiles. Even after calibration, the dual-porosity model could not match the analytical solution because a calibrated mass transfer coefficient that quantitatively placed the dual-porosity concentrations close to the analytical solution during the loading period was still unable to match the analytical solution during the unloading period. It may not be possible to have one parameter that works for all time periods because the mass transfer coefficient is a time-dependent parameter (Guan et al., 2008). Being only applicable to systems at a certain time makes the dual-porosity model less useful for simulations such as the one being considered here, where the concentration profiles are evaluated over 100 years, with a reversal of the matrix diffusion direction.

For fracture spacing case of 2 m (Figure 2.14), the characteristic diffusion time is only 15 years as compared to 370 years in the 10 m spacing case. After the characteristic diffusion time, the matrix-fracture concentration gradient is no longer steep, and the dual-porosity model is expected to match the analytical solution.

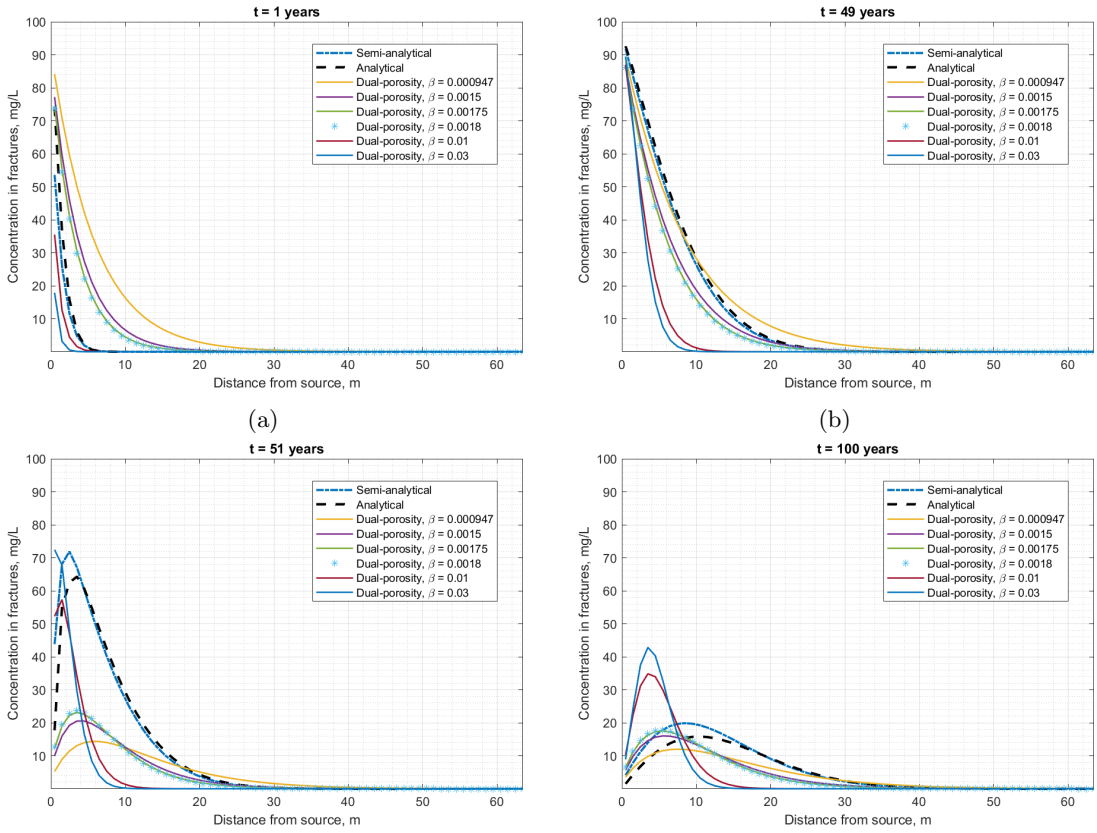

Figure 2.14: Fracture concentrations from semi-analytic, dual-porosity, and the analytical solutions at fracture spacing of 2 m at a) 1 year; b) 49 years; c) 51 years; and d) 100 years. The yellow lines are the concentration profiles produced by the shape factor mass transfer coefficient (Equation 2.5). Cyan asterisks show dual-porosity profiles with the lowest average marginal NRMSEs over four time periods.

Dual-porosity concentrations matched relatively well with the analytical solution at time periods 49 years and 100 years, which are both greater than the characteristic diffusion time of 15 years. The dual-porosity model did not produce concentrations matching the analytical solution at 1 year and 51 years because the characteristic diffusion time, which is reset after the source is removed, had not been reached. The semi-analytic model matched analytical solution well at all time periods.

Calibrations were implemented by trial and error to seek the mass transfer coefficient that gave the lowest average marginal NRMSE. The calibrated coefficient gave concentrations with lower NRMSEs at later times but at early times prior to the characteristic diffusion time, calibration did not reduce the dual-porosity model's errors.

In fracture spacing case of 0.1 m (Figure 2.15), the characteristic diffusion time is short at 0.04 years. In this case, the dual-porosity model matched the analytical solution well at all times.

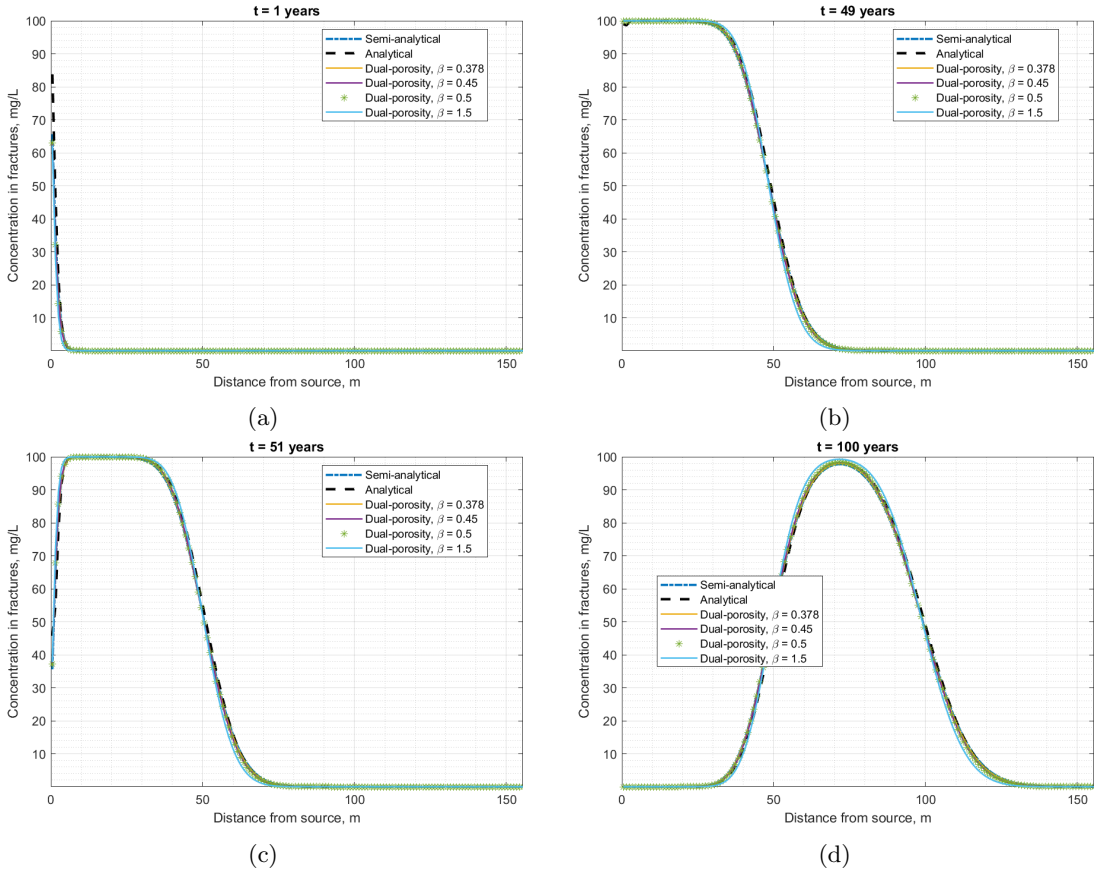

Figure 2.15: Fracture concentrations from semi-analytic, dual-porosity, and analytical solutions for a fracture spacing of 0.1 m at a) 1 year; b) 49 years; c) 51 years; and d) 100 years.

The best fit mass transfer coefficient for this case was 0.5/yr, which is similar to the value of 0.378/yr predicted by the shape factor formula. The dual-porosity model produced concentrations at low errors without calibration when the fracture spacing is at 0.1 m and when the characteristic diffusion time is less than the four time periods of 1 year, 49 years, 51 years, and 100 years. Though not shown here, we plotted the concentration profiles of both models at log scale and observed similar results.

We repeated the concentration profile comparison for other fracture spacing cases in the range between 0.1 m and 10 m. Figure 2.16 summarizes the change of the average marginal NRMSEs for both the semi-analytic and the dual-porosity models over the range of fracture spacing.

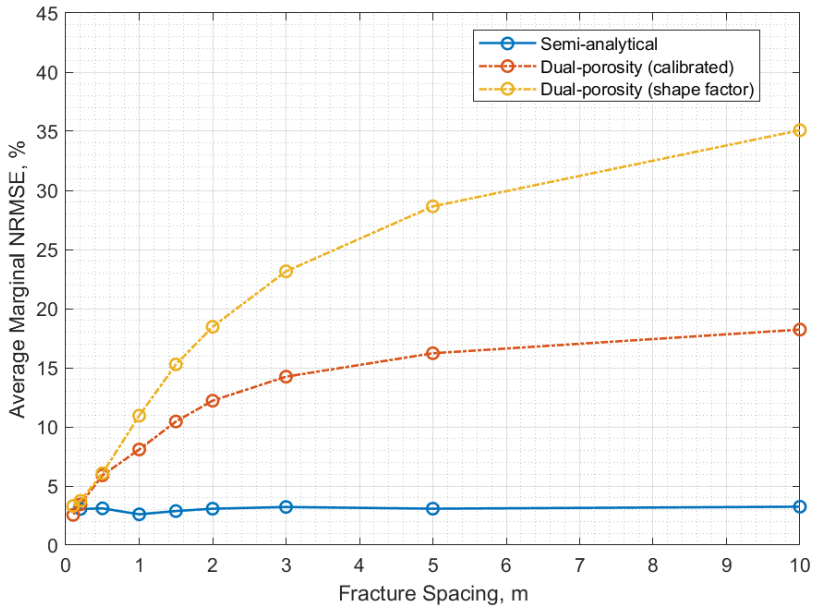

Figure 2.16: Average marginal NRMSEs comparison between the semi-analytic and the dual-porosity models over a fracture spacing range between 0.1 m and 10 m.

The NRMSE values for the semi-analytic model were consistently less than 3.5%. In contrast, the mass transfer coefficient computed by the shape factor formula only produced low NRMSEs at fracture spacing less than approximately 1 m. At the largest fracture spacing, the uncalibrated dual-porosity model produced an NRMSE tenfold that of the semi-analytic model. The effectiveness of the mass transfer coefficient based on the shape factor is limited by the characteristic diffusion time which can only be satisfied at smaller fracture spacing.

Even with calibration, the dual-porosity model's NRMSE could still be five times higher than that of the semi-analytic model in the largest fracture spacing case. Calibration cannot remove the dependency of the mass transfer coefficient on the characteristic diffusion time. While a calibrated mass transfer coefficient perhaps can produce a concentration profile that would work at some time periods, it did not produce a profile that would work at all times, unless the fracture spacing is small, which results in a short characteristic diffusion time relative to the duration of the simulation.

2.4 Simulations with Decay and Adsorption

2.4.1 Varying decay rate

The effects of decay in the same fracture systems were evaluated by reducing the decay rates from a half-life of 10 years to 5 years, and finally to 1 year. We assumed the decay rates in the fractures were the same as in the matrix.

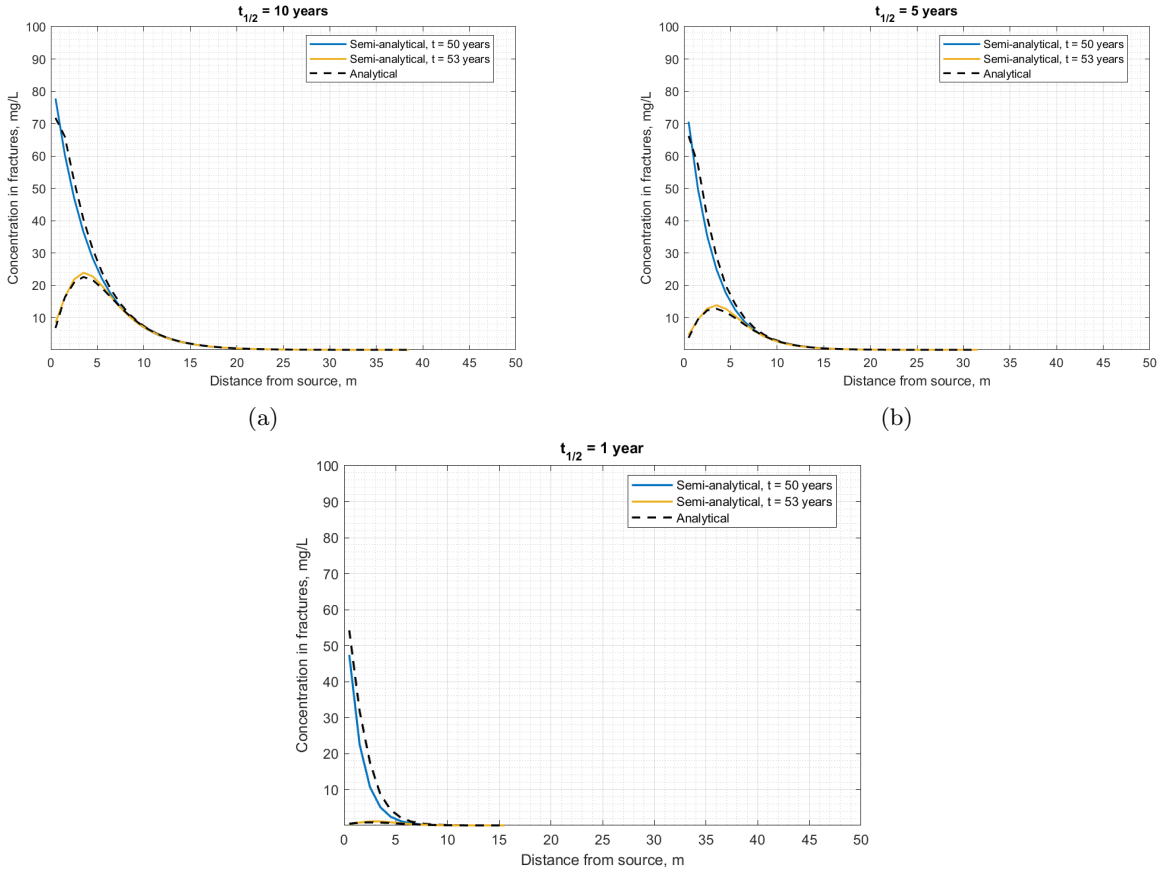

Figure 2.17: Semi-analytic and analytical fracture concentrations when the fracture spacing is 1 m with a) half-life of 10 years; b) half-life of 5 years; and c) half-life of 1 year.

The analytical profiles show the changes of the plume concentration under an increasing decay rate (Figure 2.17). Near the source, the analytical concentration decreased from over 70 mg/l to approximately 55 mg/l as the decay rate was increased from a half-life of 10 years to 1 year. Following the removal of the source, the peak concentration of the 53-year profiles lowered from over 20 mg/l under a slow decay rate to 2 mg/l under the fastest decay rate. The increasing decay rate

also reduced the spatial extent of the contaminant exceeding the detection limit from nearly 40 m from the source to only about 15 m. The semi-analytic model matched the overall shape of the analytical solution well, especially in the unloading period.

Three additional fracture spacing cases of 0.1 m, 5 m and 10 m were simulated with the three decay rates of 10-year, 5-year, and 1-year half-life (not shown). The semi-analytic and the dual-porosity profiles were compared with the analytical solutions, similar to the no decay cases. The semi-analytic model produced concentration profiles under varying decay conditions with low NRMSEs as compared to the analytical solution over a range of fracture spacing. Meanwhile, the dual-porosity model had higher NRMSEs at large fracture spacing. In smaller fracture spacing cases, when the characteristic diffusion time was small, the dual-porosity model's NRMSEs were lower.

The average marginal NRMSEs (Equation 2.31) across the four time periods on linear and log scale were computed for each decay rate. In the case of 1-year half-life decay, concentrations were below 0.001 mg/L within a few meters of distance. In one time period, only four analytical observations were above 0.001 mg/L, a significant reduction in the analytical solution's original sample size of 200 observations. Such a small sample size can skew the average NRMSE results high so the NRMSEs for the 1-year half-life decay are not compared. Figure 2.18 shows the NRMSE results for the 10-year half-life and the 5-year half-life decay rates.

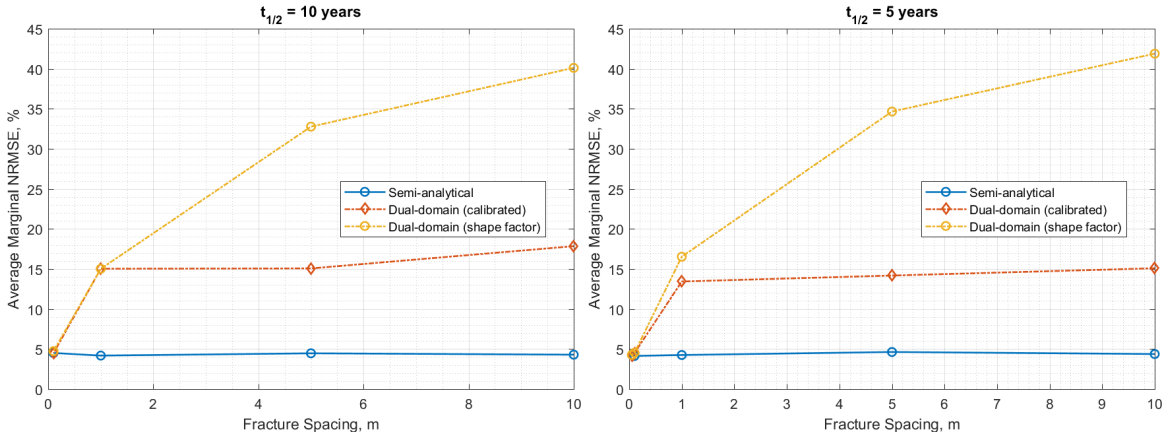

(a) (b)

Figure 2.18: Average marginal NRMSE as a function of fracture spacing for a) half-life of 10 years and b) half-life of 5 years.

The impact of decay on the dual-porosity model's accuracy was negligible when the fracture spacing is sufficiently small. Doubling the decay rate yielded similar NRMSE ranges between 0.1 m

and 10 m of fracture spacing. Calibrating the mass transfer coefficient reduced the dual-porosity model's NRMSEs but for the largest fracture spacing, even its calibrated NRMSE was three to four times than the semi-analytic model's. The accuracy of the dual-porosity model depends on the fracture spacing, similar to what we observed when varying fracture spacing without decay. Meanwhile, the accuracy of the semi-analytic model with and without decay was consistent with a NRMSE less than 5% over a range of fracture spacing.

2.4.2 Varying adsorption

Following the simulations of varying decay rates, simulations with only adsorption were evaluated. Retardation factor of 2 and 5 were tested in the same system of parallel fractures. The retardation in the matrix and in the fractures was assumed to be the same. A change in the retardation factor can be the result of variation in the fraction of the organic carbon content, which is also a function of temperature.

As the retardation factor was increased, one of the underlying physical properties of the matrix (its mass storage) necessarily increased (Figure 2.19). The change was especially apparent in the 100-year profiles (purple lines in Figure 2.19), when the peak of the fracture concentration profile decreased because more mass was stored in the matrix. The shape of the 1-year and the 49-year profile were similar to one another but the profiles in the retardation factor of 5 case had a shorter spatial extent as more solute mass changed from aqueous to solid phase, reducing the dissolved concentration in the fracture.

The semi-analytic model matched the analytical solution during the loading period better than during the unloading period (Figure 2.19). During the unloading period, it overestimated the concentration peak but was still able to match the timing of the peak and the overall shape of the analytical solution well. The overestimation reduced from over 6 mg/L at 51 years when retardation was not considered (green line in Figure 2.19a) to less than 2 mg/L (green line in Figure 2.19c).

When overlaying the dual-porosity profiles onto the semi-analytic and the analytical profiles (not shown), we observed the same trends as in the varying decay and varying fracture spacing analyses. The dual-porosity model again showed high NRMSEs at larger fracture spacing. At smaller fracture spacing, the model gave lower NRMSEs when the characteristic diffusion time was satisfied. The average marginal NRMSEs of the semi-analytic and the dual-porosity method for each fracture spacing case at both retardation rates were computed and plotted in Figure 2.20.

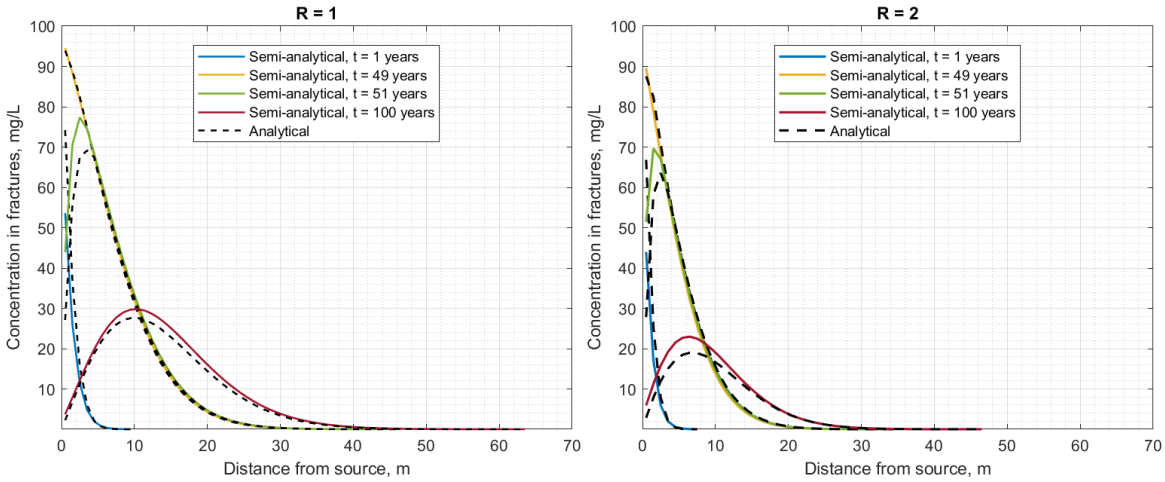

(a)

(b)

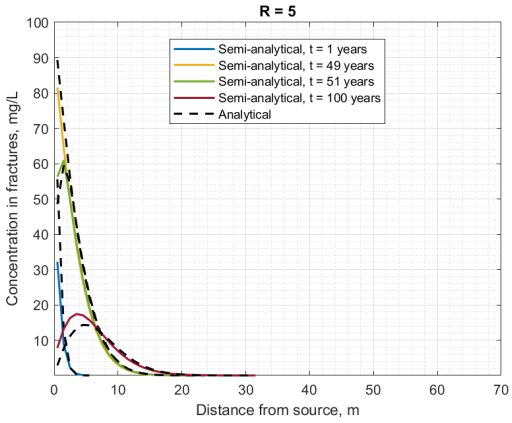

(c)

Figure 2.19: Fracture concentrations of semi-analytic model and analytical solution for fracture spacing of 1 m in the case of a) no retardation; b) retardation of 2; and c) retardation of 5.

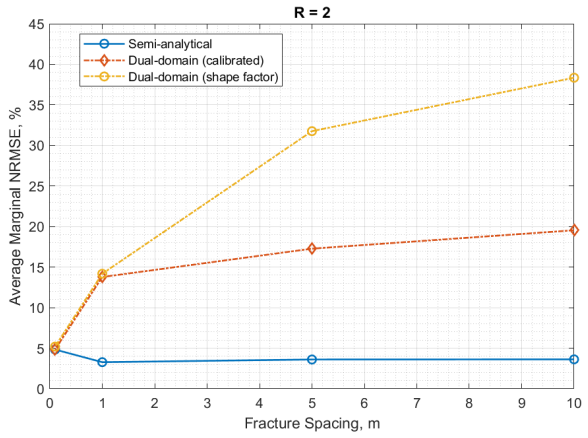

(a)

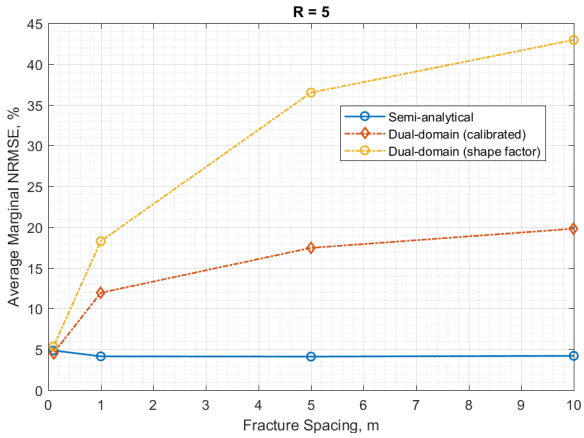

(b)

Figure 2.20: Average marginal NRMSE trends of fracture spacing cases between 0.1 m and 10 m for cases of a) R = 2 and b) R = 5.

NRMSEs of the concentration profiles predicted by the shape factor formula (yellow lines) increased as the fracture spacing and the retardation factor increased. Calibration reduced the dual-porosity model's NRMSE but even then, it was still over four to five times higher than the semi-analytic model's at the largest fracture spacing. The NRMSEs of the semi-analytic model were at or below 5%, consistent with the cases with and without decay.

2.5 Conclusion

Simulations were performed in parallel fracture systems to compare the effectiveness of the dual-porosity and the semi-analytic models in simulating dissolved concentrations in the fractures. The analytical solution by Sudicky and Frind (1982) was used as the benchmark in the comparisons.

The accuracy of the dual-porosity model with calibrations was dependent on a characteristic diffusion time, which was shown to increase with the square of the fracture spacing. At small fracture spacing when the characteristic time was small, the dual-porosity model had low NRMSEs when compared to the analytical solution because the fracture-matrix concentration gradient flattened in a short time. Meanwhile, at larger spacing, when the fracture-matrix concentration gradient is sharp over a long period of time relative to the simulation time, the model had higher NRMSEs. In a non-dimensional analysis, the dual-porosity model only gave low errors at a dimensionless time of 2.27, which equals hundreds of years in simulation time of TCE concentration in a 4-m fracture spacing case. A mathematical expression of the mass transfer coefficient based on a shape factor (van Genuchten, 1985) was used in initial dual-porosity models, prior to calibrations.

In parallel fractures, the semi-analytic model matched the analytical solution at less than 5% NRMSE without any calibration required. The results presented in this work showed that when comparing the semi-analytic model and the dual-porosity method in cases of varying fracture spacing, decay rates, and adsorption, the semi-analytic model is more accurate and robust over a range of fracture spacing. Unlike the dual-porosity method, the semi-analytic model does not depend on a characteristic diffusion time, and its modeling parameters in parallel fractures can be computed directly from the fracture geometry. The semi-analytic model is studied in the next chapter when it is applied in 2-D and 3-D discrete fracture networks.

Chapter 3

Discrete Fracture Networks

3.1 Introduction

A key to an effective groundwater remedial strategy is to understand where the mass is located in materials of contrasting permeabilities. In a heterogeneous subsurface, the solute may advance rapidly in high-permeability (high-K) material via advection while diffusing into relatively low-permeability (low-K) material. When the concentration is higher in the high-K material, a gradient toward the low-K material drives the mass to diffuse in that direction. When the gradient is reversed, the mass diffuses from the low-K material back toward the high-K material. The transport of contaminant mass between the low-K and the high-K materials by diffusion is known as matrix diffusion (Freeze & Cherry, 1979; Gillham et al., 1984; Mackay & Cherry, 1989). Observations of matrix diffusion effects in the field and in laboratory experiments are well-documented and consistent with the theoretical conceptual models (Mackay & Cherry, 1989; McKay et al., 1993; B. L. Parker et al., 1994; Ball et al., 1997; C. Liu & Ball, 2002; Chapman & Parker, 2005; Sale et al., 2013; Filippini et al., 2020).

Several types of contaminants, including radioactive solutes (Foster, 1975; Grisak & Pickens, 1980; Neretnieks, 1980; Rasmuson, 1984; Sudicky & McLaren, 1992; Therrien & Sudicky, 1996; Trinchero et al., 2020) and per- and polyfluoroalkyl substances (PFAS) (Kulkarni et al., 2022) can undergo matrix diffusion but the research about this process has been particularly well-developed for dissolved dense-non-aqueous-phase-liquids (DNAPLs) such as trichloroethylene (TCE). Fractured porous media is one of the most challenging hydrogeological setting to remediate (Pierce et al., 2018)

because the matrix volume is typically orders of magnitude larger than the fracture volume (Foster, 1975; Mackay & Cherry, 1989; Therrien & Sudicky, 1996; B. L. Parker et al., 1997, 2012; Pierce et al., 2018). The pore space in the matrix provides storage for the contaminant mass whereas the fractures act as pathways for the contaminant to spread by advection (C. K. Keller et al., 1986; Mackay & Cherry, 1989; McKay, 1991; Makedonska, 2018). When a DNAPL is spilled into a fractured media, the product phase of DNAPL may disappear in less than several years (B. L. Parker et al., 1994, 1997). However, during that time, the dissolution and diffusion of DNAPL can move a large quantity of the dissolved contaminant mass to the matrix. As the dissolved mass gradually diffuses from the matrix toward the fractures, it can cause the clean-up time to take decades (Mackay & Cherry, 1989; B. L. Parker et al., 1994; Esposito & Thomson, 1999; Chapman & Parker, 2005; B. L. Parker et al., 2012; Seyedabbasi et al., 2012; Sale et al., 2013).

3.1.1 Analytical solutions

An effective clean-up strategy will be facilitated by an accurate prediction of matrix diffusion in response to changing subsurface conditions. Either an analytical solution or a numerical model can be utilized to represent the current state of contamination and predict future transport behavior. Some of the earliest simulations of matrix diffusion (Foster, 1975; Neretnieks, 1980) were implemented using analytical solutions of 1-D diffusion into a finite or a semi-infinite matrix (Crank, 1975). Those solutions simplified the concentration in the fractures to a constant concentration, and they do not explicitly consider other transport processes such as advection and dispersion. To include those processes, researchers usually use a separate transport equation for the fractures or high-K material while maintaining one for the matrix or low-K material where only diffusion is considered. The equation for the fractures considers advective and dispersive fluxes while the transport equation for the matrix is simplified to include only the diffusive fluxes. Using that approach, Tang et al. (1981) presented an analytical solution for a single, thin fracture with matrix diffusion, solute reactions and retardation. The solution required two Laplace transformations and an inversion of the final solution to obtain fracture concentration adjusted for matrix diffusion. Roubinet et al. (2012) included two-dimensional (2-D) dispersion and 2-D matrix diffusion of conservative solutes in the same conceptual model of a single fracture. They considered the 2-D transport in the fracture as boundary value problems and used Green's functions to derive a semi-analytical solution of the concentration in the fracture.

Sudicky and Frind (1982) expanded on the Tang et al. (1981) solution to a system of parallel fractures. The solution includes advection, hydrodynamic dispersion, adsorption, and first-order decay in the fractures. For the matrix, it includes diffusion, adsorption, and first-order decay. That analytical solution uses the same approach as Tang et al. (1981), where the Laplace transform and its numerical inversion are applied to both the matrix and the fracture transport equations to solve for the concentrations. Sudicky et al. (1985) extended the analytical solution developed for a single fracture to nonreactive transport in layered sand-silt media. Starr et al. (1985) applied that sand-silt model to include reactive transport. For three-dimensional (3-D) equidistant fractures, B. L. Parker et al. (1997) derived an analytical solution by conceptualizing the matrix as parallelepipeds at a specified length, width, and height. The transient concentration in the matrix was obtained by taking the products of three 1-D solutions in a finite matrix (Crank, 1975), one for each dimension of the parallelepiped. Analytical solutions are still in use extensively today, often to calibrate and verify complex numerical models. However, for complicated applications requiring flexibility at field-scale, the numerical model approach is often chosen. We focus on a group of numerical models called discrete fracture network (DFN) models because they can represent the varying fracture attributes such as the orientation and the interconnectivity between fractures as informed by field data.

3.1.2 DFN numerical models

DFN models separate the model domain into two overlapping subdomains, one for the fracture network and one for the matrix. The interconnected elements of the fracture network are generated stochastically via probability distributions of the fracture apertures, lengths, and locations in the network. Several statistical distributions are typically built-in to the fracture generator such as Gaussian, log-normal, and exponential distributions (Endo et al., 1984; Sudicky & McLaren, 1992; Therrien & Sudicky, 1996; Pierce et al., 2018; Li et al., 2020). The distribution is chosen to best reflect the interpretation of an actual fracture network through field methods such as rock coring or borehole geophysics (B. L. Parker et al., 2012). If sufficient knowledge of the fracture geometrical and topological attributes is available, the fracture network can be visualized deterministically using dedicated 3-D geological modeling tools such as GOCAD (Blessent et al., 2009) or FracMan (Makedonska, 2018). Following the generation of fractures, the next step in the DFN approach is to discretize the modeling domain. Several meshing approaches have been utilized in the literature such as one where a structured grid of Cartesian cells at fixed spacing was used (Sudicky

& McLaren, 1992; Therrien & Sudicky, 1996). Another discretization approach is to use an adaptive mix of irregular and regular Cartesian cells depending on whether the fracture element is at the fracture-matrix interface or in the rest of the domain (Molins et al., 2019). In more recent models, researchers have preferred unstructured grids with discretization via Voronoi polygons (Hyman et al., 2015; Hadgu et al., 2017; Ngo et al., 2017) and hexahedral elements (Blessent et al., 2009). For a structured grid, a mesh of nodes at a specified spacing is overlaid over both the fracture and the matrix subdomains prior to flow and transport simulations (Therrien & Sudicky, 1996). If the grid is unstructured, special routines such as the conforming Delaunay triangulation by Hyman et al. (2015) may be required to ensure fracture intersections coincide with the edges of Voronoi volumes so that typical finite volume flow and transport solvers can be used.

There are a variety of flow and transport solutions available for DFN models after fracture elements have been generated and discretized. Some DFN models are solved using stochastic analysis of velocity and residence time distributions (Schwartz et al., 1983; Endo et al., 1984; Gillham et al., 1984) or by using particle tracking techniques i.e. the Lagrangian approach (Yates, 1990; Hyman et al., 2015; Hadgu et al., 2017; Trinchero et al., 2020). A recent particle tracking solution for DFN models was implemented by research scientists at the Los Alamos National Lab (Blessent et al., 2009; Hyman et al., 2015; Makedonska, 2018) in a comprehensive DFN modeling package called `dfnWorks`. In a particle tracking approach, advective transport is conceptualized in terms of movement of a large number of particles along pathlines, instead of solute concentration at a fixed spatial point (Zheng & Bennett, 2002). Dispersion and other transport processes such as sorption, reaction, and matrix diffusion are considered via adjustments to the particle trajectories. The primary motivation for using the particle tracking transport solution is to avoid numerical dispersion, which is inherent in the finite-difference or finite-element solutions of transport. However, if numerical dispersion can be closely managed, the case for using particle tracking techniques becomes less necessary. For the works in this manuscript, we utilize fine grid spacing to reduce numerical dispersion so we can focus on transport solutions of DFN models in Eulerian spatial grids, not Lagrangian pathlines.

In one of the earliest implementation of a DFN model, where a network of ordered equidistant fractures with constant aperture was created and simulated with horizontal and 45 degrees flow regimes, flow and transport were solved numerically using a finite-difference discretization approach (Berkowitz et al., 1988). A more efficient 2-D solution was developed using the Galerkin finite element approach with Laplace transformation and a mass transfer coefficient, which circumvents the need

to discretize the fine grid to resolve concentration gradient between the fracture and the matrix (Sudicky & McLaren, 1992). However, that DFN/dual-porosity approach requires an assumption of the matrix geometry, which is not always known. A similar type of DFN/dual-porosity hybrid model was implemented recently, which utilized the dual-porosity mass transfer coefficient as a calibrating parameter (Li et al., 2020). A more robust 3-D solution for a DFN model was developed, which uses the common-node approach where the fracture node is superimposed onto the matrix node, and the continuity of flow and mass at the fracture-matrix interface is satisfied directly without using a mass transfer coefficient (Therrien & Sudicky, 1996) . The flow and transport solutions were originally formulated using a control volume finite-element approach but the authors eventually adapted finite-difference nodal connectivities via influence coefficient matrices for efficiency (Therrien, 1992; Panday et al., 1993). That 3-D DFN model was later integrated into a larger hydrologic model called HydroGeoSphere (HGS) (Aquanty Inc., 2021). Other finite-difference discretization based transport solutions exist such as `DuMux` (Ngo et al., 2017). For flow and transport solutions of DFN models in this manuscript, we focus on applications using HGS.

HGS was utilized to create a discrete fracture network that is stylistically similar to a slice of the upland Chatsworth Formation sandstone at the Santa Susana Field Lab in Simi Hills near Los Angeles, California (Pierce et al., 2018). The site, formerly known as Rocketdyne, was operated as a rocket engines testing facility for the United States space program (Archeological Consultants, 2009) between 1949 to 2006. TCE impacts were first observed at the site in 1984, and it has since become one of the most well-known field laboratories to study groundwater contamination. (Pierce et al., 2018). Orthogonal 2-D fracture elements in the DFN were utilized to represent prominent sedimentary sequences with bedding plane fractures and near-vertical joints in the Chatsworth Formation (Pierce et al., 2018). The matrix properties for their DFN model were derived from hundreds of rock core measurements (Quinn et al., 2011; C. E. Keller et al., 2014). Steady flow under influence of the upland recharge conditions with horizontal and vertical components of the hydraulic gradient was simulated. The DFN model's bulk hydraulic conductivity was calibrated through various realizations until one matched the average hydraulic conductivity obtained from field tests.

For transport simulations at the Field Lab, a finite loading period and an unloading period following complete source removal were simulated (Pierce et al., 2018). While a 2-D discrete fracture network model was demonstrated to simulate flow and transport conditions adequately at the Field Lab, the computational demand of such a model made it less feasible to implement a similar study

in 3-D (Pierce et al., 2018). Researchers have recognized that the fine spatial discretization is a major impasse to applying numerical modeling of matrix diffusion at large scale. Three numerical models, HGS, FEFLOW and MODFLOW/MT3DMS were compared to confirm that fine spatial and temporal discretization were required to match experimental results (Chapman et al., 2012). Typically, centimeter scale discretization of the matrix is necessary to capture matrix diffusion while a field site may be at the kilometer scale (Sudicky & McLaren, 1992; Chapman & Parker, 2005; B. L. Parker et al., 2008; Chapman et al., 2012; Pierce et al., 2018; Farhat et al., 2020; Li et al., 2020; Liao et al., 2021).

3.1.3 EPM models

An alternative to the DFN model is an equivalent porous media (EPM) model. This type of model is more efficient numerically than numerical DFN models because they discretize at a larger scale, where the entire domain is considered a continuous media or a series of equivalent continua. The fine details of the modeling domain are simulated using averaged flow and transport parameters, instead of spatial discretization. Researchers have shown EPM models to be successful at replicating more finely discretized numerical models if bulk properties are accurately derived from sufficiently small representative elementary volumes and if other transport processes such as matrix diffusion is appropriately approximated (Long et al., 1982; Pankow et al., 1986; Berkowitz et al., 1988; Schwartz & Smith, 1988; McKay et al., 1993; Muskus & Falta, 2018; Pham & Falta, 2022). One of the most popular EPM models is the dual-porosity model. Early pioneers of this model applied it to simulate non-Gaussian tracer breakthrough curves in laboratory porous media cores (Barenblatt et al., 1960; Deans, 1963; Coats & Smith, 1964). The reach of the dual-porosity model was extended significantly in the United States when it became a built-in option to simulate matrix diffusion in the transport numerical code MT3DMS (Zheng & Wang, 1999; Zheng & Bennett, 2002), which interfaces directly with the numerical flow model MODFLOW (Harbaugh, 2005). The dual-porosity model divides the subsurface into two separate domains with contrasting permeabilities. The mobile domain is dominated by transport processes such as advection, dispersion, and reaction while only diffusion and reaction are active in the immobile domain. A volume fraction can be used to specify how much of the model domain is mobile and to compute the mobile and the immobile porosities (Pham & Falta, 2022). Each domain has a transport equation, and they are linked by a first order mass transfer coefficient (Barenblatt et al., 1960; Deans, 1963; Coats & Smith, 1964; Zheng & Wang,

1999; Zheng & Bennett, 2002).

The geometry of the matrix must be assumed to derive an analytical expression of the mass transfer coefficient (Huyakorn et al., 1983; van Genuchten, 1985; Haggerty & Gorelick, 1995; de Vries et al., 2017; Perina, 2022). For a system of parallel fractures, a shape factor formula to compute the mass transfer coefficient is available using the fracture spacing and the matrix properties (van Genuchten, 1985). That mass transfer coefficient worked in a dual-porosity model of a parallel fracture system of small spacing (Neville, 2006) but it did not give accurate results for systems of large fracture spacing (Pham & Falta, 2022). The dual-porosity model calculates the mass flow between the matrix and fractures using a linear driving force model, which relies on the concentration difference between the fractures and the matrix. If diffusion distances are short or times are large, this approach can work well. However, for larger diffusion distances or smaller times, the linear driving force model is unable to accurately resolve the concentration gradient near the fracture-matrix interface (Pham & Falta, 2022). Several researchers have observed that the dual-porosity model may require a time-dependent mass transfer coefficient to match observed transport behavior (Adams & Gelhar, 1992; Boggs & Adams, 1992; Boggs et al., 1992; Haggerty & Gorelick, 1995; Feehley et al., 2000; Guan et al., 2008). The time-dependency of the dual-porosity model was also confirmed recently in laboratory tank experiments (Swami et al., 2018) and in a 3-D analytical solution to the dual-porosity model (Perina, 2022).

A newer EPM model called the semi-analytic trial function model was developed (Falta & Wang, 2017; Muskus & Falta, 2018) with a user-interface called REMChlor-MD (Farhat et al., 2018). This model retains the efficiency of the dual-porosity model without the inherent time-dependency. It uses a trial function to approximate the concentration in the low-permeability material using the concentration in the high-permeability material (Vinsome & Westerveld, 1980; Bear et al., 1994). The trial function dynamically adjusts for the change in concentration gradient between the high-K and low-K materials in each discretized element and at each timestep. The matrix diffusion mass flux can be computed from the gradient of the trial function and added directly to the usual advection-dispersion equation as a source/sink term. The equation is then solvable via a typical finite-difference or finite volume numerical method. The semi-analytic model performed well when compared to analytical solutions of a two-layer aquifer/aquitard system and a system of parallel fractures (Falta & Wang, 2017; Muskus & Falta, 2018; Pham & Falta, 2022). It was able to replicate laboratory experiments of a tracer in a thin clay layer and of a sand box with embedded

clay layers (Muskus & Falta, 2018). The model was also able to accurately approximate results from a fine-grid 3-D numerical model of heterogeneous granular media (Muskus & Falta, 2018).

3.1.4 Novelty and uniqueness

The DFN and EPM approaches use different methodologies to simulate matrix diffusion. The DFN approach maximizes the availability of field data to create realistic fracture networks, and then, it uses a fine numerical mesh to solve the matrix diffusion flux. However, because matrix diffusion occurs over a length scale that is many orders of magnitude smaller than the size of the model, DFN models need to be finely discretized, requiring substantial computing resources. The EPM approach with coarser discretization is numerically more efficient but its usability requires an approximation of sub-gridblock transport processes such as matrix diffusion.

In this manuscript, the objective is to establish the utility of the semi-analytic model in a 2-D DFN model and in a series of synthetic 3-D discrete fracture networks at varying fracture spacing. We are unaware of another application of the semi-analytic model to simulate matrix diffusive transport in discrete fracture networks, especially those with a large matrix volume and that are finely-discretized at field scale in 3-D. Our simulations include a finite source loading condition, mimicking the sequence of active source, complete source removal, and a clean water flush. This source condition induces a change in the concentration gradient from a direction toward the matrix to a direction from the matrix. For every comparison between the DFN models and the semi-analytic model, we also include dual-porosity simulations to highlight the limitation of its assumption on the mass transfer process.

3.2 2-D Discrete Fracture Network

A two-dimensional (2-D) fine-grid discrete fracture network (DFN) model was generated to simulate steady flow and transient transport with matrix diffusion. The model was parameterized similarly to the 2-D discrete fracture network-matrix (DFN-M) model by Pierce et al. (2018), which was created based on site-informed data at the Santa Susana Field Lab (Field Lab). All DFNs in this research were generated with both fracture and matrix domains so the two terms DFN and DFN-M are used interchangeably.

This section describes the methodology behind the comparison of three different models.

The first type is a 2-D DFN model that is similar in terms of fracture properties, flow, and transport conditions to the 2-D DFN-M model at the Field Lab (Pierce et al., 2018). This DFN model was built using a fine-grid to ensure that the matrix diffusion gradient was fully captured, and the numerical dispersion was minimal. Because of the discretization, the DFN model took six hours to complete flow and transport simulations on a workstation with an Intel Core i7 2.80Ghz processor. The second and third type are EPM models built on much coarser grids using the semi-analytic and dual-porosity models. The coarse-grid models ran in a few minutes because they mathematically approximated matrix diffusion at the subgridblock scale, circumventing the need for fine discretization. Mass discharge and concentration contours of the coarse-grid EPM models were compared to those of the DFN to assess how the coarse-grid models simulate key features of the more computationally demanding DFN model.

3.2.1 Methodology

3.2.1.1 HydroGeoSphere DFN model

We used HydroGeoSphere (HGS) (Therrien & Sudicky, 1996; Aquanty Inc., 2021) to create all of our DFN models. Runtime for each model was tracked to measure the efficiency of each DFN model and to compare with the EPM semi-analytic and the dual-porosity models. The tracked DFN runtime does not include pre- and post-processing times. The built-in 3-D random fracture generator for block grids in HGS was activated to create a 2-D DFN, where the model's width and transverse spacing were set to unity (Walton, 2021). The random fracture generator accepts three main inputs to produce a DFN realization: the fracture frequency, the fracture location distribution, and the fracture length. Three sets of those inputs are required, one for each dimension in 3-D. To make the 3-D random fracture generator produce 2-D DFNs, we set the transverse fracture frequency to zero, the transverse fracture location distribution to 0.5, and the transverse fracture length distribution to unity (Walton, 2021). The fracture lengths were uniformly distributed at lengths between 20 m to 100 m in the x direction and between 5 m to 15 m in the z direction, identical to the 2-D DFN model at the Field Lab (Chapman, 2021). We iterated the rest of the inputs in the random fracture generator until a realization produced a similar number of total fractures as in the Field Lab DFN-M model. The chosen realization has a total of 2,250 orthogonal fractures in xz and yz planes, nearly identical to the Field Lab DFN-M model (Chapman, 2021). The 2-D gridblock spacing was kept

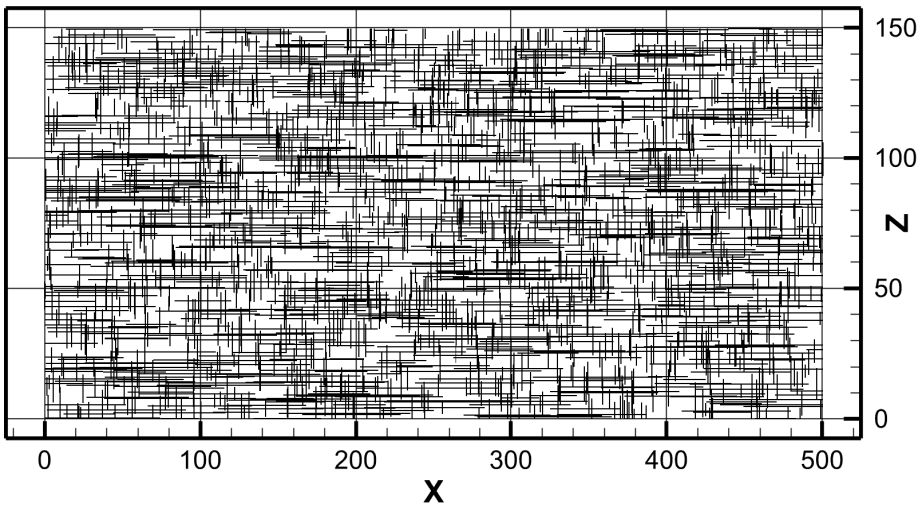

Figure 3.1: Generated 2-D discrete fracture network with fracture properties similar to Pierce et al. (2018)

at 0.1 m horizontally and vertically to ensure matrix diffusion fluxes can be captured. The model domain was set to 500 m in length and 150 m in depth. The 2-D DFN model contains a total of 7.5 million gridblocks (Figure 3.1).

After generating a 2-D DFN with a satisfactory number of total fractures, we simulated flow through the DFN by applying head boundary conditions at the inlet and outlet of the model to produce a hydraulic gradient of 0.01. While Pierce et al. (2018) implemented both horizontal and vertical flows, the focus of our study is the matrix diffusive transport so we simplified the numerical flow model by simulating only a horizontal flow field. Although head boundary conditions were set to generate only horizontal flow across the model domain, some vertical flows did occur locally in the model through vertical fracture conduits. The fracture aperture distributions were set to be uniform in all directions and were iterated until an average linear groundwater velocity in the fractures similar to the Field Lab's velocity was found. The linear velocity can be calculated by: $\bar{v}_f = K_b i_g/(V_f \phi_f)$, where K_b is the bulk hydraulic conductivity through the DFN, i_g is the hydraulic gradient, V_f is the volume fraction of fractures, and ϕ_f is the material porosity of the fractures. The denominator $V_f \phi_f$ is the bulk fracture porosity in Pierce et al. (2018)'s study. When ϕ_f is unity, the bulk fracture porosity is identical to the volume fraction of fractures in the DFN.

The volume fraction V_f, which was introduced by Muskus and Falta (2018) to simulate embedded heterogeneities in the semi-analytic model, was used to specify the volume of the discrete

fractures in the total volume. Generally, the volume fraction is defined as the ratio between a high-permeability material to the total volume (Muskus & Falta, 2018). A DFN consisting of 2-D fracture elements in three dimensions is shown in a conceptual model in Figure 3.2.

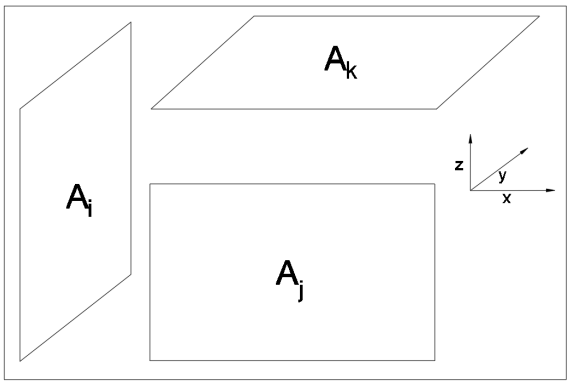

Figure 3.2: A conceptual model of a 3-D DFN, consisting of orthogonal 2-D fracture elements in 3-D.

The volume fraction of a DFN can be computed directly using the total fracture area, A_f, which is the sum of the 2-D fracture element areas in 3-D:

$$A_f = \sum^{i} y_i z_i + \sum^{j} x_j z_j + \sum^{k} x_k y_k \tag{3.1}$$

$$V_f = \frac{A_f b}{V} \tag{3.2}$$

In Equation 3.1, x_j, x_k, y_i, y_k, z_i, and z_j are the fracture lengths whereas i, j, and k are the number of fractures in 3-D. In the case of a 2-D DFN model not containing A_j elements, the sum $\sum^{j} x_j z_j$ in Equation 3.1 equals zero. Using fracture length outputs from the 2-D DFN model in HGS, A_f was computed to be nearly 57,000 m^2. In Equation 3.2, b is the fracture aperture and V is the total volume of the model domain. Through iterations of several 2-D DFNs, we found that a uniform fracture aperture of approximately 100 μm produced similar volume fraction and average linear groundwater velocity to the Field Lab's. Knowing the aperture and the total fracture area, the volume fraction for the chosen realization of our 2-D DFN was computed using Equation 3.2 to be $7.5 * 10^{-5}$, which is in the same order of magnitude as the bulk fracture porosity reported by Pierce et al. (2018). From the volume fraction, an average fracture spacing of the DFN can be

computed:

$$a = \frac{(1 - V_f)V}{A_f} \tag{3.3}$$

The numerator of Equation 3.3 is the total volume of the matrix, which equals the product of the matrix surface area and the average spacing between the fractures. Because the fractures share the same surface area with the matrix, all variables of Equation 3.3 are known, and the average fracture spacing was computed to be 1.32 m.

After a DFN with satisfactory fracture properties was generated, a steady-state flow model was simulated in HGS using a control volume finite-difference method (Therrien & Sudicky, 1996) to solve the flow equations across the modeling domain. We computed the average Darcy velocity V_d by averaging the inlet and outlet flow rates from HGS's water balance output file and dividing it by the model's depth and width (unity for 2-D DFNs), which gave an average Darcy volumetric flux of 0.0926 m/yr across the model. For comparison, we computed the average Darcy flux of the Field Lab DFN-M model to be 0.0946 m/yr, using the site's K_b of 9.46 m/yr and the hydraulic gradient i_g of 0.01 (Pierce et al., 2018). Dividing the average Darcy flux by the volume fraction gives the bulk linear groundwater velocity $\bar{v}_f$ of the fracture system, which was 1,235 m/yr. Table 3.1 summarizes the flow and transport parameters of the 2-D DFN.

To simulate transient mass transport through the 2-D DFN, we applied a TCE source concentration of 0.1 g/L over an elevation range between 90 m and 150 m at the inlet of the model. The source was held constant for 20 years prior to a complete removal, after which clean water was flushed through the DFN for another 230 years. An initial timestep of 0.1 day was used but the model was allowed to adjust the timestep adaptively, subject to a maximum allowable change in relative concentration of 0.01 (Therrien & Sudicky, 1996). We set the matrix porosity ϕ_l in the DFN to be 0.13 based on historical data at the Field Lab. The matrix porosity is four orders of magnitude larger than the bulk fracture porosity, indicating the large porous space available in the matrix for the storage of the contaminant mass. A retardation factor of 2 was applied for both the fractures and the matrix. Advection was considered in the model with upstream weighting but degradation was not. Dispersivity values in both the matrix and the fractures were set to zero.

The model solved the transport equations using the same control volume finite-difference method as in the flow simulation (Therrien & Sudicky, 1996). A common node approach was utilized

Table 3.1: Flow and transport properties of the 2-D DFN

Parameter	Fracture	Matrix
a, m		1.32
Δx, m		0.1
Δz, m		0.1
x, m		500
z, m		150
Total gridblocks		7.5e6
b, m	9.90e-5	-
V_f	7.500e-5	0.9999
i_g, m/m		0.010
V_d, m/yr	0.0926	-
$\bar{v}_f$, m/yr	1,235	-
Porosity	1	0.13
Tortuosity	1	0.1
Retardation		2
D, m^2/yr		0.0316
C_0, g/L		0.1
Source area, m^2		60
Loading, yrs		20
Unloading, yrs		230
dt, day		0.1^a
Runtime, hrs		6^b

[a] Adaptive to a concentration control of 0.01
[b] A flow simulation takes 10 to 20 minutes of the total runtime
[b] Pre- and post-processing times not included
[b] Simulated using an Intel Core i7 2.80GHz processor

internally, where the fracture domain was superimposed onto the matrix, ensuring the continuity of concentration can be determined nodally between domains without specifying a solute mass exchange term (Therrien & Sudicky, 1996). Due to the fine discretization in both vertical and longitudinal directions to capture the matrix diffusive flux between the domains, the total runtime for both the flow and transport simulations in the 2-D DFN was 6 hours using a workstation with an Intel Core i7 2.80GHz processor.

3.2.1.2 Semi-analytic model

An equivalent porous media (EPM) approach was utilized to set up the semi-analytic model on a coarse 2-D grid to approximate matrix diffusive transport in the DFN. The longitudinal spacing Δx was set to 1 m to minimize numerical dispersion. The vertical spacing Δz of 10 m was 100 times larger than the vertical spacing in the DFN. The total number of gridblocks was 7,500, three orders of magnitude smaller than the total gridblocks in the 2-D DFN model. The semi-analytic model

assumes a homogeneous constant velocity field with a Darcy velocity as a direct input.

The maximum DFN plume mass was extracted from HGS's mass balance output file and averaged over the loading period to calculate the maximum mass discharge entering the model, $\dot{m}_{max}$. That mass discharge was scaled to a coarse-grid area A_s to compute a source concentration C_0 for the coarse-grid models: $C_0 = \dot{m}_{max}/(V_d A_s)$. The source area for the coarse-grid models was placed at the inlet, and it spanned over 6 vertical gridblocks between 95 m and 145 m in block-centered elevations. The scaled source mass discharge produced a source concentration C_0 of 0.09 g/L. We compared the transient plume mass of the DFN and the coarse-grid models to ensure the designed source mass discharge produced the same overall mass in the coarse-grid models as in the DFN plume. The semi-analytic model solved for the advection term of the transport equation using the standard finite-difference method with upstream weighting at a fixed timestep of 0.02 years. This method has an inherent dispersivity of $\Delta x/2$, which is 0.5 m for this semi-analytic model. The transverse and vertical dispersivities were kept at zero. Other transport parameters in the semi-analytic model were identical to the DFN model, including the porosities, the tortuosities, and the retardation factors of both domains.

The semi-analytic model approximates matrix diffusion using three parameters: the volume fraction V_f, the matrix diffusion area A_{md}, and the diffusion length L_{md}. Those parameters are related in a similar matrix volume balance as in Equation 3.3 but instead of using the model's volume, a gridblock volume V_{gb} is used:

$$(1 - V_f)V_{gb} = A_{md}L_{md} \tag{3.4}$$

With a known gridblock volume of 10 m^3, only two of the matrix diffusion parameters were needed while the third was directly solved. The diffusion length of 0.66 m is half the known average fracture spacing. The volume fraction was known so A_{md} was directly calculated to be 15.2 m^2. Because the majority of the flow and transport occurs in the horizontal fractures, the semi-analytic parameters were adjusted to exclude the vertical 2-D fracture elements perpendicular to the flow. Without A_i, the total fracture area decreased to 42,000 m^2, and volume fraction was lowered to $5.500 * 10^{-5}$. The L_{md} increased to 0.89 m and the A_{md} increased to 11.2 m^2. This adjustment to L_{md} and A_{md} has been found to improve the accuracy of the semi-analytic model in simulating both 2-D and 3-D DFN models. The runtime for the semi-analytic model was approximately 3 minutes, using the

same workstation as for the DFN model. Table 3.2 summarizes the parameters of the semi-analytic models.

Table 3.2: Parameters for 2-D semi-analytic model

Parameter	Semi-analytic
Δx, m	1
Δz, m	10
Total gridblocks	7,500
Source area, m^2	$6\Delta z$
C_0, g/L	0.09
V_f	5.5e-5
A_{md}, m^2	11.2
L_{md}, m^2	0.89
dt, yrs	0.02
Runtime, $mins$	3

3.2.1.3 Dual-porosity model

On the same coarse grid as the semi-analytic model, a dual-porosity transport model was created using MT3DMS (Zheng & Wang, 1999; Aquaveo, 2019). The MT3DMS model did not take the Darcy velocity as a direct input so a steady-state MODFLOW model was run first. Similar to the DFN model, head boundary conditions were assigned to produce a 0.01 hydraulic gradient from the inlet to outlet of the grid. When the MODFLOW model produced the same average Darcy velocity as the DFN model, the transport model MT3DMS was initiated using the flow field from MODFLOW.

The transport parameters for MT3DMS were identical to the parameters from the semi-analytic model, except for the mass transfer coefficient β. The dual-porosity model uses β to simulate matrix diffusion between the fractures and the matrix. This parameter was initially estimated using a shape factor formula developed for 1-D parallel fractures (van Genuchten, 1985; Neville, 2006; Pham & Falta, 2022):

$$\beta = \frac{3\tau_l D \phi_l (1 - V_f)}{L_{md}^2} \tag{3.5}$$

Using the adjusted diffusion length of the semi-analytic model, the initial β was computed to be 0.0015 $1/yr$. Calibration of β was implemented via trial and error to seek a mass transfer coefficient that produced the lowest error in comparison to the DFN model. In Section 3.2.1.4, we explain how

this error is computed.

Two dual-porosity models were created for each mass transfer coefficient case, one for the loading period and one for the unloading period using the same mass transfer coefficient. The concentrations at the end of the loading model were used as initial conditions for the unloading model. The dual-porosity model ran in a total of 6 minutes using the same workstation as the one used for the DFN and the semi-analytic models.

3.2.1.4 Comparison metrics

Following the completion of each HGS, semi-analytic, and dual-porosity simulation, we obtained dissolved fracture concentrations as outputs. The HGS output files including the geometry of 2-D fracture elements and the concentrations were imported into a plotting and computational post-processing software called Tecplot 360 (Tecplot Inc., 2020) for visualization of the concentration contours. Time series of the DFN mass discharges were computed in Tecplot 360 by integrating the the concentrations, the Darcy velocities, and the apertures over the fracture elements in a yz cross-section. For a 3-D DFN, we have:

$$\dot{m}_i^t = b \int C_k^t |\mathbf{q}| dz + b \int C_j^t |\mathbf{q}| dy \tag{3.6}$$

where $\dot{m}_i^t$ is the transient mass discharge at a cross-section x_i distance along the length of the plume, and b is the uniform fracture aperture. The transient fracture concentrations in vertical and transverse locations are C_k^t and C_j^t. The magnitude of the Darcy volumetric flux at fracture locations is $|\mathbf{q}|$, which can be computed using: $|\mathbf{q}| = \sqrt{u^2 + v^2 + w^2}$, where u, v, and w are horizontal, transverse, and vertical components of the Darcy flux. Because the flow direction in our DFN models is dominant horizontally, the transverse and vertical components of the Darcy flux vector are small relative to the horizontal component. Therefore, $|\mathbf{q}|$ was approximated as: $|\mathbf{q}| = u$. The integral domains are dy, and dz, which are the discretized 2-D fracture lengths. The integrated fracture lengths and the aperture make up the cross-sectional area of the mass discharge. For a 2-D DFN with a unity width, Equation 3.6 simplifies to contain only the first term on the right hand side.

The mass discharge from the coarse-grid EPM models were computed similarly but instead of using the fracture aperture in the cross-sectional area, the coarse-grid models integrate over the EPM cross-sectional area instead. At each yz cross-section, the mass discharge for EPM models

with an unidirectional flow is:

$$\dot{m}_i^t = V_d \int \int C_{j,k}^t dy dz \tag{3.7}$$

where the integral domains dz and dy are the gridblock's width and depth.

The root-mean-squared-errors (RMSEs) were computed between the transient mass discharges of the EPM models and the DFN model for each cross-section x_i:

$$\text{RMSE}_i = \sqrt{\sum^t \frac{(A_t - O_t)^2}{n_t}} \tag{3.8}$$

where RMSE_i is the RMSE at a cross-section x_i, A_t is the actual transient mass discharge in the DFN and, O_t is the observed transient mass discharge of either the semi-analytic or the dual-porosity model. The total number of transient mass discharges n_t was 250, one for each year of the loading and unloading periods. The RMSE was normalized to the maximum plume mass discharge $\dot{m}_{max}$, and a marginal normalized RMSE (NRMSE) was computed to have a single metric of comparison across n_i cross-sections for each model:

$$\text{NRMSE}_i = \frac{\text{RMSE}_i}{\dot{m}_{max}} \tag{3.9}$$

$$\text{Marginal NRMSE} = \sum^i \frac{\text{NRMSE}_i}{n_i} \tag{3.10}$$

Marginal NRMSEs for the semi-analytic models were computed over a total of $n_i = 9$ cross-sections along the length of the plume. For the dual-porosity model, a marginal NRMSE was computed for each calibration of the mass transfer coefficient.

3.2.2 2-D DFN Results

3.2.2.1 Mass discharge comparisons

The semi-analytic and the dual-porosity models are similar in how they simulate advective, dispersive, and reactive transport. Where they differed is the approximation of matrix diffusion. Prior to comparing the matrix diffusion approaches, we verified that their non-matrix diffusive mass discharges were the same. In the verification, the two models showed a constant mass discharge during the loading period and a rapid drop to zero in the unloading period. Without matrix

diffusion, the contaminant mass was removed from the model almost as soon as the source was removed.

Matrix diffusion was simulated in the dual-porosity model by including a non-zero mass transfer coefficient β. An initial β value was computed to be 0.0015 $1/yr$ using Equation 3.5 and a L_{md} of 0.89 m. The mass transfer coefficient had been shown to be a time-dependent parameter in a system of 1-D parallel fractures (Pham & Falta, 2022). The time-dependency causes the dual-porosity model to produce mass discharges with low NRMSEs only at large simulation times relative to a characteristic time. The characteristic time can be approximated by the time when the DFN model's mass discharge curve flattens. At 4.5 m (Figure 3.3a), the DFN mode's mass discharge curve flattened after 10 years (loading period), and after 40 years (unloading period). At locations further from the inlet of the model, the characteristic time increases to about 90 years at 24.5 m (Figure 3.3b) and to 100 years at 44.5 m. When the characteristic time is larger than the simulation time, the dual-porosity mass discharge curve did not follow the DFN mode's mass discharge closely. A best fit β value was found via a trial and error calibration. The best fit β reproduced the DFN model mass discharge with an error of 1.9% at 4.5 m but that error increased to 9.3% at 24.5 m (green dashed line in Figure 3.3b) and 7.6% at 44.5 m (Figure 3.3c). The error was still two times the error at 4.5 m at the end of the plume (3.3d). The NRMSEs of the dual-porosity model were computed for five additional cross-sections, and the marginal NRMSE was 4%.

Matrix diffusion was simulated in the semi-analytic model by setting the A_{md} to the computed value. Concentration outputs were integrated to compute transient mass discharge over various cross sections along the length of the plume. Four of those cross-sections are shown in Figure 3.3 at gradual distances from the source until the DFN normalized mass discharge was below 10% of the source concentration. As the cross-section was further from the source, the peak DFN mass discharge decreased from close to 90% of the maximum mass discharge (circle in Figure 3.3a) to less than 10% at 184.5 m (Figure 3.3d). The semi-analytic model reproduced the DFN mass discharge curve at 1% error on average and matched the peak discharge more closely at distances far from the source. It took the semi-analytic model a few minutes of computing time to replicate the output of a finely discretized DFN model that required hours of computing time to complete.

The semi-analytic profile retained the efficiency of the dual-porosity model but improved on its robustness by accurately and consistently simulating the DFN mass discharge at different locations of the plume at all times. A single set of the semi-analytic matrix diffusion parameters

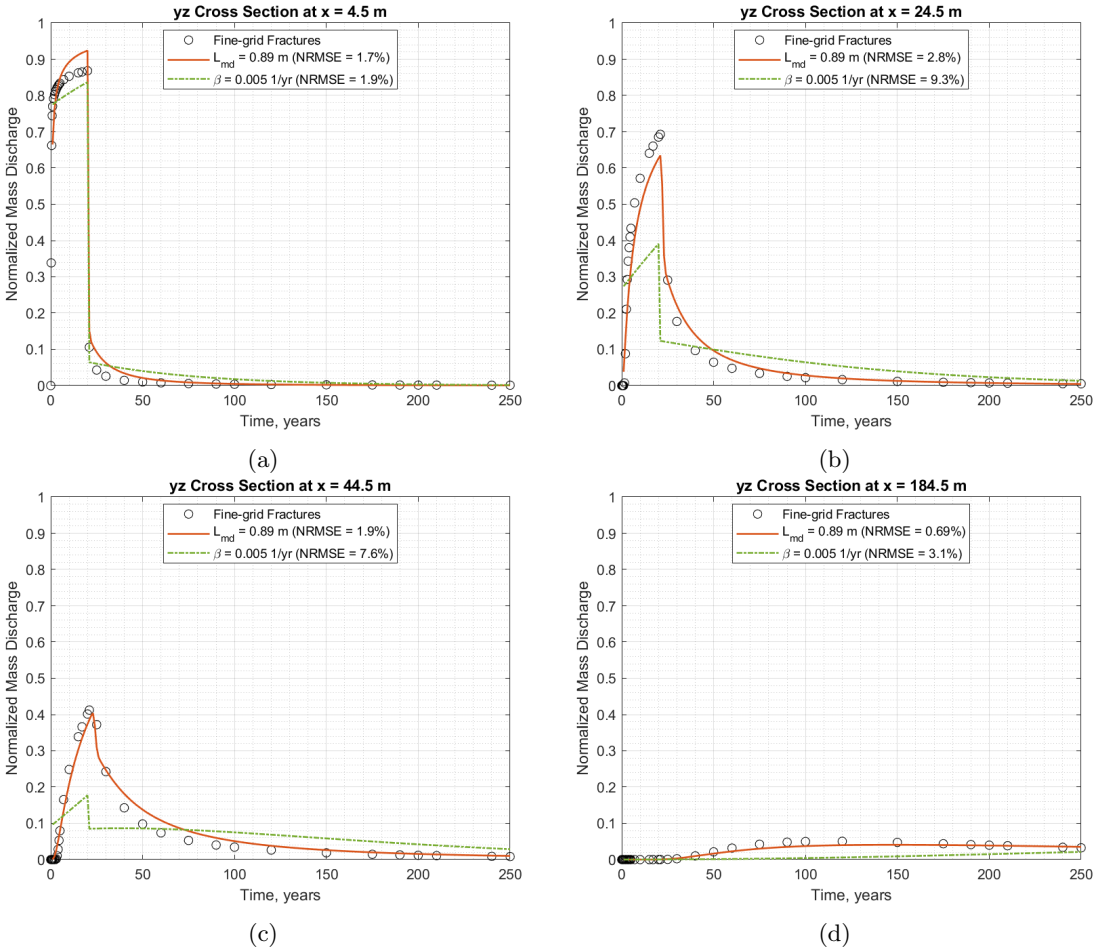

Figure 3.3: Semi-analytic (red solid lines), calibrated dual-porosity (dashed green lines), and DFN model (circles) mass discharges at: a) x = 4.5 m, b) x = 24.5 m, c) x = 44.5 m, and d) x = 184.5 m. Semi-analytic marginal NRMSE was 1% over a total of nine cross-sections (only four shown). Dual-porosity marginal NRMSE was 4% over the same total number of cross-sections.

was sufficient to recreate the DFN mass discharges within a 1% error on average.

3.2.2.2 Concentration Contours

At 10 years, the front of the DFN plume (top panel in Figure 3.4a) was at approximately 150 m with the edge of the highest concentration contours at about 60 m from the model's inlet. At 50 years (top panel in Figure 3.4b), when the source had been removed for 30 years, the plume's center of mass was followed by a clean water front at concentrations several orders of magnitude smaller. At 80 years after source removal (top panel in Figure 3.4c), the highest fracture concentration contours were largely gone, except for a few isolated spots at the inlet where the source was placed in some hydraulically isolated fractures.

Over both the loading and unloading periods period, the semi-analytic model (middle panels in Figure 3.4) was able to replicate the movement of the plume in the DFN, coming within a few meters of the DFN plume extent over several orders of magnitude of the concentration.

At 10 years, the $1 * 10^{-4}$ to $1 * 10^{-6}$ contours (dark green to blue in Figure 3.4a) of the calibrated dual-porosity model were further than the extent of the same contours of the DFN model. The higher concentration contours (red to light green in Figure 3.4a) matched with the DFN contours. At 50 years, the dual-porosity model appeared to underestimate the center of mass because the 0.01 to 0.1 concentration contour was not simulated (bottom panel in Figure 3.4b). The dual-porosity plume advanced in the unloading period at a slower rate than the semi-analytic and the DFN model over time.

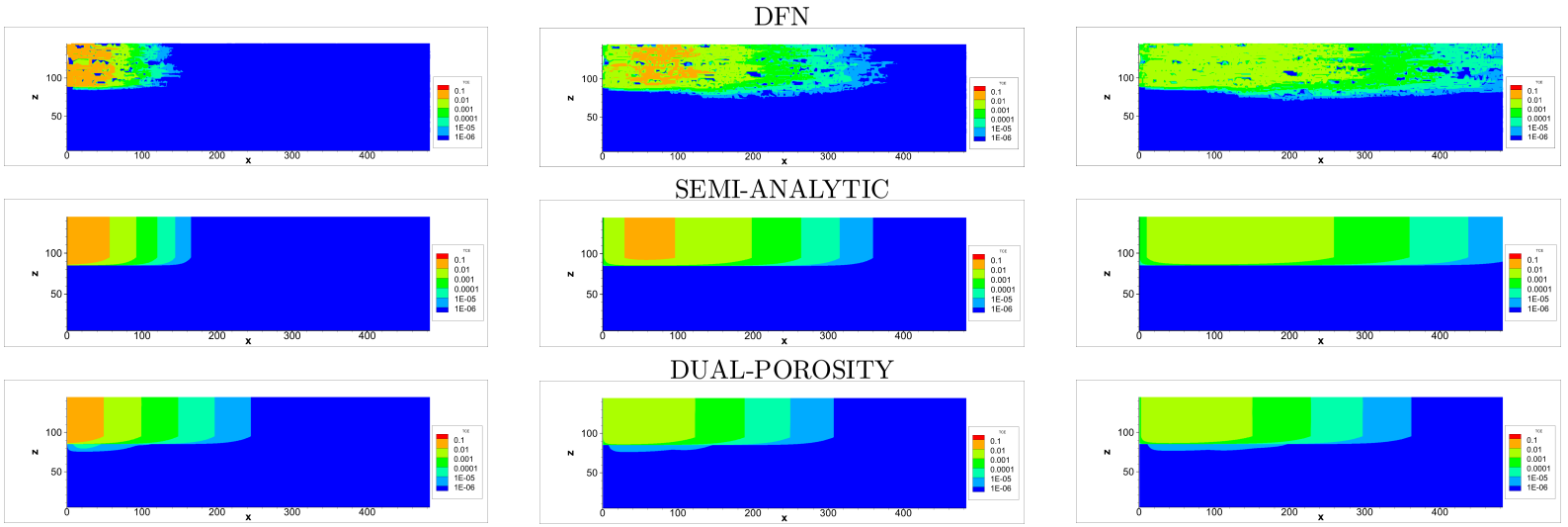

(a) t = 10 years (b) t = 50 years (c) t = 100 years

Figure 3.4: Comparison of semi-analytic and dual-porosity fracture concentrations to DFN fracture concentrations after: a) 10 years, b) t = 50 years, and c) t = 100 years.

3.3 3-D Discrete Fracture Networks

In this section, we built multiple synthetic 3-D DFN models over a range of fracture spacing to expand on the study of the semi-analytic and the dual-porosity models at simulating matrix diffusion in fractured media.

3.3.1 Methodology

3.3.1.1 HGS 3-D DFN models

Three DFNs in 3-D were generated at 50 m wide with average fracture spacing of 0.6 m, 1.2 m, and 4.3 m. The 0.6-m and 1.2-m fracture spacing models were 20 m deep whereas for the 4.3-m fracture spacing model, we maintained a large fracture spacing by doubling the depth of the model to 40 m. Because of the added third dimension, we decreased the model extent to 210 m and tripled the gridblock spacing to stay within reasonable computational limits of HGS. We found that a gridblock spacing of 0.3 m is the finest discretization for a 3-D DFN of this size and fracture configuration to run in HGS. The total number of gridblocks at 0.3-m gridblock spacing for the 0.6-m and the 1.2-m fracture spacing models was 8 million gridblocks. For the largest fracture spacing case of 4.3 m at the same gridblock spacing, the total number of gridblocks was up to 16 million.

The number of fractures in each 3-D DFN model decreased with the fracture spacing. The smallest fracture spacing model contained over 6,600 fractures whereas the 1.2-m and 4.3-m spacing models had about 3,800 and 1,500 fractures respectively. Fractures were distributed over the entire length, width, and depth of the models. Fracture lengths were uniformly distributed by the random fracture generator with lengths between 1 m to 95 m in the x direction, between 1 m to 23 m in the y direction, and between 1 m to 5 m in the z direction. The fracture aperture was uniformly set to 70 μm. The three-dimensional fracture frequencies were iterated so that the total number of fractures stayed within the computational limits of HGS to discretize the model's domain.

The volume fraction for the 0.6-m fracture spacing model was $1*10^{-4}$, an order of magnitude larger than the volume fraction of the 2-DFN model. The volume fraction decreased with the fracture spacing as fractures were further apart and less fractures were placed in the network. Table 3.3 shows the computed volume fraction for each of the three DFN models. Figure 3.5 shows the generated DFN realizations for each fracture spacing case.

We simulated flow through the 3-D DFNs using the same approach as in the 2-D DFN

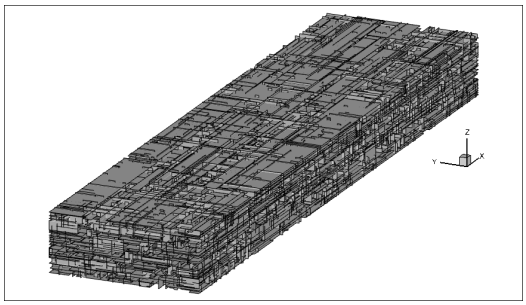

(a) a = 0.6 m

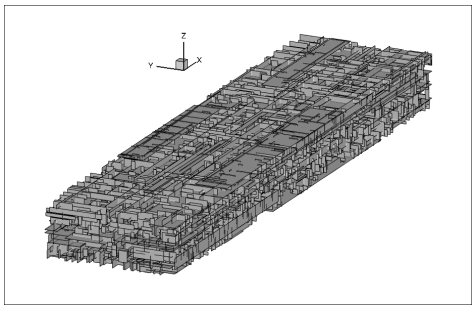

(b) a = 1.2 m

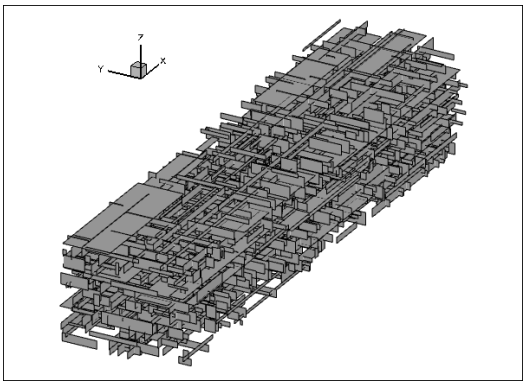

(c) a = 4.3 m

Figure 3.5: 3-D discrete fracture networks of increasing fracture spacing generated using the 3-D random fracture generator in HGS

study. Head boundary conditions were placed at the inlet and the outlet of each 3-D DFN model to produce a 0.01 hydraulic gradient. The inlet and outlet flow rates were extracted from the water balance output file of the HGS model to compute the average Darcy velocity of each 3-D DFN model. The volume fractions, the bulk hydraulic conductivities and the linear groundwater velocities were computed using the same procedures as in the 2-D DFN model. As the number of fractures decreased with the fracture spacing, the velocities also decreased because less conduits were available for groundwater flow through the fracture networks. The Darcy velocity of the largest fracture spacing DFN model was an order of magnitude smaller than those of the smaller fracture spacing model. Table 3.3 summarizes the flow parameters of the three 3-D DFN models.

For the transport simulations, we applied the same source concentration from the 2-D DFN model over a 50 m^2 cross-sectional area, which was centered laterally and vertically at the inlet of each 3-D DFN model. We held that source concentration constant for 20 years, then removed it and simulated a clean water flush through each DFN model for 230 years. Retardation was not considered so the distribution coefficient K_d was set to zero and the fracture retardation factor was

Table 3.3: Flow and transport properties of 3-D DFN models.

a, m	0.613	1.18	4.30
b, μm		70	
Δx, m		0.3	
Δy, m		0.3	
Δz, m		0.3	
i_g, m/m		0.010	
Source area, m^2		50	
K_d, m^3/kg		0	
R		1	
Fractures	6,672	3,855	1,542
V_f	1.142e-4	5.916e-5	1.629e-5
V_d, m/yr	0.0929	0.0402	0.00678
$\bar{v}_f$, m/yr	813	679	417
Runtime[a], hrs	6	7	11
x, m		210	
y, m		50	
z, m	20		40
Total gridblocks	8e6		16e6

[a] Included 10 to 20 minutes of flow simulation
[a] Pre- & post-processing times not included

set to unity. Table 3.3 shows the transport parameters for the 3-D DFN models. Only parameters different from the 2-D DFN in Table 3.1 were included.

Using the same numerical solution in HGS, it took six hours for the model with the smallest fracture spacing to complete and 11 hours for the model with the largest fracture spacing. The runtime for the lower fracture spacing cases was similar to 2-D DFN model because the addition of the third dimension was compensated by the decrease in model's length and the increase in gridblock spacing.

3.3.1.2 Semi-analytic and dual-porosity models

Semi-analytic and dual-porosity models were created with the same overall dimensions for each 3-D DFN model. The gridblock spacing was an order of magnitude larger than the DFN spacing at Δx of 1 m, Δy of 5 m, and Δz of 2.5 m. All three grids contained 210 gridblocks in the x direction and because of symmetry, only 5 gridblocks in the y direction were needed. Vertically the coarse grids for the two smaller fracture spacing models had 8 gridblocks and the 4.3 m spacing model had 12 blocks. The largest number of total gridblocks was 12,600 blocks, two orders of magnitude smaller than the largest 3-D DFN gridblock total.

For flow simulations, the semi-analytic models take the Darcy volumetric fluxes as direct

inputs. Steady-state MODFLOW simulations with isotropic homogeneous hydraulic conductivities were created for the dual-porosity models, similar to the approach in the 2-D DFN study. When the flow fields produced the same Darcy velocities as in the DFNs, transient transport MT3DMS models with dual-porosity mass transfer were created.

The maximum mass discharges from each 3-D DFN model were extracted from the HGS's mass balance and scaled to the coarse-grid source area, as described in Section 3.2.1.2. The resulting source concentrations for the EPM models are listed in Table 3.4. The semi-analytic and the dual-porosity source areas consist of two gridblocks vertically and two gridblocks laterally centered at the inlet of each DFN model. The transient plume mass of the DFN and the semi-analytic models were compared at the end of each transport simulation to ensure the specified initial concentration in the coarse-grid model produced the same plume mass as the DFN model over time.

To replicate the DFN concentration contours, vertical dispersivities were added in the EPM models. Transverse dispersivities were computed as ten times the vertical dispersivities. Transverse and vertical dispersivities for each semi-analytic model are listed in Table 3.4. The rest of the transport parameters were the same as shown in Table 3.1, including the fixed timestep, loading time, unloading time, porosities, and tortuosities.

Table 3.4: Transport parameters for semi-analytic and dual-porosity models.

a, m	0.613	1.18	4.30
C_0, g/L	0.12	0.11	0.16
α_y, m	0.04	0.08	0.5
α_z, m	0.004	0.008	0.05
A_{md}, m^2	41	21	4
L_{md}, m	0.306	0.592	3.2
Runtime[a], $mins$	5	5	9
β (initial), $1/yr$	0.013	0.0035	2.7e-4
β (calibrated), $1/yr$	-	-	6e-4
Runtime[b], $mins$	7	7	8

[a] Semi-analytic [b] Dual-porosity

The semi-analytic and dual-porosity models differed in their matrix diffusion parameters. For the semi-analytic models, the matrix diffusion lengths L_{md} and areas A_{md} were computed as explained in Section 3.2.1.2. The semi-analytic models ran for less than ten minutes. For the dual-porosity transport models, initial mass transfer coefficients were computed using the fracture spacing listed in Table 3.3 and Equation 3.5. Calibration was not required for the smaller fracture spacing cases but it was necessary for the largest fracture spacing case (Table 3.4). The dual-porosity

runtimes were similar to those of the semi-analytic models.

We used the same comparison metrics as in the 2-D DFN study to compare the 3-D DFN models with the semi-analytic and the dual-porosity models. Equation 3.6 and Equation 3.7 were utilized to compute the mass discharges with the presence of transverse fractures. For the longer plumes in the smaller fracture spacing models, the mass discharges were computed at 12 cross-sections along the length of the plume. For the largest fracture spacing case, the plume was shorter so we only compared mass discharges at seven cross-sections. NRMSEs were calculated to assess the difference between the coarse-grid EPM models and the DFN models at each cross-section.

3.3.2 3-D DFN Results

3.3.2.1 Small fracture spacing cases

Coarse-grid mass discharges normalized to the maximum mass discharge of the DFN are compared to the DFN mass discharge for the smallest fracture spacing case (0.6 m) in Figure 3.6. The 3-D DFN mass discharge behavior (circle markers) was similar to the behavior of the 2-D DFN mass discharge, with a rising profile during the loading period and a lowering profile with a long tail in the unloading period. At 8.5 m from the inlet, the DFN mass discharge peak was nearly 90% of the maximum mass discharge. That peak dropped to below 70% at 17.5 m and to 10% at 148.5 m.

The semi-analytic model (red solid lines) replicated the overall DFN mass discharge well for all of the cross-sections, especially the long tails due to matrix diffusion. The semi-analytic model underestimated the peaks by a few percentage points but on average, maintained a low NRMSE of 2%. The dual-porosity mass discharge at this fracture spacing simulated the DFN mass discharge fairly well at a NRMSE of 4% without any calibration needed. The model underestimated the DFN mass discharge more often than the semi-analytic model so its marginal NRMSE doubled. This observation is consistent with the findings in our study of 1-D parallel fractures (Pham & Falta, 2022), where the dual-porosity model also matched an analytical solution (Sudicky & Frind, 1982) well at small fracture spacing.

Figure 3.7 shows the same comparison for a 3-D DFN with twice the fracture spacing (1.2 m). This DFN model had less fractures, which translated to a lower volume fraction, a lower Darcy velocity, and a somewhat lower linear velocity. The plume's center of mass at this fracture spacing moved at a slower pace than the plume in the 0.6-m fracture spacing model. In the smaller fracture

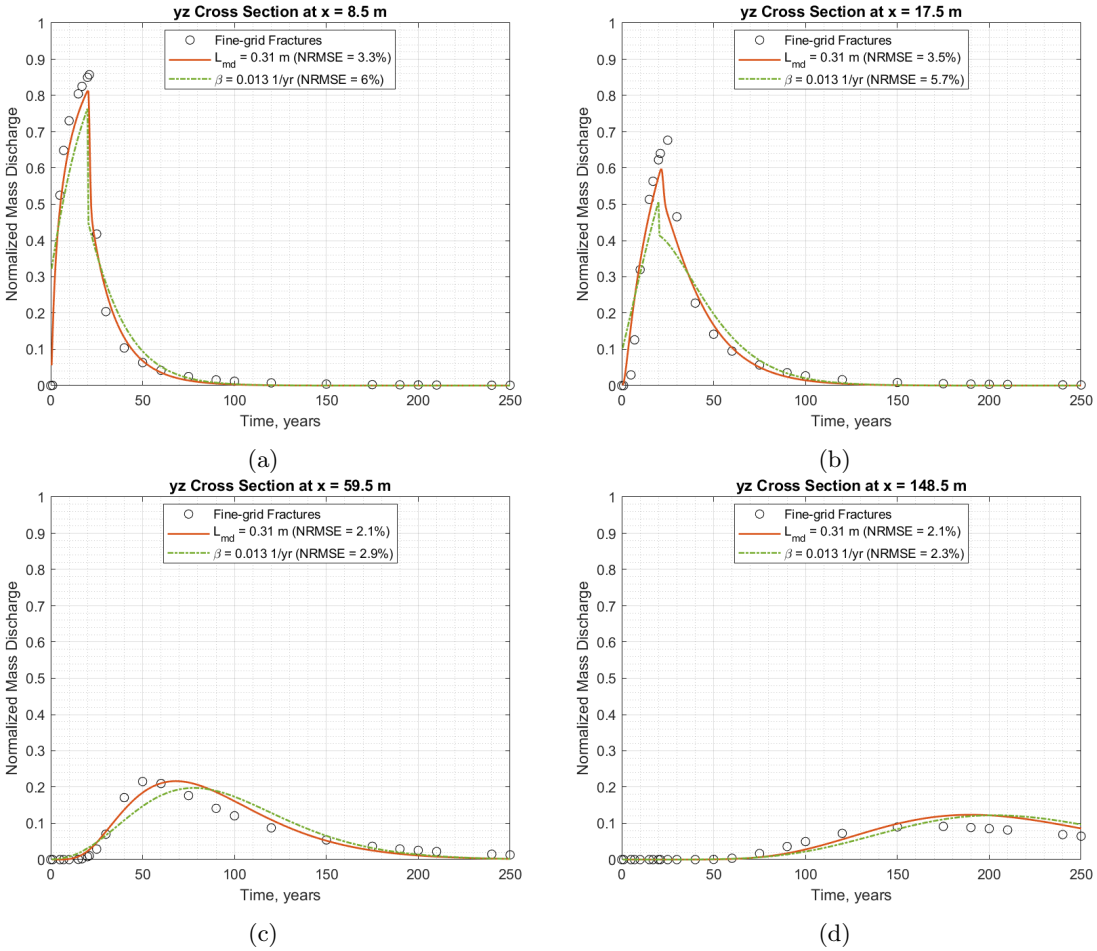

Figure 3.6: Semi-analytic (red solid lines), dual-porosity (green dashed line) and 3-D DFN (circles) mass discharges over four cross-sections at fracture spacing of 0.6 m. Semi-analytic marginal NRMSE is 2%, and dual-porosity marginal NRMSE is 4% (without calibration) over 12 cross-sections (only four are shown).

spacing case, it took 148.5 m before the DFN mass discharge dropped to 10% of the maximum mass discharge (circle in Figure 3.6d) while in this larger fracture spacing case, it took only 59.5 m (circle in Figure 3.7).

The semi-analytic model provided a reasonable match to the DFN model with a average NRMSE of 2% (red lines in Figure 3.7). To keep the dual-porosity NRMSE low over 12 vertical cross sections along the length of the plume, the dual-porosity model was calibrated to a β of 0.0035/yr. At this mass transfer coefficient for a 3-D DFN with fractures at 1.2 m, the dual-porosity model (green dashed lines in Figure 3.7) appeared to simplify the gradient of the discharge to a linear function of time. While the dual-porosity mass discharge overlapped with the DFN model's at some

times, its average NRMSE was twice as high as the semi-analytic model. The dual-porosity mass transfer coefficient was calculated from Equation 3.5, and calibration was completed via trial and error.

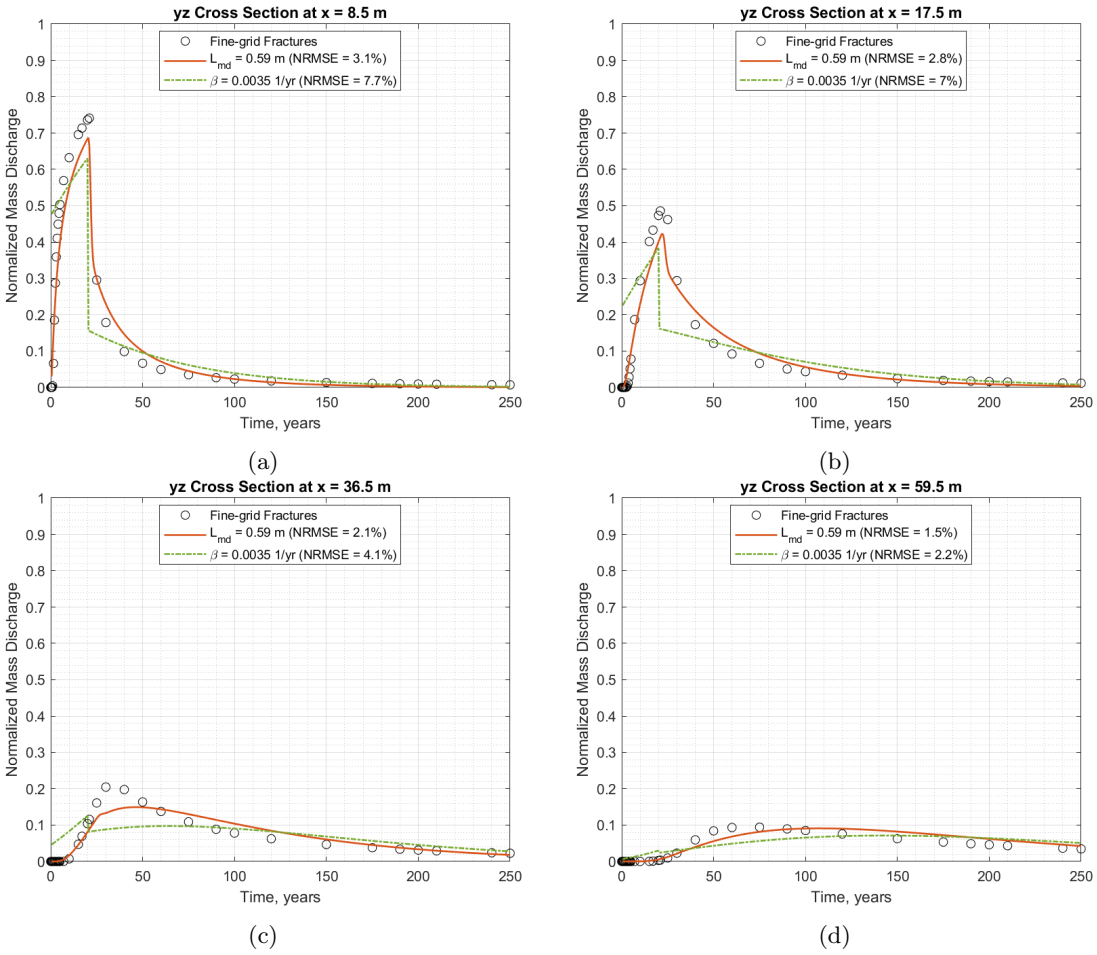

Figure 3.7: Semi-analytic (red line), dual-porosity (green dashed line) and 3-D DFN (circle) mass discharges over four cross-sections at fracture spacing of 1.2 m. Semi-analytic marginal NRMSE is 2%, and dual-porosity marginal NRMSE is 4% (without calibration) over 12 cross-sections (only four are shown).

3.3.2.2 Large fracture spacing case

For a DFN model at 4.3-m fracture spacing , the longitudinal spread of the DFN plume was the shortest as indicated by DFN mass discharge peak dropping to 10% of the maximum discharge within 36.5 m (Figure 3.8d). The large matrix volume provided significantly more matrix volume for mass storage and reduced linear velocity, which shortened the extent of the plume in the fractures.

Other aspects of the DFN mass discharge profile were similar to the profiles with smaller fracture spacing.

The semi-analytic mass discharge peak was close to the DFN peak at the 8.5-m cross-section. Some underestimation of the mass discharge peaks occurred at other cross-sections but the model maintained an average NRMSE of 4%. While the dual-porosity models had performed adequately in the smallest fracture spacing case, it did not simulate matrix diffusion well in the 4.3-m fracture spacing case, even with calibration. The dual-porosity mass discharge is shown as the green dashed line in Figure 3.8.

The semi-analytic model appears to be a more robust alternative than the dual-porosity model over a range of fracture spacing. The semi-analytic model captured the non-linear behavior of matrix diffusion in the DFN while maintaining a lower marginal NRMSE. The semi-analytic parameters were computed directly from the properties of the DFN. The dual-porosity model had performed adequately at smaller fracture spacing but as the fracture spacing increased, the model was unable to simulate the non-linear plume tailing behavior of the DFN via a first-order mass transfer coefficient, even with calibration.

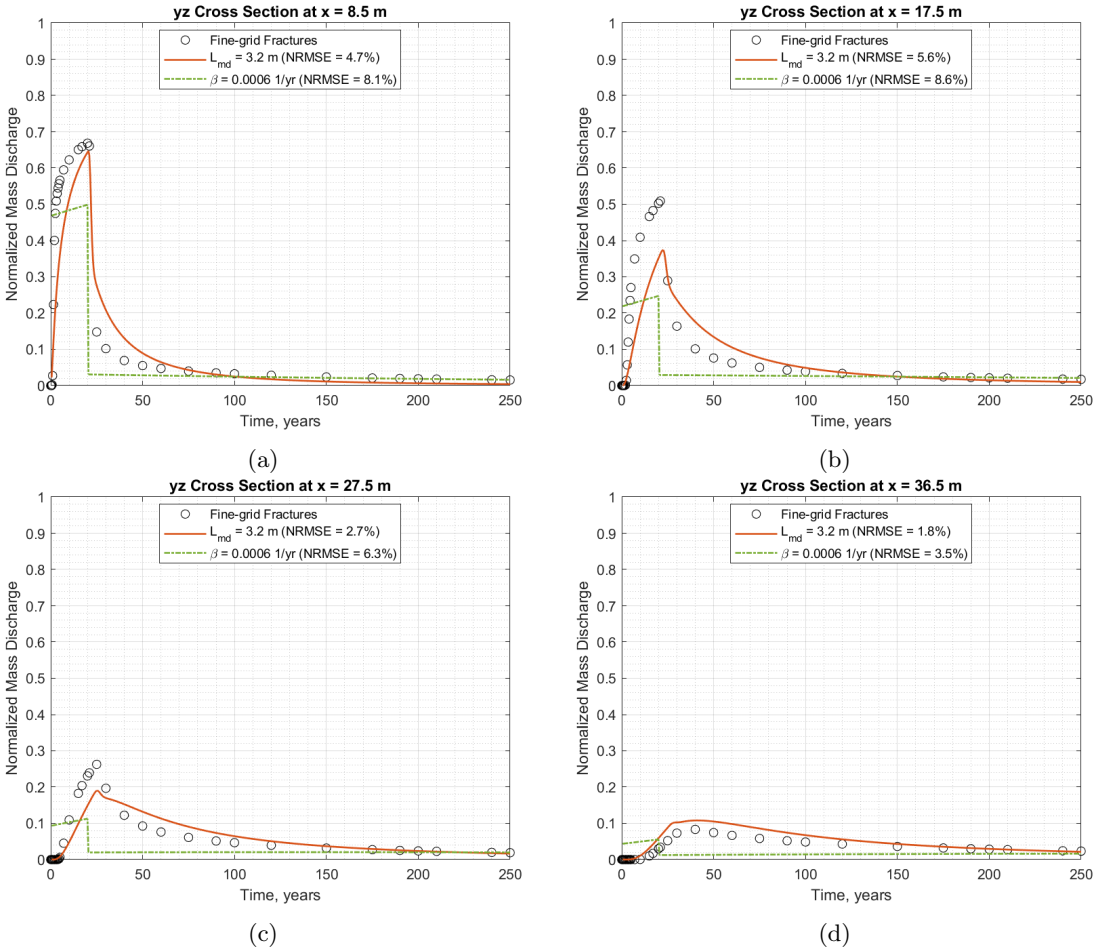

Figure 3.8: Semi-analytic, dual-porosity, and DFN model mass discharges over four cross-sections at fracture spacing of 4.3 m. Semi-analytic marginal NRMSE is 4%, and dual-porosity marginal NRMSE is 6% (calibrated) over seven cross-sections (only four are shown).

3.3.2.3 Concentration contours

We cut a horizontal slice at the center of the 1.2-m fracture spacing plume to study more closely the concentration contours in comparison with the coarse-grid models. The three panels of Figure 3.9 show DFN, semi-analytic, and dual-porosity contours over three time periods of 20, 60, and 100 years. The plume advanced between 80 m and 100 m after 20 years, with the highest concentrations in the 0.01 to 0.1 g/L range (orange contours) present in the first 50 m of the plume's length. At 60 years, the higher concentration contours began to disappear in response to 40 years of clean water flushing after a complete source removal. At 100 years, other than in a few isolated fractures at the inlet, only the concentrations lower than 0.01 g/L were present in the DFN model.

The semi-analytic model simulated both the DFN contours within a few meters of the DFN plume length for all three time periods and over several orders of magnitude of the concentration. The concentrations for the DFN contours were produced after seven hours of simulation time while the semi-analytic concentrations were obtained in less than 10 minutes. The dual-porosity concentration contours were not as close to the DFN model's contours compared to the semi-analytic model's. The dual-porosity model over-predicted the extent of the lower concentrations in the first two time periods. At 20 years, it only matched with the DFN contours in the 0.01 to 0.1 g/L range. The match improved at 60 years, when the match was adequate up to 0.0001 g/L. At 100 years, the dual-porosity performed similarly to the semi-analytic method. The comparison of the contours indicated that the use of the dual-porosity model may be appropriate at large simulation times.

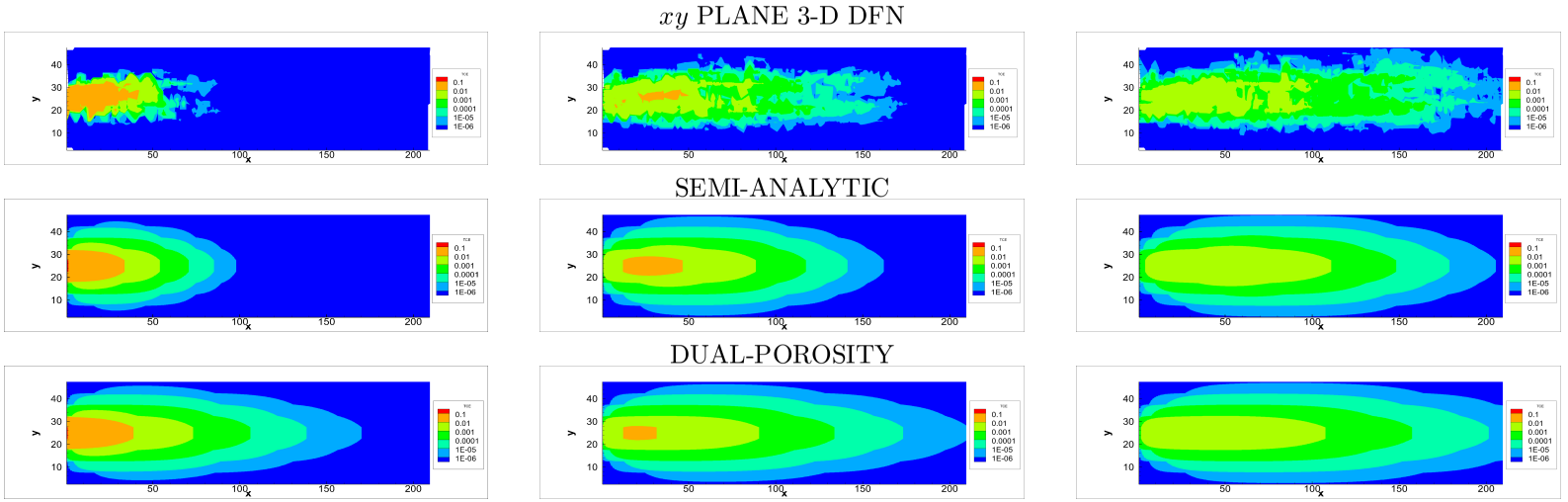

(a) t = 20 years (b) t = 60 years (c) t = 100 years

Figure 3.9: xy Concentration contours of 3-D DFN and coarse-grid EPM models at fracture spacing case of 1.2 m.

3.4 Conclusion

Transient transport models were simulated in 2-D and 3-D discrete fracture networks using fine-grid HGS and coarse-grid EPM models. Dual-porosity and semi-analytic models were evaluated on their capability to match outputs from the DFN models. The dual-porosity and the semi-analytic models took a few minutes to simulate matrix diffusive transport compared to several hours for the DFN models. When matrix diffusion was simulated in a 2-D discrete fracture network with fractures at an average spacing of about a meter, the dual-porosity approximation was generally unable to give mass discharge profiles matching the DFN profiles, even with calibration of the mass transfer coefficient. Meanwhile, the semi-analytic model replicated the DFN mass discharge curves well over all distances.

In a series of 3-D DFN models, the dual-porosity model performed well when the fracture spacing was less than a meter, using a mass transfer coefficient computed via a shape factor formula (van Genuchten, 1985). When the fracture spacing increased to a few meters, the dual-porosity gave high NRMSEs, similar to the 2-D DFN case. The semi-analytic model was able to simulate DFN mass discharges and concentration contours with low errors in all of the 3-D DFNs.

The semi-analytic model appears to be a robust EPM model for simulating matrix diffusion in fractured porous media. A key advantage of this approach is that its modeling parameters can be directly computed using fracture network properties. Currently, the semi-analytic model is being incorporated into MODFLOW 6 (Langevin et al., 2022) and MODFLOW-USG (Panday et al., 2013) to simulate matrix diffusion in 3-D unstructured grids with variable flow fields.

Chapter 4

Granular Heterogeneous Media

4.1 Introduction

Matrix diffusion is a critical transport process in not only fractured media but also in granular heterogeneous media. The contrast in permeabilities between the fractures and the matrix is analogous to the permeability contrast between high-permeability (high-K) and low-permeability (low-K) materials in a granular aquifer. The word "matrix" in this context refers to materials such as silts and clays.

In a heterogeneous sand-gravel aquifer, the presence of low-K materials, often in longitudinal lens at sporadic locations, can add significant clean-up time (Mackay & Cherry, 1989) in comparison to a uniform sand-gravel aquifer. Similar to the matrix in fractured media, the low-K lenses act as storage location for the contaminant to diffuse into. When the concentration gradient is reversed, the contaminant gradually moves back out from the low-K materials into the high-K groundwater flow paths. The diffusion time scale is much slower than the advective and dispersive time scales, potentially causing the concentration in the plume to be above regulatory standards for decades (Gillham et al., 1984; B. L. Parker et al., 1994; Esposito & Thomson, 1999; Chapman & Parker, 2005; Sale et al., 2008; B. L. Parker et al., 2012; Seyedabbasi et al., 2012; Falta & Wang, 2017; Muskus & Falta, 2018; Farhat et al., 2020; Pham & Falta, 2022).

The need to accurately depict matrix diffusion can be as important in heterogeneous granular media as in fractured media. Efforts to model matrix diffusion in the literature were initially overlooked because of the emphasis on solving for only the advective and the dispersive fluxes

in isotropic and homogeneous aquifers (Hadley & Newell, 2014). However, the underestimation of clean-up time in sand-silt or sand-clay settings eventually led researchers to explicitly consider matrix diffusion.

Many analytical solutions for fracture-matrix systems can be applied for heterogeneous granular media. For example, 1-D analytical solutions by Crank (1975) can be applied in a stratified sand-aquitard setting where the aquitard can be conceptualized as a finite or semi-infinite matrix. Another example is Sudicky et al. (1985) and Starr et al. (1985) applying analytical solutions for matrix diffusion in a single fracture to layered granular media where the porosity of the high-K material is less than one. Some analytical solutions unique to granular material exist such as one by C. Liu and Ball (1998) for a two-layer porous media, in which they applied Green's function and the binomial theory in a Laplace domain. More recently, Yang et al. (2015) developed analytical and experimental approaches to study reactive and nonreactive transport in a thin aquitard bounded by an adjacent aquifer. Experiments were performed in a 2-D flow chamber with a high-K aquifer on top of thin clay layers of varying thicknesses. The authors applied the method of images to adapt a 1-D analytical solution of diffusion in a semi-infinite low-K material to a finite aquitard. Yang et al. (2017) expanded on that solution by including a power law model for the source function, allowing the source to be controlled as a step-function, as an exponential function or as a linear function of the initial concentration. Yang et al. (2019) found that solution to match better with measured data in flow chamber experiments than the historical semi-infinite analytical solution (Carslaw & Jaeger, 1959).

Similar to our findings from the literature reviews in sections 2.1 and 3.1, we learned that analytical solutions are very useful in some specific systems but they are rarely in 3-D and often require assumptions about the geometry of the low-K materials. For more realistic settings at field scale, numerical models are often required. The large numerical codes such as MT3DMS (Zheng & Wang, 1999; Aquaveo, 2019) and HydroGeoSphere (Therrien & Sudicky, 1996; Aquanty Inc., 2021), which we applied extensively in previous studies in fractured media, are adaptable to heterogeneous porous media. However, their applications in granular media are constrained by the same computational limits as in the fracture-matrix systems. Matrix diffusion occurs over a small length scale so to capture it in large numerical models, the spatial discretization must be very fine, which leads to long simulation times (Chapman et al., 2012).

For this study of matrix diffusion in heterogeneous granular media, we utilize the two equiv-

alent porous media (EPM) models we had used previously: the dual-porosity and the semi-analytic models. EPM models have proven to be a good compromise between analytical solutions and numerical models while requiring a fraction of the computational demands of fine-grid numerical models (Long et al., 1982; Pankow et al., 1986; Berkowitz et al., 1988; Schwartz & Smith, 1988; McKay et al., 1993; Falta & Wang, 2017; Muskus & Falta, 2018; Pham & Falta, 2022).

The semi-analytic model has been shown to be a more robust EPM model than the dual-porosity model in parallel fractures (Chapter 2) and in discrete fracture networks (Chapter 3). We continue the comparison between the two EPM models by applying them in the 3-D heterogeneous media transport model by Muskus and Falta (2018). The rest of this chapter is organized as follows: in Chapter 4.2, we review how Muskus and Falta (2018) simulated flow and transport in two unique distributions of sand and clay layers. We also describe how EPM models are created to approximate matrix diffusion in the 3-D heterogeneous model, including the addition of dual-porosity models to the comparison. In Chapter 4.3, we present the results of the comparison between the fine-grid model outputs and the EPM approximations in terms of the outlet mass discharges and concentration contours.

4.2 Methods

Two highly heterogeneous simulations of a sand-clay system were created using the Transitional Probability Geostatistical Software (TPROGS) (Carle, 1999; Muskus & Falta, 2018) as implemented in the graphical user interface GMS by Aquaveo (2019). 84 synthetic boreholes were analyzed using TPROGS and Markov Chains to generate conditional simulations of sand-clay material cross sections. Inputs such as the lag spacing i.e. the distance between nearby pair of geological facies, the material proportion, and the lens length were set to build the Markov Chains. Following the creation of the Markov Chains, a series of conditional simulations based on the synthetic boring logs were generated and tested to ensure the resulting flow and transport models fit the physical boundaries of the system and that the computational time was reasonable (Muskus & Falta, 2018).

The results of the TPROGS simulations were two fine grid configurations. In one case, called the "lens case," Muskus and Falta (2018) generated a subsurface that consisted of long horizontally connected sand zones. In another case, called the "random case," they created a subsurface architecture with more random but spatially correlated material distributions.

The two simulations shared the same grid dimensions: 1052.9 m in x-direction with 101 gridblocks, 615.7 m in y with 70 gridblocks, and 41.15 m in z with 400 gridblocks. There were a total of 2,828,000 gridblocks in the model.

4.2.1 Fine grid models

Using the parameters in Table 4.1, TPROGS generated a material distribution consisting of horizontally elongated sand zones (lens case) and another distribution (random case) where the distribution was more randomized. The volume of sands in the random case model was increased from 0.29 to 0.35 to promote more flow through the model. The thickness of the sand layers were the same in both models. In the random case, sand lens ratios were reduced to 18 m in the horizontal (x) direction and to 7.5 m in the dip (y) direction. The lens ratios of the clay materials were also decreased.

Parameter	**Lens case**		**Random case**	
	Sand	**Clay**	**Sand**	**Clay**
Proportion	0.29	0.71	0.35	0.65
Lens length in z, m	0.61	2.73	0.61	2.73
Lens ratio in x	118.67	65.5	18	7.47
Lens ratio in y	10	5.52	7.5	3.11

Table 4.1: TPROGS parameters for lens and random case (Muskus & Falta, 2018)

The two material distributions are as shown in Figure 4.1. To create a flow field for both models, the hydraulic conductivity was set at 9.14 m/d for sand and $3.05 * 10^{-4}$ m/d for clay. At the upstream and downstream end of the model, two head boundary condition were imposed to produce a head gradient of 0.01. The MODFLOW flow simulations took 17 minutes on an Intel i7 CPU 3.60 GHz desktop computer, producing two steady-state, 3-D, heterogeneous, and anisotropic flow fields. The average Darcy velocity in the lens case was 5.62 m/yr whereas in the random case, it was 2.70 m/yr. The demotion of longitudinal lenses parallel to flow in the random case reduced the interconnectivity and the Darcy velocity through the model.

Two MT3DMS transport models were set up, one for each material distribution. A TCE source of 10 mg/l was placed 156 m downstream from the inlets of both models. Advection and molecular diffusion were considered but mechanical dispersion was kept at a minimum. The source was not placed at the inlet because it caused excessive lateral dispersion. In the lens case, the source area consisted of 18 gridblocks of the model and was maintained at a constant concentration of 10

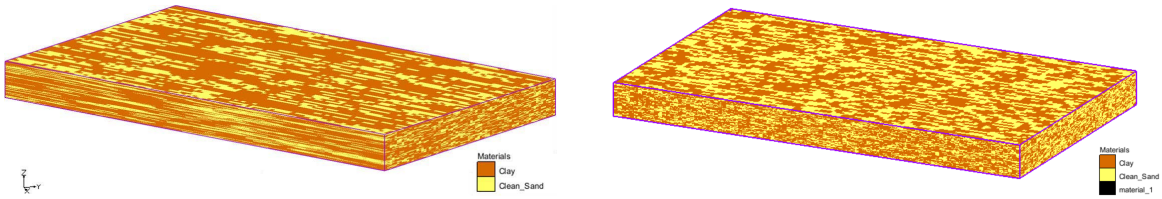

(a) (b)

Figure 4.1: Material distribution from TPROGS for: (a) lens case and (b) random case (Muskus & Falta, 2018)

mg/l for 30 years. Then, the source was removed, and clean water was flushed through the system for 200 years. In the random case, the source area was placed in 28 gridblocks and the flushing period was extended to 400 years.

The advective terms in both models were solved using upstream weighting. The timestep was set to 0.02 years in the lens case and 0.5 years in the random case because of the longer flushing period. Retardation and decay were not considered. Flow and transport parameters are listed in Table 4.2.

Distribution	**Lens**		**Random**	
Parameter	**Sand**	**Clay**	**Sand**	**Clay**
Porosity, ϕ^*	0.3	0.5	-	-
Hydraulic conductivity, K*	0.61 m	2.73 m	-	-
TCE source concentration, C_0^*	10 mg/l	0 mg/l	-	-
Effective diffusion coefficient, D*	0.025 m^2/yr			
Maximum hydraulic head, h_{max}	77.61 m			
Minimum hydraulic head, h_{min}	67.35 m			
Δt	0.02 years		0.5 years	
Loading period	30 years		30 years	
Unloading period	200 years		400 years	

* Same parameters used in lens and random cases

Table 4.2: Parameters used in MODFLOW and MT3DMS models (Muskus & Falta, 2018)

After the flow fields were generated, the MT3DMS simulations for the loading period of the lens case ran for 6-8 hours and for 8-10 hours in the random case. The unloading periods ran for 45 hours in the lens case and 60 hours in the random case.

4.2.2 Equivalent porous media (EPM) models

Dual-porosity and semi-analytic models were set up using a coarser and more computationally efficient EPM grid to simulate transport in the lens and random material distributions. Data

inputs for the dual-porosity EPM models were entered using the graphical user interface GMS by Aquaveo (2019). The semi-analytic coarse grid models were ran using the Fortran executable of the method, and data inputs were entered using a text file. SERDP and ESTCP host the Fortran executable and the optional graphical user interface REMChlor-MD in a repository online (Farhat et al., 2018).

The dimensions of the EPM gridblocks were computed by doubling the x and y spacing of the gridblock spacing in the fine grid model. Vertical spacing in the random case was larger than in the lens case to accommodate additional source cells in that model. Table 4.3 lists the coarse grid spacing for both cases. The potential time saving is apparent from the difference in the number of gridblocks between the fine grid and the coarse grid model.

Parameter	**Fine**	**Lens Coarse**	**Random Coarse**
dx, m	10.42	20.85	20.85
dy, m	8.8	17.59	17.59
dz, m	0.1	1.85	2.88
Gridblocks	2,828,000	6,966*	9,632*

*assuming symmetry about y = 0

Table 4.3: Coarse grid dimensions

Both the coarse grid dual-porosity and semi-analytic flow simulations were implemented under the assumption of a homogeneous and uniform velocity flow field. For the dual-porosity models, MODFLOW simulations were created with the same head gradient of 0.01 as the fine grid's. The head gradient was imposed by placing two head boundary conditions at the inlet and the outlet of the EPM dual-porosity models. Calibration of the hydraulic conductivity was implemented via trial and error until the average Darcy velocity of the EPM dual-porosity models matched the fine grid's. The calibrated hydraulic conductivity for the lens case was 549.1 m/yr and 263.7 m/yr for the random case. The MODFLOW models were run at steady state, and because of the coarser grid, the flow fields were produced nearly instantaneously. For the semi-analytic models, the Darcy velocities were direct inputs.

Two average source concentrations were designed to produce the same source mass discharges in the EPM models as in the fine grid's (Muskus & Falta, 2018). The EPM source concentration for the lens case was 4.3 mg/l and 6.4 mg/L for the random case. The EPM source concentrations were placed in a single coarse source cell, which is symmetrical about the y-axis. The EPM models only capture the plume with the source placed at the inlet so the overall length of

the models was shortened to 896 m. EPM models maintained the same source step-function with a loading period and an unloading period as in the fine-grid models. In the semi-analytic model, the step-function behavior of the source is built-in and was activated by simply setting parameter Γ to zero. For the dual-porosity models, two transport models were required to simulate the step-function behavior of the source for each mass transfer coefficient. A loading dual-porosity transport model was created first, and the concentration outputs from that model were used as the initial conditions for the unloading dual-porosity transport model.

Same as the fine grid models, both EPM dual-porosity and semi-analytic models considered advection and molecular diffusion, while keeping mechanical dispersion at a minimum. The advective terms were calculated using the finite difference method with upstream weighting in both EPM models. Muskus and Falta (2018) calibrated the dispersivities to match the plume outlines of the lens case fine grid model so those dispersivities were used in the dual-porosity and semi-analytic coarse grid model. The dual-porosity MT3DMS mass balance equations were solved iteratively using a conjugate gradient method with a symmetric successive over relaxation preconditioning factor of 1.0 while the semi-analytic model utilized the Gauss Seidel iterative method. The convergence criterion in both coarse grid models was set to $1 * 10^{-4}$. For both the lens and the random cases, a timestep refinement study was implemented to ensure that prior to the simulations of diffusive effects, the outputs from the two coarse grid models were identical (Muskus & Falta, 2018). The results from those studies indicated a timestep of 0.1 years for use in the lens case EPM models and a timestep of 0.04 years in the random case EPM models.

To simulate matrix diffusion in MT3DMS using the dual-porosity approach, the built-in option to utilize a mass transfer coefficient was activated (Zheng & Wang, 1999; Aquaveo, 2019). An initial mass transfer coefficient was estimated using an analytical expression (Haggerty & Gorelick, 1995; Guan et al., 2008): $\beta = \frac{\phi_{im}\tau_l D}{L_{md}^2}$, where L_{md} is the same as the diffusion length in the semi-analytic model. However, for both the lens and the random cases, the initial mass transfer coefficient required calibrations via trial and error. A series of dual-porosity transport models were simulated in MT3DMS (Deans, 1963; Coats & Smith, 1964; Zheng & Wang, 1999; Zheng & Bennett, 2002) for each mass transfer coefficient in each material distribution case.

The dual-porosity models also require inputs of the mobile and immobile porosities to specify the degree of heterogeneity in the two domains. Those two parameters were computed directly using the sand porosity, the clay porosity, and the volume fraction from the TPROGs simulations. Using

Equation 2.3 and 2.4, the mobile and immobile porosities were computed to be 0.0864 and 0.356 respectively in the lens case. In the random case, the mobile porosity was 0.105, and the immobile porosity was 0.325. Each dual-porosity transport model ran for about 4 minutes, including both loading and unloading models, on a high-performance laptop with an Intel i7 2.80Ghz processor.

For the semi-analytic models, matrix diffusion simulation requires inputs of the volume fraction, the diffusion length, and the diffusion area. The volume fraction was known from TPROGS material distributions. The diffusion length was estimated in each material distribution case by randomly selecting three lateral faces of the fine-grid model and approximating the thickness of the clay layers in a series of synthetic boreholes (Muskus & Falta, 2018). A total clay thickness for each lateral face was computed as a volumetric weighted average of the individual thickness measurements. Because the clay lens are typically in contact at the top and the bottom with sand layers, the diffusion into the clay from both directions was assumed to meet in the middle of the clay lens. So, the diffusion length was computed as half of the average clay thickness for each lateral face. The average of the three diffusion lengths was 1.85 m for the lens case and 1.21 m for the random case. Knowing the volume fraction and the average diffusion length, the diffusion areas were computed directly using Equation 2.17 to be 261 m^2 for the lens case and 567 m^2 for the random case. Each semi-analytic model ran for 1 minute and 9 seconds using the Intel i7 2.80Ghz processor computer used for the dual-porosity models.

To objectively evaluate the effectiveness of the calibrating parameters, the root-mean-square-errors (RMSEs) between the outlet EPM mass discharge and the fine grid model's were computed. Those RMSEs were then normalized by the source mass discharge, resulting in a NRMSE between 0 and 1. The mass discharges were computed similar to the procedure shown in Section 3.2.1.4. NRMSEs were computed for each dual-porosity model in comparison to the fine-grid discharges to determine the one producing the lowest NRMSE in each material distribution case.

4.3 Results

4.3.1 Mass discharge comparisons

The outlet mass discharges of the EPM models were compared against the fine grid's. In Figure 4.2, mass discharges for a series of dual-porosity models over a range of mass transfer coefficient are shown for both material distributions.

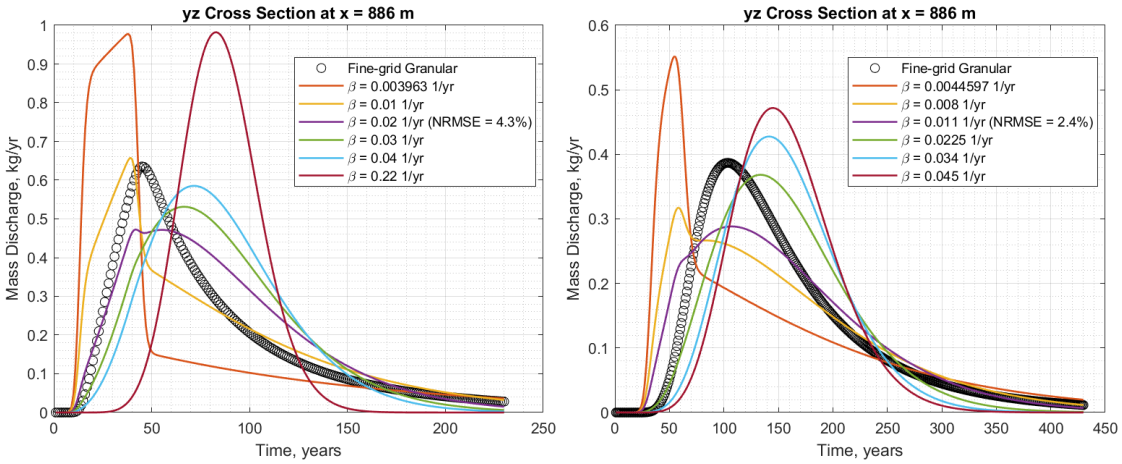

(a) Lens case

(b) Random case

Figure 4.2: Range of β in calibrations of dual-porosity models. Panels (a) and (b) are of different mass and time scales.

The overall behavior of the fine-grid mass discharge profiles were similar. For both material distributions, the fine-grid mass discharge (black circle markers) rose over a loading period and dropped in an unloading period with long tailing of the discharges until the end of the simulations. The lens case had a peak mass discharge value of 0.64 kg/yr that occurred at t = 50 years whereas the random case's peak mass discharge was just below 0.4 kg/yr at t = 100 years. The lack of interconnected sand lens parallel to flow reduced the flow and the amount of mass in the random case.

The solid purple lines show the calibrated dual-porosity mass discharges in the two material distributions with the lowest NRMSEs, which were produced by the mass transfer coefficient of 0.02 $1/yr$ in the lens case and of 0.011 $1/yr$ in the random case. Other solid lines are calibrations of the dual-porosity model, where the mass transfer coefficient varied over two orders of magnitude in the lens case and over an order of magnitude in the random case. The larger the mass transfer coefficient, the more contaminant mass diffused from the high-permeability layers to the low-permeability layers, causing the peak of the dissolved mass discharge curve to gradually drop. Very large mass transfer coefficients simulated fast mass exchange between the low-K and the high-K domains and diminished the role of matrix diffusion. Profiles of systems with fast mass exchange and high mass transfer coefficients were more Gaussian than others, as evidenced by the green, cyan, and burgundy solid lines.

The dual-porosity model was unable to match the fine-grid mass discharge because it as-

sumes that the mass transfer process between the high-K and the low-K domains follows a linear force model (Bear & Cheng, 2010; Pham & Falta, 2022). For some systems, the linear force model does not give accurate results until simulation time has reached decades to hundreds of years (Pham & Falta, 2022). Because of this time-dependency, one mass transfer coefficient cannot accurately simulate mass discharge at all times. Table 4.4 reports the NRMSEs for all the cases. The initial estimates of the mass transfer coefficient, 0.004 $1/yr$ and 0.0045 $1/yr$, were computed based on an analytical expression of the coefficient in the literature (Haggerty & Gorelick, 1995; Guan et al., 2008) but their NRMSEs were high so additional dual-porosity transport models were simulated in trial and error calibrations.

Lens case						
β, **1/yr**	0.004	0.01	0.02	0.03	0.04	0.22
NRMSE	16%	6%	4%	7%	9%	19%
Random case						
β, **1/yr**	0.0045	0.008	0.011	0.0225	0.034	0.045
NRMSE	7.7%	3.9%	2.4%	2.7%	4.3%	5.3%

Table 4.4: NRMSEs of dual-porosity models

Only the dual-porosity models with the lowest NRMSEs were compared to the semi-analytic and the fine-grid models in Figure 4.3.

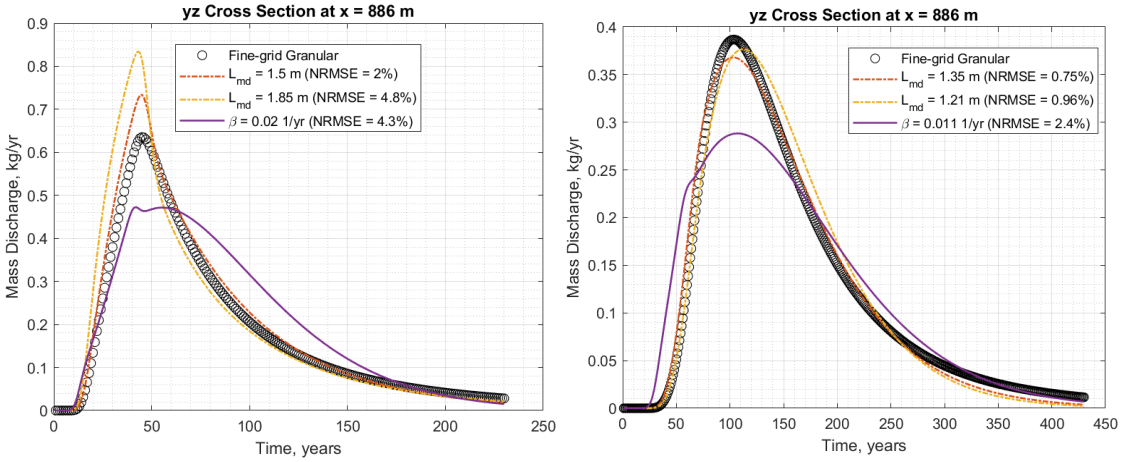

(a) Lens case

(b) Random case

Figure 4.3: Comparing mass rates of EPM semi-analytic and fine-grid models. Panels (a) and (b) are of different mass and time scales.

The uncalibrated NRMSE semi-analytic model in the lens case (dashed-dot red line in Figure 4.3a) was within 0.5% of the dual-porosity NRMSE (purple line), which was only attained after a

series of calibrations. The uncalibrated semi-analytic model performed even better in the random case where its NRMSE was less than half of the calibrated dual-porosity model's NRMSE (Figure 4.3b).

Qualitatively, the semi-analytic mass discharge profiles were more satisfactory because they closely followed the long tailing behavior of the fine-grid models. To improve the semi-analytic match, a single instance of the diffusion length (dashed-dot yellow lines in Figure 4.3) was iterated for each material distribution case. The calibrated semi-analytic model in the lens case halved the NRMSE and moved the peak mass discharge closer to the fine-grid model's. In the random case, the calibrated diffusion length had an error an order of magnitude smaller than the calibrated dual-porosity model's NRMSE.

Between the two EPM models in two TPROGS material distributions, the semi-analytic model appeared to be a better choice in simulating matrix diffusion. It produced an adequate match to the fine-grid model with matrix diffusive parameters directly computed. Within a single calibration, the semi-analytic model improved its match with the fine-grid model. Meanwhile, the dual-porosity model required several iterations of the mass transfer coefficient to produce quantitatively comparable matches.

4.3.2 Concentration contours

Muskus and Falta (2018) compared dissolved concentration contours between fine-grid and semi-analytic models. Expanding on their work, we added dual-porosity concentration contours to the visualizations of the fine-grid and the EPM models concentration contours using Tecplot360 (Tecplot Inc., 2020). The top three rows of Figure 4.4 show the lateral spread of the plume over 30 to 130 years as simulated by the fine-grid, the dual-porosity, and the semi-analytic models. The bottom three rows show the vertical spread of the plume.

The highest concentration contours (greater than 1000 $\mu g/L$) were present within the first 200 m of both material distributions after 30 years of source loading. Those high concentrations were flushed out after 100 years of a clean water flush. Due to the lack of material lens parallel to flow, the random case plume's lateral spread was more significant than the lens case's. The random case had a deeper vertical spread, extending over 40 m below the surface.

While the semi-analytic mass discharges were more accurate than the dual-porosity mass discharges, the concentration contours of the two models over log cycles of the concentrations were

similar. Both models appeared to overpredict the longitudinal extents of the 1000 $\mu g/L$ contours because only a slice of the fine-grid xy contours was plotted while several superimposed slices from the fine-grid models are needed to be analogous to a single EPM slice. Some differences are expected between the EPM contours, which give averaged extents of the plume in more discretized grids. When Muskus and Falta (2018) superimposed a number of fine-grid layers, the aggregated contours were similar to the semi-analytic contours.

The comparison of the contours validated the effectiveness of the EPM models in approximating complex transport in fine-grid models. The EPM models were able to recreate the overall features of high-resolution contours from fine-grid models that took tens of hours to simulate. The efficiency of EPM models is useful when timely decisions are required in the planning phase of a remedial strategy. Between the two EPM models, the semi-analytic model required the least effort in calibration. Given the accuracy of the semi-analytic model without calibration, it appears to be an ideal EPM choice to be applied at matrix diffusion sites.

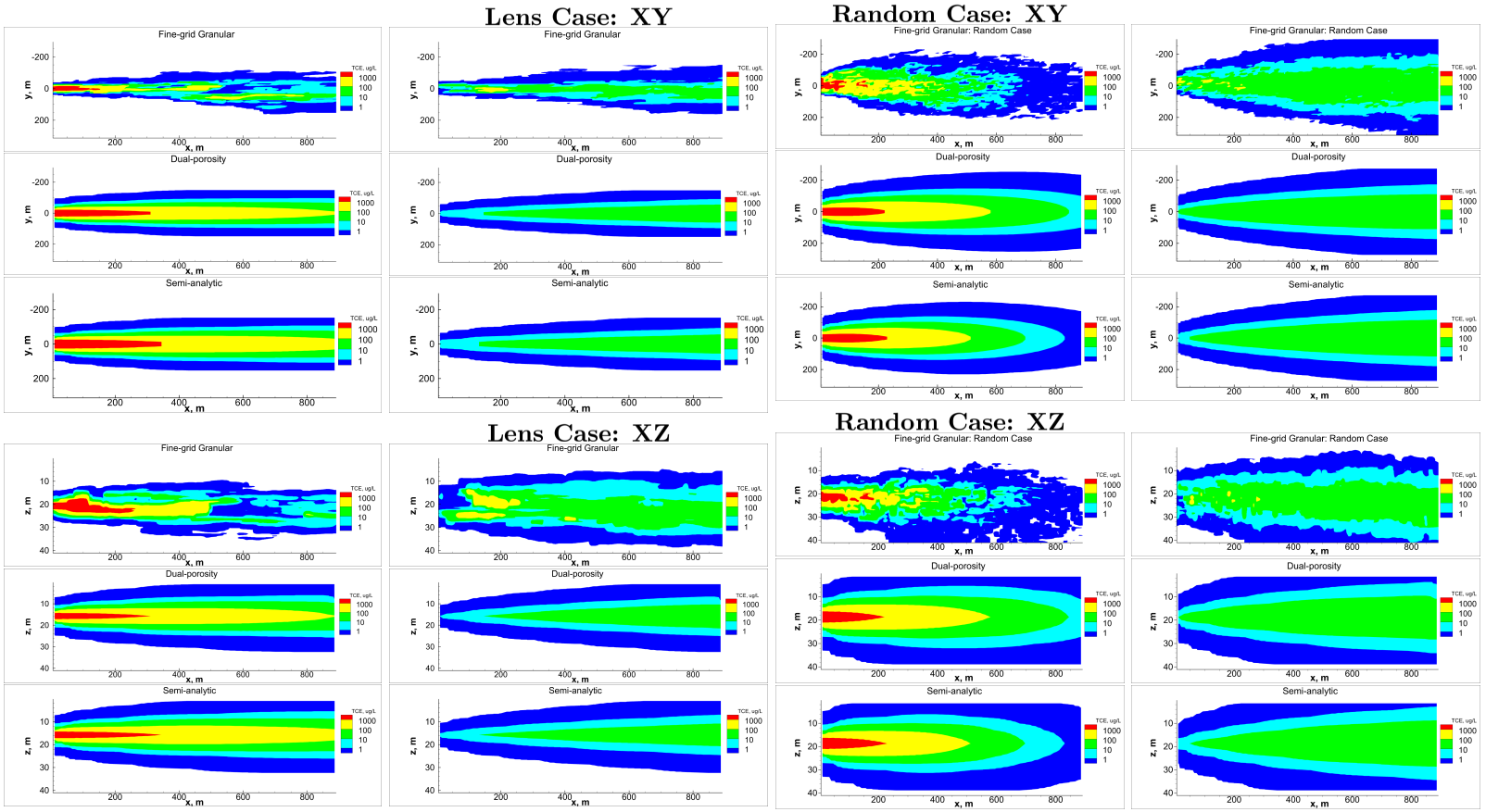

(a) Lens case: t = 30 years (b) Lens case: t = 130 years (c) Random case: t = 30 years (d) Random case: t = 130 years

Figure 4.4: Contours for two material distributions for the time windows of 30 and 130 years

4.4 Conclusion

Dual-porosity models were added to a previous study of matrix diffusion in 3-D numerical models of heterogeneous granular media (Muskus & Falta, 2018). Heterogeneity was simulated in two unique material distributions of sands and clays using TPROGS (Carle, 1999).

The dual-porosity was unable to simulate the fine-grid mass discharge at low NRMSEs without calibration. The behavior of the dual-porosity mass discharge varied over a range of the mass transfer coefficient, which was used as a calibrating parameter. At small values of the mass transfer coefficient, the dual-porosity model overpredicted the fine-grid model's mass discharge peak and at large values, the model overlooked matrix diffusion effects, generating mass discharge profiles more akin to those in an advection-dispersion dominant system. The calibrated dual-porosity concentration contours were similar to the semi-analytic model's, and they reasonably approximated the contours from the fine-grid models, which took tens of hours to simulate. Both EPM models were efficient in time, requiring minutes to complete a simulation.

The semi-analytic model simulated the fine-grid model's mass discharges within a small NRMSE using a diffusion length approximated via synthetic boreholes in the heterogeneous formations. With a single calibration, the semi-analytic model's NRMSEs were reduced to be much smaller than then dual-porosity model's errors. The semi-analytic model appears to be a more robust EPM model capable of approximating matrix diffusion in both fractured and heterogeneous media.

Chapter 5

Semi-analytic Model with Variable Diffusion Area

5.1 Introduction

The semi-analytic model was thoroughly tested in a system of parallel fractures, in discrete fracture networks, and in heterogeneous granular media, as shown in previous chapters of this dissertation. The results indicated that this model is capable of simulating matrix diffusion accurately in both fractured and granular media. A key matrix diffusion parameter in this model is the matrix diffusion area, which describes the interfacial area through which the contaminant mass diffuses. In its current implementation (Falta & Wang, 2017; Muskus & Falta, 2018) for embedded heterogeneities, the matrix diffusion area is a fixed parameter specified by the user based on an understanding of the matrix geometry. However, in an earlier adaptation of the semi-analytic model, Pruess and Wu (1993) considered the diffusion area to be a variable function. This inclusion by those researchers appears to be significant because it added a term in the governing function, that alters how the matrix diffusive flux is solved in the final transport solution.

In this chapter, the significance of the variable area function in the semi-analytic model is explored by first converting the existing semi-analytic model with a 1-D diffusion area to a 3-D semi-analytic model with a variable area function. Then, we compare the outputs between the 3-D semi-analytic model with variable diffusion area to the existing semi-analytic model in a series of

3-D matrix geometries. An analytical solution of diffusion in a 3-D matrix geometry (Crank, 1975) is used in the comparison as the benchmark. The objective is to quantify any gain in accuracy from the 3-D semi-analytic model as compared to the 1-D semi-analytic model. We add dual-porosity model simulation results to the comparisons to further evaluate how that model performs relative to the two semi-analytic models.

5.2 3-D Semi-analytic Model

5.2.1 Governing equation with a variable matrix area function

Figure 5.1 shows a conceptual model of a matrix gridblock where diffusion occurs from the surface of the block toward its center.

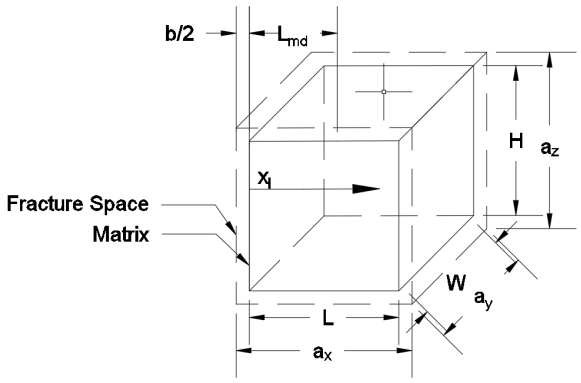

Figure 5.1: Conceptual model of a 3-D matrix block

Variables a_x, a_y, and a_z are the fracture spacing in three dimensions. Variables L, W, and H denote the length, width, and height of the 3-D matrix block. The fracture aperture is b, which is assumed to be uniform around the matrix block. From the fracture spacing and the aperture, the length, width, and height of the 3-D matrix block can be computed: $L = a_x - b$, $W = a_y - b$, and $H = a_z - b$.

Following Pruess and Wu (1993), the interfacial area through which the mass diffuses into the matrix block can be modeled as a varying function dependent on the distance into the matrix, x_l. Under this conceptual model, diffusion occurs over a range of x_l from 0 to L_{md} with L_{md} being the maximum diffusion distance from the fracture-matrix interface to the center of the matrix block. That definition is identical to how Muskus and Falta (2018) defined L_{md} in the 1-D semi-analytic model.

Pruess and Wu (1993) defines the variable area function as $A(x_l)$, which calculates the available interfacial area in an arbitrary matrix block of volume V_m:

$$A(x_l)dx_l = dV_m \tag{5.1}$$

For a 3-D matrix block of length L, width W, and height H, $A(x_l)$ is a polynomial:

$$\begin{aligned} A(x_l) &= 2(L-2x_l)(W-2x_l) + 2(W-2x_l)(H-2x_l) + 2(H-2x_l)(L-2x_l) \\ &= 24x_l^2 - 8x_l(L+W+H) + 2(LW+WH+HL) \end{aligned} \tag{5.2}$$

When the surface area of the matrix block is defined as $A_s = 2(LW + WH + HL)$ and the sum of the sides is defined as $S = L + W + H$, Equation 5.2 is simplified to:

$$A(x_l) = 24x_l^2 - 8Sx_l + A_s \tag{5.3}$$

At the interface when $x_l = 0$, Equation 5.3 returns the surface area of the 3-D matrix block, $A(0) = A_s$.

Equation 5.3 is verified by computing the ratio $A(x_l)/A(0)$ for a matrix cube of size L and compares it to Equation 13 in Pruess and Wu (1993). When the parallelepiped is a cube, the surface area becomes $A_s = 6L^2$, which is also the maximum diffusion area $A(0)$. Furthermore, the sum of sides becomes $S = 3L$ and by substituting S and A_s into Equation 5.3, the variable area function becomes $A(x_l) = 24x_l^2 - 24x_lL + 6L^2$, which simplifies to $A(x_l) = 6(L-2x_l)^2$. Taking the ratio $A(x_l)/A(0)$ now gives $A(x_l)/A(0) = (L-2x_l)^2/L^2$. Expanding the numerator and simplifying gives $A(x_l)/A(0) = (1-2x_l/L)^2$, which is identical to Equation 13 in Pruess and Wu (1993).

Including the variable matrix diffusion area in a mass balance of the matrix block results in the following governing equations with parent-daughter reactions:

$$\begin{aligned} R_{lm}\frac{\partial C_{lm}}{\partial t} &= \tau D\frac{\partial^2 C_{lm}}{\partial x_l^2} + \tau D\frac{\partial C_{lm}}{\partial x_l}\frac{1}{A(x_l)}\frac{\partial A(x_l)}{\partial x_l} + y_{m-1}\lambda_{lm-1}C_{lm-1} - \lambda_{lm}C_{lm} \\ &= \tau D\frac{\partial^2 C_{lm}}{\partial x_l^2} + \tau D\frac{\partial C_{lm}}{\partial x_l}\frac{\partial lnA(x_l)}{\partial x_l} + y_{m-1}\lambda_{lm-1}C_{lm-1} - \lambda_{lm}C_{lm} \qquad m > 1 \end{aligned} \tag{5.4}$$

$$R_{lm}\frac{\partial C_{lm}}{\partial t} = \tau D\frac{\partial^2 C_{lm}}{\partial x_l^2} + \tau D\frac{\partial C_{lm}}{\partial x_l}\frac{\partial lnA(x_l)}{\partial x_l} - \lambda_{lm}C_{lm} \qquad m = 1 \tag{5.5}$$

The variables are as defined in Muskus and Falta (2018).

5.2.2 Solving for p_m and q_m

The fitting function used in this 3-D formulation is unchanged from the function Muskus and Falta (2018) used, except x_l is now the diffusion distance in a 3-D system:

$$C_{lm}(x_l, t) = (C_m^{t+\Delta t} + p_m x_l + q_m x_l^2) e^{-x_l/d_m} \tag{5.6}$$

The penetration depth is identical to that which was previously defined by Muskus and Falta (2018) but now with an upper bound dependent on the decay rate:

$$d_m = min(\frac{\sqrt{\kappa_{lm} t}}{2}, \sqrt{\frac{\tau_l D}{\lambda_{lm}}}) \tag{5.7}$$

$$\kappa_{lm} = \frac{\tau_l D}{R_{lm}} \tag{5.8}$$

To solve for p_m and q_m in Equation 5.6, we need to set up a system of two equations, which can be obtained by applying two constraints to the diffusion mass discharge. The first constraint requires the governing equation (Equation 5.4) to be satisfied at the interface between the fracture and the matrix blocks:

$$R_{lm}\frac{\partial C_{lm}}{\partial t} = \tau_l D \frac{\partial^2 C_{lm}}{\partial x_l^2}|_{x_l=0} + \tau_l D \frac{\partial C_{lm}}{\partial x_l}|_{x_l=0} \frac{\partial lnA}{\partial x_l}|_{x_l=0} - \lambda_{lm} C_{lm}|_{x_l=0} + y_{lm-1}\lambda_{lm-1} C_{lm-1}|_{x_l=0} \tag{5.9}$$

A finite difference approximation is applied to the time derivative on the left hand side of Equation 5.9, whereas Equation 5.2 and Equation 5.6 are differentiated at the interface and substituted into the right hand side. After those operations, we have:

$$R_{lm}\frac{C_m^{t+\Delta t}-C_m^t}{\Delta t}=\tau D(\frac{C_m^{t+\Delta t}}{d_m^2}+2q_m-\frac{2p_m}{d_m})-\frac{8\tau_l DS}{A_s}(p_m-\frac{C_m^{t+\Delta t}}{d_m})-\lambda_{lm}C_m^{t+\Delta t}$$
$$+y_{lm-1}\lambda_{lm-1}C_{m-1}^{t+\Delta t} \tag{5.10}$$

The second constraint is the mass conservation of the diffusion mass in the matrix.

$$R_{lm}\frac{\partial}{\partial t}\int_0^{L_{md}}C_{lm}A(x_l)dx_l=-\tau_l DA(0)\frac{\partial C_{lm}}{\partial x_l}|_{x_l=0}+y_{lm-1}\lambda_{lm-1}\int_0^{L_{md}}C_{lm}A(x_l)dx_l$$
$$-\lambda_{lm}\int_0^{L_{md}}C_{lm}A(x_l)dx_l \tag{5.11}$$

Dividing both sides of Equation 5.11 by the area function evaluated at the interface, we have:

$$R_{lm}\frac{\partial}{\partial t}\int_0^{L_{md}}C_{lm}\frac{A(x_l)}{A(0)}dx_l=-\tau_l D\frac{\partial C_{lm}}{\partial x_l}|_{x_l=0}+y_{lm-1}\lambda_{lm-1}\int_0^{L_{md}}C_{lm}\frac{A(x_l)}{A(0)}dx_l$$
$$-\lambda_{lm}\int_0^{L_{md}}C_{lm}\frac{A(x_l)}{A(0)}dx_l \tag{5.12}$$

The concentration integrals in Equation 5.12 can now be evaluated separately:

$$\begin{aligned}I_m(t)&=\int_0^{L_{md}}C_{lm}\frac{A(x_l)}{A(0)}dx_l\\&=\int_0^{L_{md}}(C_m^{t+\Delta t}+p_mx_l+q_mx_l^2)(\frac{24}{A_s}x_l^2-\frac{8S}{A_s}x_l+1)e^{-x_l/dm}dx_l\end{aligned} \tag{5.13}$$

Grouping by the x-dependent terms $x_l^n e^{-x_l/dm}$ (n = 0, 1, 2, 3, 4) and performing the integrations, we have :

$$I(t)=\zeta_m\frac{24q_m}{A_s}+\epsilon_m(\frac{24p_m}{A_s}-\frac{8Sq_m}{A_s})+\beta_m(\frac{24C_m^{t+\Delta t}}{A_s}-\frac{8Sp_m}{A_s}+q_m)+\gamma_m(p_m-\frac{8SC_m^{t+\Delta t}}{A_s})$$
$$+\delta_m C_m^{t+\Delta t} \tag{5.14}$$

where, the coefficients δ_m, γ_m, β_m, ϵ_m, and ζ_m in Equation 5.14 are the weighting functions following

Pruess and Wu (1993). Those weighting functions are defined as:

$$\delta_m = d_m - d_m e^{-L_{md}/d_m} \tag{5.15}$$

$$\gamma_m = d_m^2 - e^{-L_{md}/d_m}(d_m^2 + d_m L_{md}) \tag{5.16}$$

$$\beta_m = 2d_m^3 - e^{-L_{md}/d_m}(2d_m^3 + 2d_m^2 L_{md} + d_m L_{md}^2) \tag{5.17}$$

$$\epsilon_m = 6d_m^4 - e^{-L_{md}/d}(6d_m^4 + 6d_m^3 L_{md} + 3d_m^2 L_{md}^2 + d_m L_{md}^3) \tag{5.18}$$

$$\zeta_m = 24d_m^5 - e^{-L_{md}/d_m}(24d_m^5 + 24d_m^4 L_{md} + 12d_m^3 L_{md}^2 + 4d_m^2 L_{md}^3 + d_m L_{md}^4) \tag{5.19}$$

The definitions of δ_m, γ_m, and β_m are identical to those of Muskus and Falta (2018). Grouping the terms on the right hand side of Equation 5.14 by $C_m^{t+\Delta t}$, q_m, and p_m gives an expression for the concentration integral that is similar to Muskus and Falta (2018)'s concentration integral:

$$I_m(t) = \delta'_m C_m^{t+\Delta t} + \beta'_m q_m + \gamma'_m p_m \tag{5.20}$$

where the coefficients for Equation 5.20 are defined as:

$$\delta'_m = \frac{24\beta_m}{A_s} - \frac{8S\gamma_m}{A_s} + \delta_m \tag{5.21}$$

$$\beta'_m = \frac{24\zeta_m}{A_s} - \frac{8S\epsilon_m}{A_s} + \beta_m \tag{5.22}$$

$$\gamma'_m = \frac{24\epsilon_m}{A_s} - \frac{8S\beta_m}{A_s} + \gamma_m \tag{5.23}$$

With the concentration integral defined, we can substitute it into Equation 5.12, along with the finite difference approximation of the time derivative on the left hand side and the first derivative of the fitting function evaluated at the interface:

$$\boxed{\begin{aligned} R_{lm}\frac{\delta'_m C_m^{t+\Delta t} + \beta'_m q_m + \gamma'_m p_m - I_m^t}{\Delta t} &= \tau_l D(\frac{C_m^{t+\Delta t}}{d_m} - p_m) + y_{lm-1}\lambda_{lm-1} I_{m-1}^{t+\Delta t} \\ &\quad -\lambda_{lm}(\delta'_m C_m^{t+\Delta t} + \beta'_m q_m + \gamma'_m p_m) \end{aligned}} \tag{5.24}$$

p_m and q_m can be solved sequentially via substitutions using Equation 5.10 and Equation

5.24, resulting in the explicit expressions below:

$$p_m = \frac{I_m^t + \frac{y_{lm-1}\lambda_{lm-1}I_{m-1}^{t+\Delta t}\Delta t}{R_{lm}} - E_m C_m^{t+\Delta t} - A_m(\frac{C_m^{t+\Delta t} - C_m^t}{2\kappa_{lm}\Delta t} - \frac{C_m^{t+\Delta t}}{2d_m^2} - \frac{y_{lm-1}\lambda_{lm-1}C_{m-1}^{t+\Delta t}}{2R_{lm}\kappa_{lm}} + \frac{\lambda_{lm}C_m^{t+\Delta t}}{2R_{lm}\kappa_{lm}} - \frac{4SC_m^{t+\Delta t}}{A_s d_m})}{A_m(\frac{1}{d_m} + \frac{4S}{A_s}) + B_m} \tag{5.25}$$

where:

$$A_m = \beta'_m + \frac{\lambda_{lm}\Delta t}{R_{lm}}\beta'_m \tag{5.26}$$

$$B_m = \gamma'_m + \kappa_{lm}\Delta t + \frac{\lambda_{lm}\Delta t}{R_{lm}}\gamma'_m \tag{5.27}$$

$$E_m = \gamma'_m - \frac{\kappa_{lm}\Delta t}{d_m} + \frac{\lambda_{lm}\Delta t}{R_{lm}}\delta'_m \tag{5.28}$$

$$q_m = \frac{\frac{(C_m^{t+\Delta t} - C_m^t)d_m^2}{\kappa_{lm}\Delta t} - C_m^{t+\Delta t} + 2d_m p_m - \frac{y_{lm-1}\lambda_{lm-1}C_{lm-1}^{t+\Delta t}d_m^2}{R_{lm}\kappa_{lm}} + \frac{\lambda_{lm}C_m^{t+\Delta t}d_m^2}{R_{lm}\kappa_{lm}} + \frac{8Sd_m}{A_s}(d_m p_m - C_m^{t+\Delta t})}{2d_m^2} \tag{5.29}$$

Following Muskus and Falta (2018), the expression for p_m is rewritten as a high-permeability concentration dependent term:

$$p_m = a_m C_m^{t+\Delta t} + b_m^{t+\Delta t} \tag{5.30}$$

with

$$a_m = \frac{-E_m - \frac{A_m}{2\kappa_{lm}\Delta t} + \frac{A_m}{2d_m^2} - \frac{A_m\lambda_{lm}}{2R_{lm}\kappa_{lm}} + \frac{4SA_m}{A_s d_m}}{A_m(\frac{1}{d_m} + \frac{4S}{A_s}) + B_m} \tag{5.31}$$

$$b_m = \frac{I_m^t + \frac{A_m C_m^t}{2\kappa_{lm}\Delta t} + \frac{A_m y_{lm-1}\lambda_{lm-1}C_{m-1}^{t+\Delta t}}{2R_{lm}\kappa_{lm}} + \frac{y_{lm-1}\lambda_{lm-1}I_{lm-1}^{t+\Delta t}\Delta t}{R_{lm}}}{A_m(\frac{1}{d_m} + \frac{4S}{A_s}) + B_m} \tag{5.32}$$

This allows for a convenient inclusion of the matrix diffusion mass discharge as a direct source/sink term in the usual advection-dispersion transport model of the high-permeability gridblocks. Follow-

ing (Muskus & Falta, 2018), the matrix mass discharge is rewritten below:

$$\begin{aligned} \dot{m_{lm}} &= \phi_l \tau_l D A(x_l) \frac{\partial C_{lm}}{\partial x_l}|_{x_l=0} \\ &= A_s \phi_l \tau_l D[(a_m - \frac{1}{d_m}) C_m^{t+\Delta t} + b_m^{t+\Delta t}] \end{aligned} \tag{5.33}$$

The matrix mass can be computed directly using the concentration integral with the variable area function:

$$\begin{aligned} m_{lm} &= \phi_l R_l \int_0^{L_{md}} C_l dV \\ &= \phi_l R_l \int_0^{L_{md}} C_l A(x_l) dx_l \\ &= A_s \phi_l R_l I(t) \end{aligned} \tag{5.34}$$

This expanded version of the semi-analytic model is currently programmed in MATLAB with the full source code included in Appendix A.

5.3 3-D Matrix Block Simulation Methods

The 3-D semi-analytic model with the variable diffusion area function was validated in a series of three matrix cubes and a matrix parallelepiped. It was compared to the 1-D semi-analytic model where a fixed diffusion area and an average diffusion length were calculated using the matrix block geometry. An analytical solution of diffusion in a generic matrix block by Crank (1975) was used as a benchmark. In the same comparisons, a dual-porosity model was evaluated as an alternative to the semi-analytic models.

5.3.1 Analytical solution

Assuming a boundary condition of a constant concentration in the fractures and a zero initial concentration everywhere in the matrix, Crank (1975) gave the analytical solution to the

governing diffusion equation of diffusion into a 3-D matrix block as shown in Figure 5.1.

$$C_{l,1} = C_0 - C_0 \frac{64}{\pi^3} \sum_{l=0}^{\infty} \sum_{m=0}^{\infty} \sum_{n=0}^{\infty} \frac{-1^{l+m+n}}{(2l+1)(2m+1)(2n+1)} * f(x,y,z)[\frac{k+\alpha * \exp[-t(k+\alpha)]}{k+\alpha}] \tag{5.35}$$

where,

$$f(x,y,z) = \cos\frac{(2l+1)\pi x}{2a} \cos\frac{(2m+1)\pi y}{2b} \cos\frac{(2n+1)\pi z}{2c}$$
$$\alpha = \frac{\pi^2 D \tau_l}{4R_l}[(\frac{2l+1}{a})^2 + (\frac{2m+1}{b})^2 + (\frac{2n+1}{c})^2]$$

The variable $C_{l,1}$ is the transient concentration in the matrix in a loading period whereas C_0 is the constant concentration in the fractures. The variable k is the constant decay rate. The variables a, b, and c are half of the length, width, and height of the matrix block. The variables D, τ_l, and R_l are the diffusion coefficient, the tortuosity and the retardation in the matrix respectively.

Equation 5.35 was integrated with respect to the block dimensions to obtain the transient matrix mass in the loading period:

$$\begin{aligned} M_{l,1} &= \phi_l R_l \int_{-a}^{a} \int_{-b}^{b} \int_{-c}^{c} C_{l,1} dx dy dz \\ &= C_0 \phi_l R_l abc[8 - (\frac{64}{\pi^3})^2 \sum_{l=0}^{\infty} \sum_{m=0}^{\infty} \sum_{n=0}^{\infty} \frac{1}{(2l+1)^2(2m+1)^2(2n+1)^2} . \frac{k+\alpha * \exp\{-t(k+\alpha)\}}{k+\alpha}] \end{aligned} \tag{5.36}$$

Crank (1975) also solved for the matrix mass discharge in the loading period analytically:

$$\dot{m_{l,1}} = (\frac{64}{\pi^3})^2 \phi_l R_l C_0 abc \sum_{l=0}^{\infty} \sum_{m=0}^{\infty} \sum_{n=0}^{\infty} \frac{\alpha}{(2l+1)^2(2m+1)^2(2n+1)^2} . \frac{k+\alpha * \exp\{-t(k+\alpha)\}}{k+\alpha} \tag{5.37}$$

For the unloading period, superposition in time was applied on the loading concentration in Equation 5.35 first to obtain the unloading transient concentration. Then, the unloading analytical

solution was integrated over the matrix volume to obtain the matrix mass in the unloading period:

$$M_{l,2} = (\frac{64}{\pi^3})^2 C_0 \phi_l R_l abc[\sum_{l=0}^{\infty}\sum_{m=0}^{\infty}\sum_{n=0}^{\infty} \frac{k+\alpha*\exp\{-(t-t_1)(k+\alpha)\}}{(k+\alpha)(2l+1)^2(2m+1)^2(2n+1)^2} - \sum_{l=0}^{\infty}\sum_{m=0}^{\infty}\sum_{n=0}^{\infty} \frac{k+\alpha*\exp\{-t(k+\alpha)\}}{(k+\alpha)(2l+1)^2(2m+1)^2(2n+1)^2}] \tag{5.38}$$

For the unloading matrix mass discharge, superposition was applied in the same manner:

$$\begin{aligned} \dot{m_{l,2}} &= \dot{m_{l,1}}(t) - \dot{m_{l,1}}(t-t_1) \\ &= (\frac{64}{\pi^3})^2 C_0 \phi_l R_l abc\{\sum_{l=0}^{\infty}\sum_{m=0}^{\infty}\sum_{n=0}^{\infty} \frac{\alpha[k+\alpha*\exp\{-t(k+\alpha)\}]}{(k+\alpha)(2l+1)^2(2m+1)^2(2n+1)^2} \\ &\quad - \sum_{l=0}^{\infty}\sum_{m=0}^{\infty}\sum_{n=0}^{\infty} \frac{\alpha[k+\alpha*\exp\{-(t-t_1)(k+\alpha)\}]}{(k+\alpha)(2l+1)^2(2m+1)^2(2n+1)^2}\} \end{aligned} \tag{5.39}$$

The analytical solution of the matrix mass and discharge in equations 5.36 to 5.39 were programmed in MATLAB. Vectorized programming was utilized to avoid usage of `for` loops, which boosted efficiency. A copy of the code is included in Appendix B.

The programmed analytical solution was applied in a series of four geometries: a 0.2-m cube, a 2-m cube, a 5-m cube, and a 10x10x1 m^3 parallelepiped. The loading period was set for 50 years, which was followed by an unloading period of the same length for a total simulation time of 100 years. An arbitrary source concentration C_0 was chosen to be 0.1 g/L. Two retardation cases were evaluated for each geometry: one without retardation and one with a R_l of 3. A no decay case was considered first and then a decay of 2-year half-life was implemented. When retardation was present, decay was not considered and vice versa. Other parameters for the simulations are listed in Table 5.1.

5.3.2 Dual-porosity model

Pham and Falta (2022) solved the matrix equation of the dual-porosity model in Section 2.2.1 for a 1-D matrix block surrounded by fractures using the same boundary and initial conditions as the 3-D matrix block analytical solution:

Parameter	Value
Aperture, μm	100
D, m^2/yr	0.0316
C_0, g/L	0.1
ϕ_l	0.1
τ_l	0.1
R_l	1 or 3
$t_{1/2}$, yrs	2 or no decay
Loading, yrs	50[a]
Unloading, yrs	100

[a] 5 years for 0.2-m case

Table 5.1: Parameters for 3-D matrix block simulations

$$C_{l,1} = \frac{\beta C_0}{\beta + \lambda_l \phi_l (1 - V_f)} (1 - e^{-\frac{\beta + \lambda_l \phi_l (1 - V_f)}{(1 - V_f)\phi_l R_l} t}) \tag{5.40}$$

where β is the dual-porosity mass transfer coefficient and λ_l is the first-order decay rate in the matrix, with other variables as defined previously. We used this solution to create dual-porosity simulations for comparisons in the series of 3-D matrix blocks.

Applying superposition in time to Equation 5.40 gives the dual-porosity matrix concentration in the unloading period:

$$C_{l,2} = \frac{\beta C_0}{\beta + \lambda_l \phi_l (1 - V_f)} [\exp\{-\frac{\beta + \lambda_l \phi_l (1 - V_f)}{(1 - V_f)\phi_l R_l} (t - t_1)\} - \exp\{-\frac{\beta + \lambda_l \phi_l (1 - V_f)}{(1 - V_f)\phi_l R_l} t\}] \tag{5.41}$$

The loading and unloading matrix mass discharges in a 3-D parallelepiped can be computed using the concentration gradient between the fractures and the matrix:

$$\dot{m_{l,1}} = \beta V (C_0 - C_{l,1}) \tag{5.42}$$

$$\dot{m_{l,2}} = \beta V (-C_{l,2}) \tag{5.43}$$

Multiplying the dual-porosity matrix concentrations by the volume, the material porosity, and the retardation factor of the matrix gives the matrix masses for both periods:

$$M_{l,1} = R_l \phi_l (1 - V_f) V C_{l,1} \tag{5.44}$$

$$M_{l,2} = R_l \phi_l (1 - V_f) V C_{l,2} \tag{5.45}$$

Equations 5.42 to 5.45 were applied in the same 3-D parallelepiped geometries using parameters in Table 5.1. The dual-porosity model requires input of the mass transfer coefficient to simulate the matrix mass transfer between the block and the surrounding fractures. We computed an initial coefficient for each geometry case using:

$$\beta = \frac{(1 - V_f) \phi_l \tau_l D}{L_{md}^2} \tag{5.46}$$

where L_{md} is the average matrix diffusion length in the 1-D semi-analytic model. We describe the procedure to compute this average length in Section 5.3.3.

The resulting matrix mass discharges and masses were compared to the analytical solution and the 1-D and 3-D semi-analytic models.

5.3.3 Semi-analytic models

1-D and 3-D semi-analytic models were run for the series of 3-D matrix blocks. Both models were implemented in a single equivalent porous media (EPM) gridblock of a length a_x, a width a_y, and a height a_z as shown in Figure 5.1. The EPM gridblock dimension was computed by adding the length L, width W, and height H of the matrix block to a fracture aperture, which was set to 100 μm for all 3-D matrix block cases. The semi-analytic models use the same parameters as shown in Table 5.1.

To simulate a constant fracture concentration, we set the Darcy velocity in the semi-analytic models to a large value. The matrix mass discharge was calculated by subtracting the fracture mass discharge from the source mass discharge. We calculated the source mass discharge by multiplying the Darcy velocity by the source concentration and the gridblock cross-sectional area. The matrix mass was computed by multiplying the semi-analytic concentration integral at each timestep by the diffusion area, the matrix porosity, and the matrix retardation factor.

The volume fraction of the fractures is a diffusion modeling parameter in both semi-analytic models. It was computed using the ratio of the matrix volume to the total volume:

$$V_f = 1 - \frac{V_l}{V} \tag{5.47}$$

where V_l is the matrix volume. The matrix volume is straightforward for a cube (L^3) and a parallelepiped ($L * W * H$). The same volume fraction of the fractures is used in the 1-D and 3-D semi-analytic models.

For the diffusion area, the 3-D semi-analytic model utilizes a polynomial area function which varies according to a diffusion length (Equation 5.3). It internally computes a maximum diffusion length based on the geometry of the 3-D matrix block. For these simulations, that length can either be half the side of a cube or the average of half the length, width, and height of a parallelepiped.

In the 1-D semi-analytic model, the matrix diffusion area A_{md} is a fixed value, which equals the 3-D semi-analytic area function evaluated at the fractures-matrix interface when the matrix diffusion length is zero. Given the volume of the EPM gridblock, the volume fraction of the fractures, and the fixed diffusion area, the 1-D model's average diffusion length L_{md} is computed directly using the matrix volume balance: $(1 - V_f)V = A_{md}L_{md}$.

The 1-D semi-analytic model was run using a Fortran executable whereas the MATLAB code (Appendix A) was used to implement the 3-D semi-analytic model.

Root mean square errors (RMSEs) were computed for each semi-analytic and dual-porosity simulation using the analytical solution as the benchmark. Those errors were normalized to the maximum analytical solution mass or mass discharge to calculate the normalized root mean square errors (NRMSEs). The procedure to compute the RMSEs was the same as implemented in previous chapters.

5.4 3-D Matrix Block Results

5.4.1 Dual-porosity and analytical solution comparisons

Figure 5.2 shows the dual-porosity mass discharge and its calibrations (solid lines) in comparison to the analytical mass discharge (black circle). As the volume of the 3-D matrix block

increased, the magnitude of the mass discharge increased from a maximum absolute value of just below $1 * 10^{-4}$ kg/yr in the 0.2-m cube to 0.05 kg/yr in the parallelepiped. While the scale of the mass discharge varied with the size of the matrix block, the shape of the discharge curve remained the same. In the loading period, the mass discharge curve started at a high value and then dropped gradually over time. The slope of the mass discharge curve reduced to zero when equilibrium was reached between the concentration in the fractures and in the matrix. The mass discharge curve reversed in the unloading period when the source concentration was removed, and mass discharge diffused from the matrix out into the fractures.

The dual-porosity model did not require calibration in the 0.2-m cube case but calibration was necessary for other cases. The dual-porosity mass discharge curve with the lowest NRMSE is plotted in blue line (Figure 5.2). The dual-porosity model has been shown in previous chapters to be accurate when the fracture spacing is small. The model relies on a linear driving force assumption to simulate the concentration gradient between the fractures and the matrix. Such assumption works well when the fractures are close together but not as well when they are far apart. As the matrix block became larger, the dual-porosity NRMSE were as high as 16% (blue line in Figure 5.2c). The dual-porosity model overlapped with the analytical solution more at late times. This is consistent with our understanding of the dual-porosity model's limitation in simulating matrix diffusion.

Dual-porosity mass discharges with large errors leads to matrix mass approximations with large errors for the dual-porosity as shown in Figure 5.3. The dual-porosity mass curve had a 1.7% NRMSE in the 0.2-m cube case but that error increased tenfold as the matrix block increased in size.

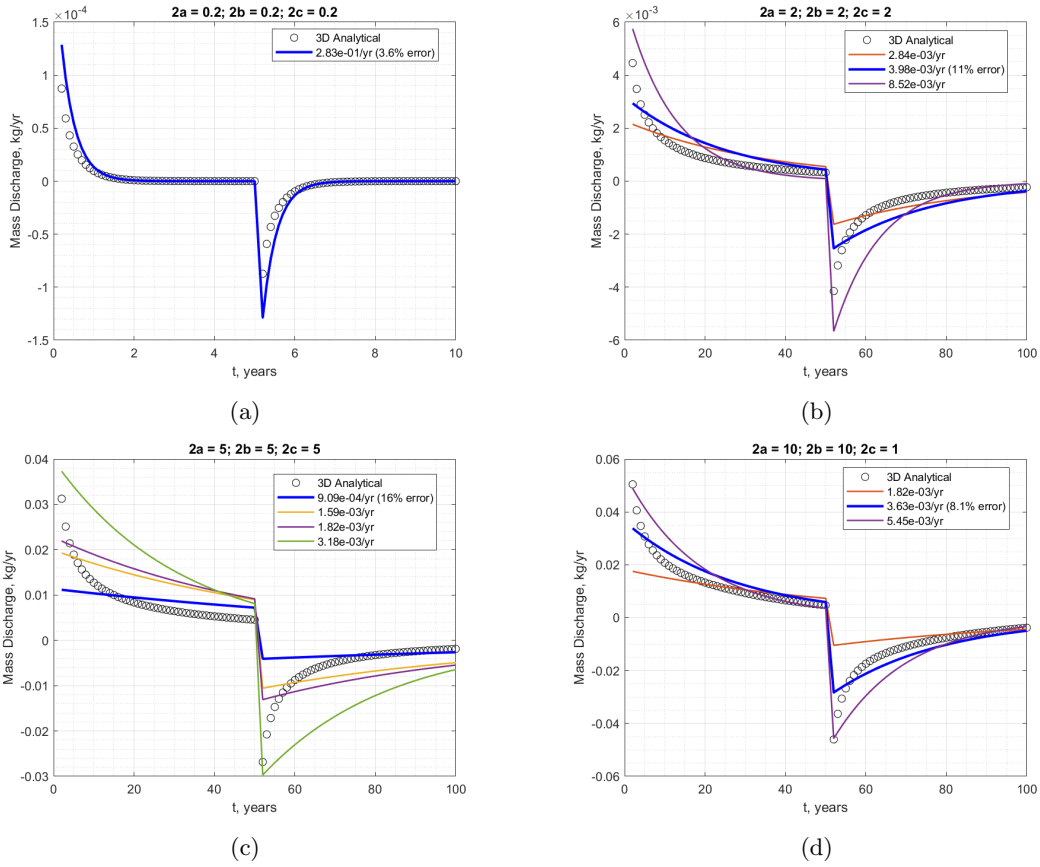

Figure 5.2: Comparison of dual-porosity mass discharge to analytical mass discharge for: a) 0.2-m cube, b) 2-m cube, c) 5-m cube, and d) 10x10x1 parallelepiped.

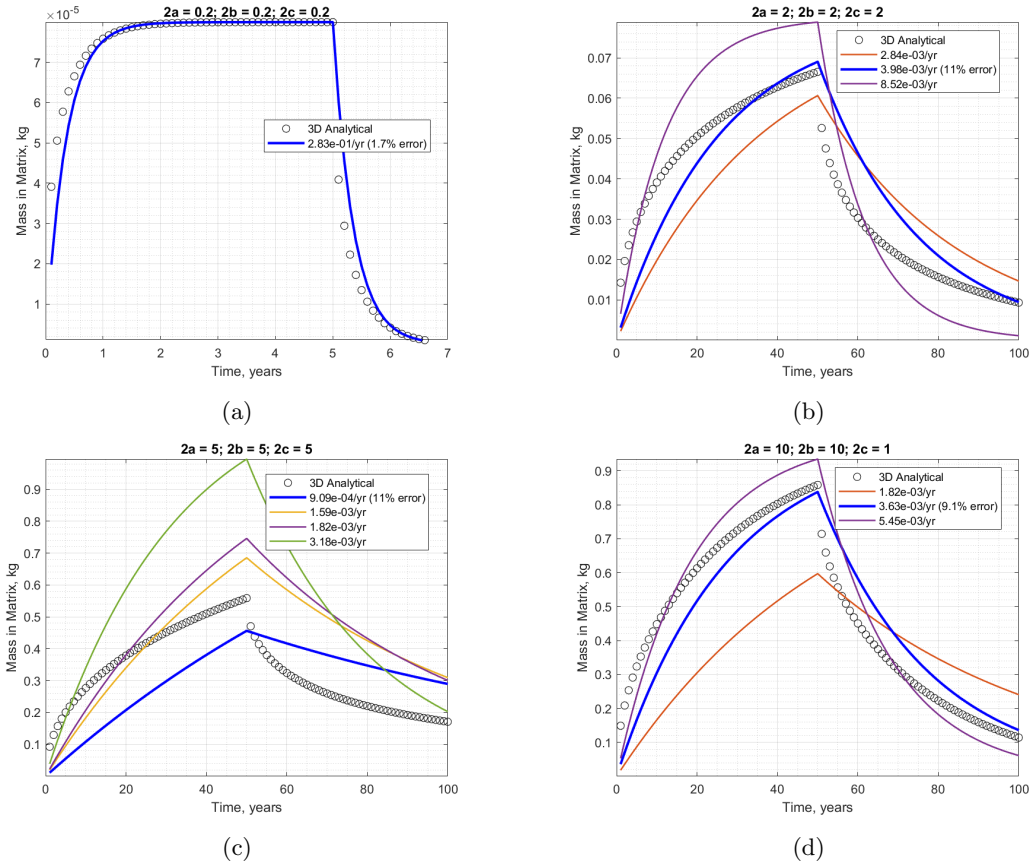

Figure 5.3: Comparison of dual-porosity matrix mass to analytical matrix mass for: a) 0.2-m cube, b) 2-m cube, c) 5-m cube, and d) 10x10x1 parallelepiped.

5.4.2 Comparisons with semi-analytic models

We retained the calibrated dual-porosity mass discharge with the lowest NRMSEs and added the 1-D and 3-D semi-analytic mass discharges for comparison in Figure 5.4. The 3-D semi-analytic mass discharge in green lines matched the analytical mass discharge at less than 6.2% NRMSE. The 3-D semi-analytic mass discharge curves (green line in Figure 5.4) were essentially identical to the analytical solution (circle in Figure 5.4) in the loading period. In the unloading period, the 3-D semi-analytic model deviated a bit from the analytical solution but still very close, especially at late times.

The 1-D semi-analytic model (purple line in Figure 5.4) did not match the analytical solution as well as the 3-D model but it still showed good correspondence with the analytical solution, especially in comparison to the dual-porosity model. It replicated the non-linear curvature of the analytical solution well as the matrix block increased in size while the dual-porosity became more linear and less accurate.

The 3-D semi-analytic model gained accuracy because it modeled the matrix area function using a polynomial which adjusts with the changes in the diffusion distance and the fracture-matrix concentration gradient over time. A different polynomial area function is required if the matrix geometry changes from being a cube or a parallelepiped to for example, a sphere.

While the 1-D semi-analytic model assumes a fixed matrix diffusion area and a conservative diffusion length, its error difference in comparison to the 3-D model was only about 5% at worst. The 1-D semi-analytic model has been shown to give adequate results in complex settings such as 3-D discrete fracture networks and heterogeneous granular media.

In Figure 5.5, we show the performance of the semi-analytic models in comparison to the dual-porosity model and the analytical solution in the same geometries with a matrix retardation of 3. The addition of adsorption raised the magnitude of the mass discharge curves. The three models performed similarly when the matrix block was small. As the size increased, the dual-porosity became less accurate than the semi-analytic models. The presence of sorption reduced the magnitude of the best-fit mass transfer coefficient in all geometries.

The 3-D semi-analytic model adjusted to sorption effects and maintained good accuracy with the analytical solution, indicating that the method was derived and programmed correctly for a non-unity retardation factor. The error difference between the 1-D and the 3-D semi-analytic

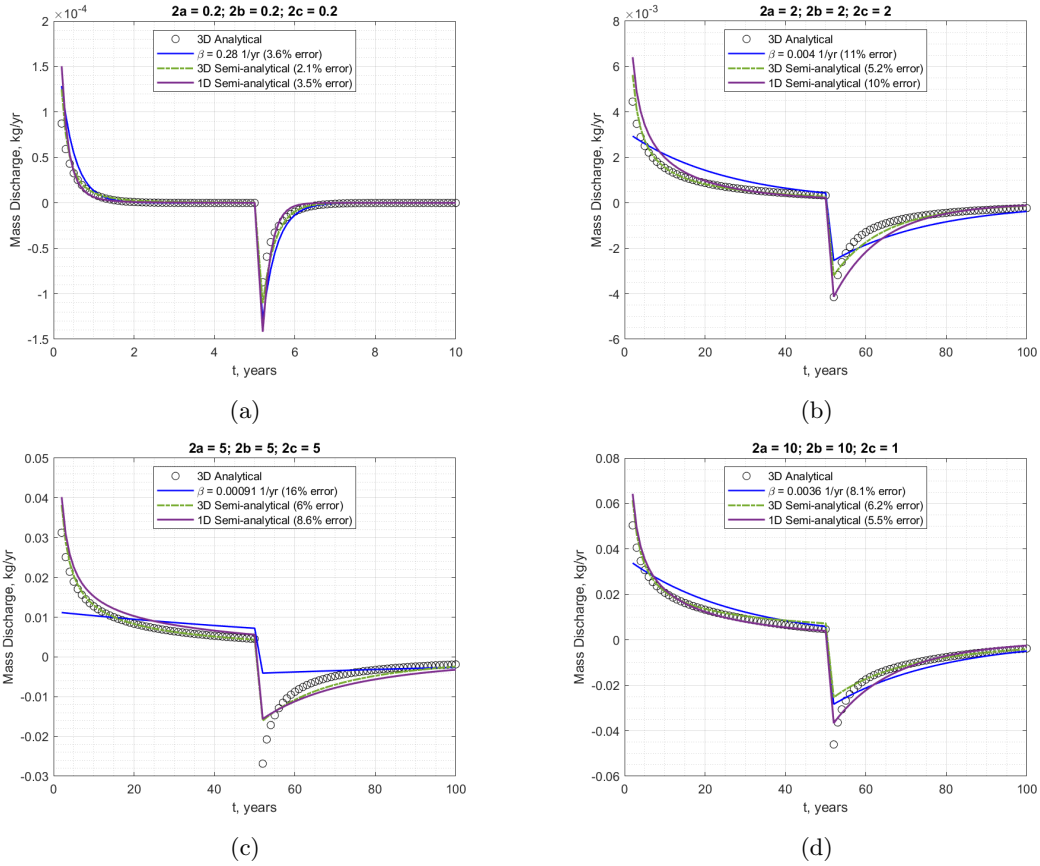

Figure 5.4: Comparison of semi-analytic matrix mass discharges to dual-porosity and analytical matrix masses for: a) 0.2-m cube, b) 2-m cube, c) 5-m cube, and d) 10x10x1 parallelepiped.

models was consistent with the case when sorption was not considered.

In simulations of matrix diffusion in the same geometries with a 2-yr half-life decay in the matrix, we observed the 3-D semi-analytic model adjusted well to the presence of decay as shown in Figure 5.6. However, the fast decay rate limited the penetration distance of the mass to a small length of 0.1 m. This short distance in effect normalized diffusive transport in all four blocks to one small cube case, which gave a false illusion that the dual-porosity performed well in all cases.

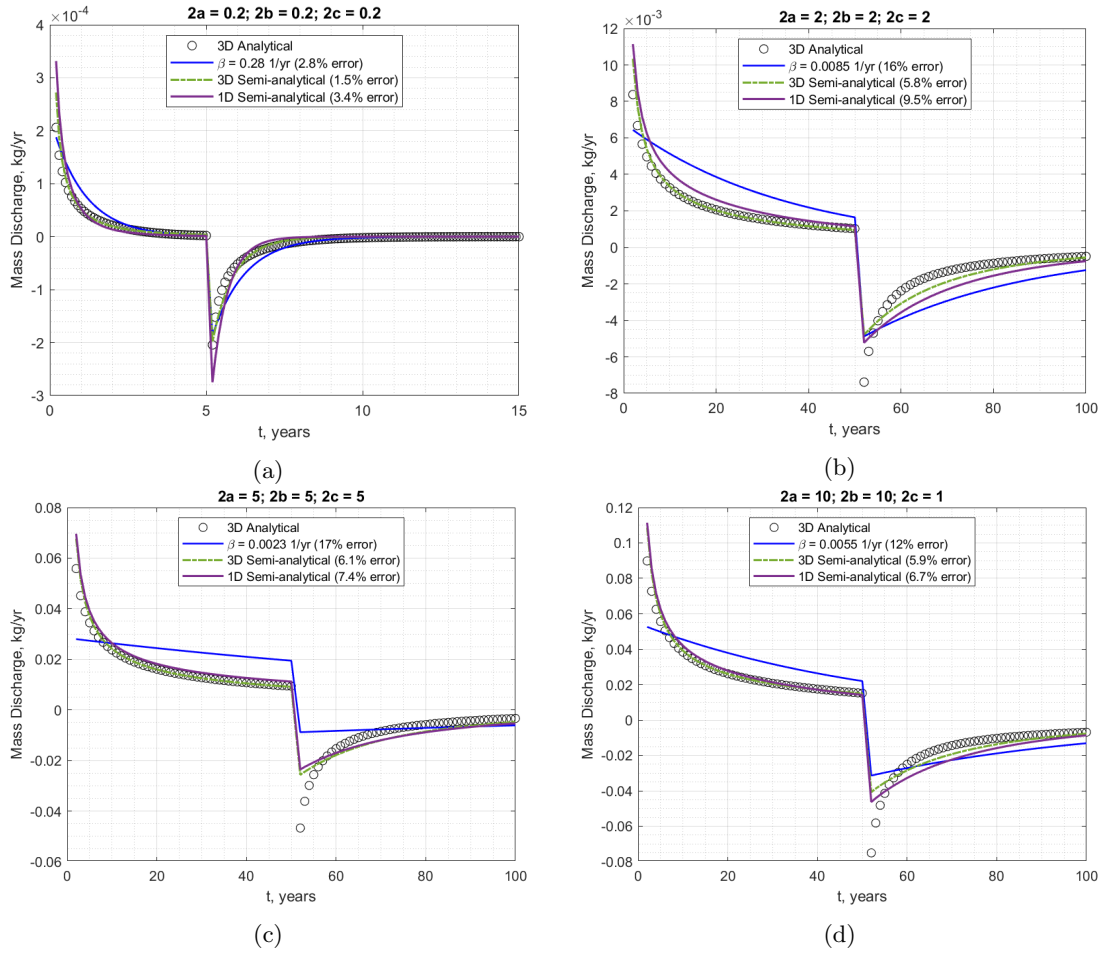

Figure 5.5: Comparison of semi-analytic matrix mass discharges with retardation factor of 3 to calibrated dual-porosity and analytical matrix discharges for: a) 0.2-m cube, b) 2-m cube, c) 5-m cube, and d) 10x10x1 parallelepiped.

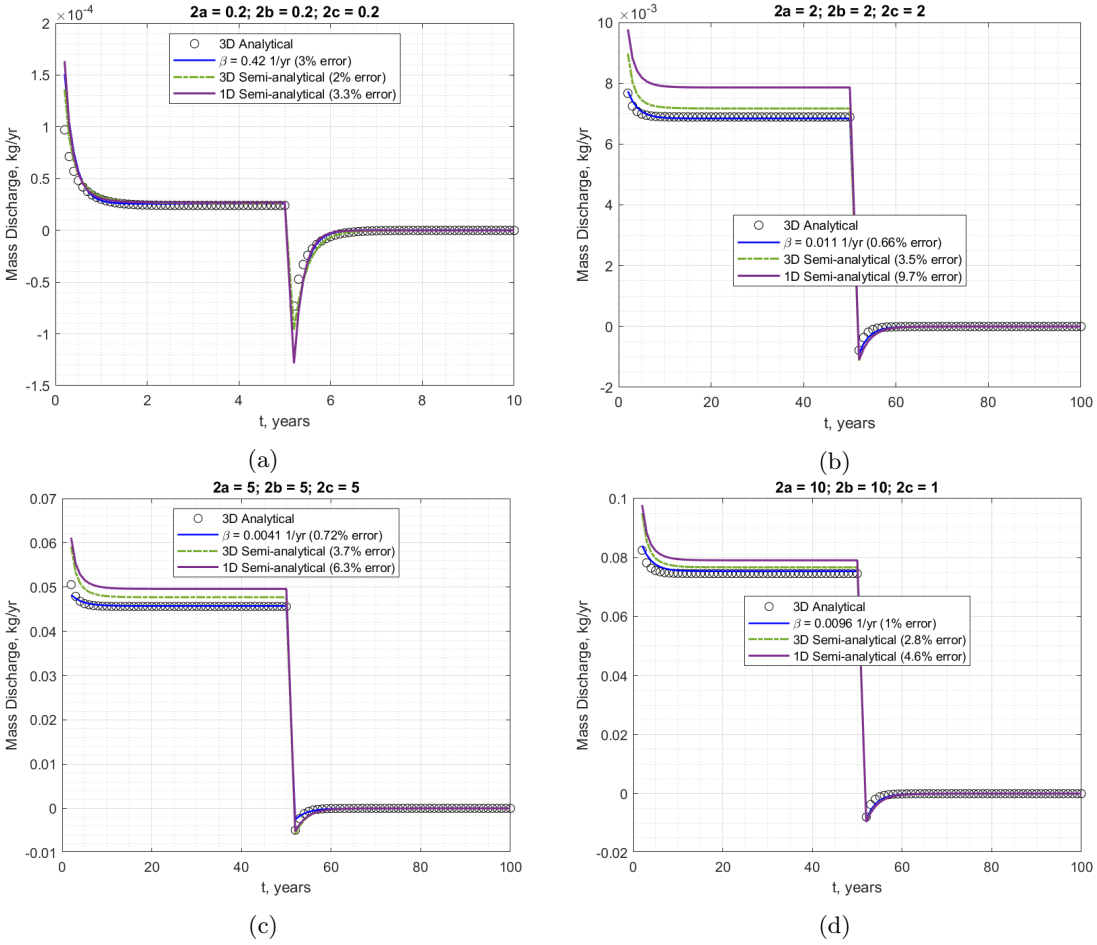

Figure 5.6: Comparison of semi-analytic matrix mass discharges with 2-yr half-life decay rate to calibrated dual-porosity and analytical matrix discharges for: a) 0.2-m cube, b) 2-m cube, c) 5-m cube, and d) 10x10x1 parallelepiped.

5.5 Conclusion

The semi-analytic model was expanded to include a variable diffusion area function in a 3-D semi-analytic model. The area function is currently applicable to only a matrix block of finite length, width, and height. When the variable area function is evaluated at the interface, the function returns the surface area of the matrix, which is also the fixed matrix diffusion area in the 1-D semi-analytic model.

The expansion was tested in a series of three matrix cubes and a parallelepiped with an analytical solution (Crank, 1975) used as a benchmark. When comparing the mass discharges and the masses from the two semi-analytic models, we found the two models to differ by less than 5%. For that gain in a matrix of a different geometry, a different area function needs to be programmed in the 3-D semi-analytic model. While the 1-D semi-analytic model uses a fixed diffusion area and an average diffusion length based on a matrix volume balance, it matched at low NRMSEs to the analytical solution, especially when comparing to the dual-porosity model.

The dual-porosity mass and mass discharge have higher NRMSEs as those of the semi-analytic models (maximum NRMSE at 17% in the 5-m cube case with retardation). As observed in previous chapters, the dual-porosity model only performed well when the fracture spacing and the matrix block are small. When the spacing and the block size increase, the model's assumption that the matrix diffusive mass flux obeys a linear force model is no longer valid, and it causes the dual-porosity model to give high errors.

Chapter 6

General Conclusions

The semi-analytic trial function model was tested in a system of parallel fractures, in 2-D/3-D discrete fracture networks (DFNs), and in 3-D heterogeneous porous media. The model maintained consistently low errors when compared with the analytical solution for transport in parallel fractures (Sudicky & Frind, 1982) over a range of fracture spacing. The errors remained low when retardation and decay were considered. The efficiency of the semi-analytic model was salient in the cases of discrete fracture networks where it gave results in a few minutes while the fine-grid DFN models took hours to complete. The model was within 3% error when simulating matrix diffusion in a 2-D DFN and within 6% error in several cases of 3-D DFNs. When considering the plume movement in DFNs, the semi-analytic model predicted within a few meters of the longitudinal extents and the concentration contours of the fine-grid DFN model. In two material distributions of a heterogeneous media, the semi-analytic model performed similarly well.

A notable strength of the semi-analytic model is that its matrix diffusion modeling parameters are directly computed in fractured and porous media using either the fracture properties or heterogeneity observations from subsurface core/boreholes. An effort to improve the semi-analytic model by including a variable diffusion area yielded about a 5% gain in accuracy.

In contrast with the semi-analytic model, the dual-porosity model appeared to be a less robust equivalent porous media approach. It relied on a first-order mass transfer coefficient, which can be initially estimated as the inverse of the characteristic diffusion time. The dual-porosity performed well at first in cases when the fracture spacing was small. However even with calibration, in cases when the fracture spacing was large, the dual-porosity model had higher errors than the

semi-analytic model and was unable to match analytical solutions as well as fine-grid results.

Appendices

Appendix A

Expanded semi-analytic code

```
%Semi-ana with 3D grid, 3D dispersion, decay, no daughter production
    ,
%step function for source behavior, embedded md, no zone remediation
%v201: added 3d full formulation
%v202: added mass_rc and dmdt_rc exports. Separated quick plotting.
%v203: revised importing of mass3d, dmdt3d as matrix, not cells
%v204: in quick plots, normalized NRMSE of mass by mass in matrix
%v205: changed Lmd to average of all sides, instead of min of all
    sides
%v206: add 1D SA results for comparison, added error calcs for 1d
    data,
%v207: added exports of 1d data
clearvars;
tic;
%3D fracture spacing and run number
LWH = [2 2 2]; %3d matrix block dimensions
rcruns = 70202;
% pore vol, frac aperture, frac spa: m/yr, m, m
% FOR PARALLEL FRAC CASE only
```

```
%Vp = 100; b = 1e-4;
%a = .5; %1D fracture spacing
% FOR OTHER CASES
Vd = 500; %specify for porous media and simple 3d parallel frac
%Amd = 3.223477258347244e+02; %for porous media case
%Vf = 0.288; Lmd = 1.5;  %for porous media case
% Gridblock properties
dx = 2.0001; dy = 2.0001; dz = 2.0001;
nx = 1; %+1 for source cell at x=0
ny = 1; nz = 1; %ny is y+ only!!
% Porosities
phi_f = 1; phi_l = 0.1;
% alphax,y,z for dispersion
alx = 0; aly = 0; alz = 0;
% Transport properties
czero = 0.1; tzeromass = 10000; %kg/m3 or g/L, kg
% Source location
lysrc = 1; lzsrcmin = 1; lzsrcmax = 1;
% Reaction and retardation properties; years, unitless
thalf_f = 1e6; thalf_l = 1e6;
Rl = 1; R = 1;
% Diffusion properties: unitless, m2/yr
tau_f = .1; tau_l = 0.1;
D = 0.0315576; %m^2/yr
% Time properties
dt = 1; t1 = 50; nt = 100; %CHANGE
eps = 1e-4; %Falta's numerical zero for use when t1=t2
% Gauss Seidel tolerance
tol = 1e-4; maxit = 500;
%Import RC for troubleshooting only
```

```
%conc_rc = importRCMD('REMChlor-MD_3dfrc70701.out');
%Import 3D matrrix mass and mass discharge
mass3d = load(...
['mass3d_thalf=' num2str(thalf_l) 'yrs_Rl=' num2str(Rl)...
'_run' num2str(rcruns) '.txt']);
dmdt3d = load(...
['dmdt3d_thalf=' num2str(thalf_l) 'yrs_Rl=' num2str(Rl)...
'_run' num2str(rcruns) '.txt']);
raw_mass_rc = imp_rcmd_mass(['plume_mass_3dfrc' num2str(rcruns) '.
    out']);
raw_dmdt_rc = imp_rcmd_mDschrg(['discharge_3dfrc' num2str(rcruns) '.
    out']);
%%%%%%%%%%%%%%%%%%%%%%%%%%%%%%%%%%%%%%%%%%%%%%%%%%%%%%%%%%%%%%%%%%%
% Compute SEMI-ANALYTICAL SOLUTION
for i = 1:size(LWH,1)
L(i) = LWH(i,1); W(i) = LWH(i,2); H(i) = LWH(i,3);
end
% Compute distance arrays
% Add extra for src cell and ci+1jk, cij+1k, cijk+1 in dispersion
    terms
x = 0:dx:dx*nx; y = dy:dy:dy*ny; z = dz:dz:dz*nz;
%tabtxyz = mesh
% Compute SA matrix diff paras (embedded case)
%Vf = b/a; Lmd = (a-b)/2; %for parallel frac case only
V = dx.*dy.*dz; Vf = 1 - (L*W*H)/V; volh = V*Vf;
Vl = L*W*H; %volume of matrix
%Amd = (1-Vf)*V/Lmd;  %for parallel frac case only
As = 2*(L*W + W*H + H*L); S = L + W + H;
%Lmd = (1 - Vf)*V/Amd; %SAA
Lmd = mean([L/2 W/2 H/2]); %full 3d formulation Lmd
```

```
% Compute Darcy velocity
%Vd = phi_f*Vf*Vp; %for 1d parallel frac case only
% Time properties
t2 = t1+dt; %assume t1<t<t2 does not exist
t_off_end = dt*nt;
t_on = dt:dt:t1; t_off = t_on(end)+dt:dt:t_off_end;
t = [eps t_on t_off]; %tplotrc = tplot*dt*npt;
% Prepare table to report concentration
%[T,X,Y,Z] = ndgrid(t,x,y,z);
[Z,Y,X,T] = ndgrid(z,y,x(2:end),t(2:end)); %include nx+1, nt+1
% Subtract half a gblock size and tabulate
tabxyz = [X(:)-(dx/2) Y(:)-(dy/2) Z(:)-(dz/2)];
tabtxyz = [T(:) tabxyz];
% Diffusion and reaction Properties
%tcdiff = max(axyz)^2/D; tcadv = max(axyz)/Vd;
kappa = tau_l*D/Rl;
lambda_l = log(2)/thalf_l; lambda = log(2)/thalf_f;
% Penetration depth
d = min(sqrt(tau_l*D/lambda_l),sqrt(kappa*t)/2); %d for all times
%Da2 = tcdiff/(1/lambda); Da1 = tcadv/(1/lambda);
%Compute XS area for dispersion terms
ayz = dz*dy*Vf; %HIGH K area, need to multiply mass and discharge by
    2
axz = dz*dx*Vf; axy = dx*dy*Vf;
%Compute dispersivities
Dy = aly*Vd/(Vf*phi_f) + tau_f*D;
Dz = alz*Vd/(Vf*phi_f) + tau_f*D;
Dx = (alx - dx/2)*Vd/(Vf*phi_f); %falta did not include D* in Dx
   calc
%Dx applies only when greater than num dispersion
```

```
if Dx < 0; Dx = 0;end
% Zero out Dy and Dz for single-block case
if ny == 1; Dy = 0; end; if nz == 1; Dz = 0; end
% Create source step function behavior
%csource = [czero*ones(1,length(t_on)) 0*ones(1,length(t_off))];
% paras for integral for all times
delt = d - d.*exp(-Lmd./d);
gam = d.^2 - (d*Lmd + d.^2).*exp(-Lmd./d);
beta = 2*d.^3 - (Lmd^2*d + 2*Lmd*d.^2 + 2*d.^3).*exp(-Lmd./d);
epsi = 6*d.^4 - (6*d.^4 + 6*Lmd*d.^3 + 3*Lmd^2*d.^2 + Lmd^3*d).*...
exp(-Lmd./d);
zeta = 24*d.^5 - (24*d.^5 + 24*Lmd*d.^4 + 12*Lmd^2*d.^3 + ...
4*Lmd^3*d.^2 + Lmd^4*d).*exp(-Lmd./d);
% Compute 3d formula terms
deltpr = (24/As)*beta - (8*S/As)*gam + delt;
betapr = (24/As)*zeta - (8*S/As)*epsi + beta;
gampr = (24/As)*epsi - (8*S/As)*beta + gam;
% Compute paras for p and q for all times
A = betapr + (lambda_l*dt/Rl)*betapr; %this is A
B = gampr + kappa*dt + (lambda_l*dt/Rl)*gampr; %this is B
E = deltpr - kappa*dt./d + (lambda_l*dt/Rl)*deltpr; %this is E
% Compute a for p calc, all times, all times
% no parent-daughter
atop = -E - A/(2*kappa*dt) + A./(2*d.^2) - A*lambda_l/(2*Rl*kappa) +
    ...
(4*S*A)./(As*d);
abot = A./d + (4*S/As)*A + B; aa2 = atop./abot;
% Compute deno for b in p = aC + b, all times
bbot = A./d + (4*S/As)*A + B;
% Compute denom for Ax=b to solve for Cnew all times, not space
```

```
    variable
deno2 = (As*phi_l*tau_l*D./d - As*phi_l*tau_l*D*aa2);
%%%%%%%%%%%%%%%%%%%%%%%%%%%%%%%% t0 t1
    %%%%%%%%%%%%%%%%%%%%%%%%%%%%%%%%%%%%
% Compute cnew t1, use cold, aiold as temporary variables for t0
% temp var necessary to make sure t array is dt to tn
% Initialize conc integral and Cf at all blocks
cnew{1} = zeros(length(x),length(y),length(z)); %cnew at t0
ainew{1} = zeros(length(x),length(y),length(z)); %this is ainew at
    t0
el = 1;
%%%%%%%%%%%%%%%%%%%%%%%%%%%%%%%%%%%%%%%%%%%%%%%%%%%%%%%%%%%%%%%%
% Compute at t1 to tn
for n = 2:length(t)
% Compute b at current timestep, all blocks, no parent-daughter***
% p = aC + b
btop = ainew{n-1} + A(n)*cnew{n-1}./(2*kappa*dt); %space dependent
bb2 = btop./bbot(n); %bb2 at t1
%Compute matrix diffusion terms, all blocks
anum2 = As*phi_l*tau_l*D*bb2;
errmax = 10; iter = 0;
%Initial guess of conc at current timestep
cnew{n} = cnew{n-1};
% Assign source conc to source cell
if t(n) > t1
cnew{n}(1,1:lysrc,lzsrcmin:lzsrcmax) = 0;
else %when time equal t1 or less
cnew{n}(1,1:lysrc,lzsrcmin:lzsrcmax) = czero;
end
%Start error loop
```

```
while errmax > tol
oldval = cnew{n};
iter = iter + 1;
for i = 2:length(x) %loop through all blocks at t1
for j = 1:length(y)
for k = 1:length(z)
%advection and storage term
anum1 = (Vd/Vf)*ayz*cnew{n}(i-1,j,k) + ...
(volh*phi_f*R/dt)*cnew{n-1}(i,j,k);
%storage, upstream weight and decay
%reset after each ijk
deno1 = volh*phi_f*R/dt + Vd*dy*dz + ...
volh*phi_f*lambda; %no zone remed
%vertical dispersion, no-flow at bottom and top
if 1 < k && k < nz
anum1 = anum1 + ...
(axy*phi_f*Dz/dz)*(cnew{n}(i,j,k-1) + ...
cnew{n}(i,j,k+1));
deno1 = deno1 + 2*Vf*phi_f*Dz*dx*dy/dz;
elseif k == 1 && nz == 1 %single block
anum1 = anum1 + 0; %no vertical dispersion
deno1 = deno1 + 0;
elseif k == 1 %no flow bottom
anum1 = anum1 + (axy*phi_f*Dz/dz)*cnew{n}(i,j,k+1);
deno1 = deno1 + Vf*phi_f*Dz*dx*dy/dz;
elseif k == nz %no flow top
anum1 = anum1 + (axy*phi_f*Dz/dz)*cnew{n}(i,j,k-1);
deno1 = deno1 + Vf*phi_f*Dz*dx*dy/dz;
end
%transverse dispersion
```

```
if 1 < j && j< ny
anum1 = anum1 + (phi_f*Dy*axz/dy)*...
(cnew{n}(i,j-1,k) + cnew{n}(i,j+1,k));
deno1 = deno1 + 2*Vf*phi_f*Dy*dx*dz/dy;
elseif j == 1 && ny == 1 %single block
anum1 = anum1 + 0; %no transverse dispersion
deno1 = deno1 + 0;
elseif j == 1
anum1 = anum1 + (phi_f*Dy*axz/dy)*cnew{n}(i,j+1,k);
deno1 = deno1 + Vf*phi_f*Dy*dx*dz/dy;
elseif j == ny %inf acting, outer conc = 0
anum1 = anum1 + (phi_f*Dy*axz/dy)*cnew{n}(i,j-1,k);
deno1 = deno1 + 2*Vf*phi_f*Dy*dx*dz/dy;
end
%longitudinal dispersion
if i < nx+1 %before last cell
anum1 = anum1 + (phi_f*Dx*ayz/dx)*...
(cnew{n}(i-1,j,k) + cnew{n}(i+1,j,k));
deno1 = deno1 + 2*Vf*phi_f*Dx*dy*dz/dx;
elseif i == nx+1 %inf acting, outer conc = 0
anum1 = anum1 + (phi_f*Dx*ayz/dx)*cnew{n}(i-1,j,k);
deno1 = deno1 + 2*Vf*phi_f*Dx*dy*dz/dx;
end
%add in matrix diffusion term
anum = anum1 + anum2(i,j,k);
denom = deno1 + deno2(n);
%Solve for cnew
cnew{n}(i,j,k) = anum/denom;
%cnew2{n,k} = cnew{n}(:,:,k);
end
```

```
end
end
errmax = max(max(max(abs(cnew{n} - oldval))));
end
% Compute p and q for ainew at current time
p2 = aa2(n)*cnew{n} + bb2;
qtop = (cnew{n} - cnew{n-1})*d(n)^2/(kappa*dt) - cnew{n} +...
2*d(n)*p2 + lambda_l*cnew{n}*d(n)^2./(Rl*kappa) + ...
(8*S*d(n)^2/As)*p2 - (8*S*d(n)/As)*cnew{n};
q2 = qtop./(2*d(n)^2);
% Compute new conc int, set Cf to C0
ainew{n} = deltpr(n)*cnew{n} + gampr(n)*p2 + betapr(n)*q2; %kg
% Separate to compile cnew, compute discharge, and mass
for i = 2:length(x) %skip x0 value
for j = 1:ny
for k = 1:nz
conc_my{el} = [t(n) x(i)-dx/2 y(j)-dy/2 z(k)-dz/2 ...
cnew{n}(i,j,k)];
el = el+1;
end
end
end
end
% Convert conc_my from cell to matrix
conc_my = conc_my(:); conc_my = cell2mat(conc_my);
% quick comparison of two conc tables
%abs(conc_rc(:,5) - conc_my(:,5))./conc_rc(:,5)*100;
%%%%%%%%%%%%%%%%%%%%%%%%%%%%%%%%%%%%%%%%%%%%%%%%%%%%%%%%
% 3D Mass Discharge Calcs for one block problem
dmdthk = conc_my(:,end)*dz*dy*Vd; %HK
```

```
dmdtsrc = czero*Vd*dy*dz;% Source mass flux from half model source
    block
dmdt_rc_on = dmdtsrc - dmdthk(2:(t1/dt)); % LK Mass Discharge - ON
dmdt_rc = [dmdt_rc_on; -dmdthk((t2/dt)+1:end)]; %ignore initial time
     data
tplot = [t_on(2:end)'; t_off(2:end)'];
% 3D Matrix mass for one block problem
ainew2 = cell2mat(ainew); ainew2 = ainew2(2,2:end); %remove ainew at
     x0,t0
mass_rc = As*phi_l*Rl*ainew2;
%% Export mass and mass discharge data for series plotting
save(['massRC_thalf=' num2str(thalf_l) 'yrs_Rl=' num2str(Rl)...
'_run' num2str(rcruns) '.txt'],'mass_rc','-ascii','-double');
save(['dmdtRC_thalf=' num2str(thalf_l) 'yrs_Rl=' num2str(Rl)...
'_run' num2str(rcruns) '.txt'],'dmdt_rc','-ascii','-double');
toc;
%% 1D Mass Discharge for one block problem
dmdthk1d = raw_dmdt_rc(:,3)./2;
dmdt_1drc_on = dmdtsrc - dmdthk1d(2:(t1/dt));
dmdt_1drc = [dmdt_1drc_on; -dmdthk1d((t2/dt)+1:end)];
mass1d = raw_mass_rc(:,2)./2;
%% Export 1d mass and mass discharge data for series plotting
save(['massRC1d_thalf=' num2str(thalf_l) 'yrs_Rl=' num2str(Rl)...
'_run' num2str(rcruns) '.txt'],'mass1d','-ascii','-double');
save(['dmdtRC1d_thalf=' num2str(thalf_l) 'yrs_Rl=' num2str(Rl)...
'_run' num2str(rcruns) '.txt'],'dmdt_1drc','-ascii','-double');
%% Plotting
% Compute quick NRMSE for 3D & 1D SA
rmse_dmdt_rc = sqrt( mean( (dmdt_rc - dmdt3d').^2 ) );
rmse_dmdt_1drc = sqrt( mean( (dmdt_1drc - dmdt3d').^2 ) );
```

```
rnmse_mass_rc = sqrt( mean( (mass_rc - mass3d).^2 ) );
rnmse_mass_1drc = sqrt( mean( (mass1d - mass3d').^2 ) );
% normalized by largest dmdt3d
nrmse_dmdt_rc = rmse_dmdt_rc*100/(max(dmdt3d));
nrmse_dmdt_1drc = rmse_dmdt_1drc*100/(max(dmdt3d));
nrmse_mass_rc = rnmse_mass_rc*100/(czero*phi_l*Rl*Vl*(1-Vf));
nrmse_mass_1drc = rnmse_mass_1drc*100/(czero*phi_l*Rl*Vl*(1-Vf));
% Start plotting
close all;
figure;
plot(tplot,dmdt3d,'ko','displayname','Analytical'); hold on;
plot(tplot,dmdt_rc,'-.','color','#77AC30',...
'displayname',...
['3D Semi-analytical, (' num2str(round(nrmse_dmdt_rc,2,'significant'
   )) '% error)'],...
'linewidth',1.5);
plot(tplot,dmdt_1drc,'DisplayName',...
['1D Semi-analytical, (' num2str(round(nrmse_dmdt_1drc,2,...
'significant')) '% error)'],'LineWidth',1.5);
grid on; grid minor; legend; hold off;
xlabel('Time, years'); ylabel('Matrix Mass Discharge, kg/yr');
```

Appendix B

Analytical solution for 3-D matrix block

```
%%%%%%%%%%%%%%%%%%%%%%%%%%%%%%%% INPUTS
    %%%%%%%%%%%%%%%%%%%%%%%%%%%%%%%%%%%%
% half dimensions of matrix block per ana sol
abc = [2.5 2.5 2.5];
a = abc(1); b = abc(2); c = abc(3);
rcruns = 70702;
%Time inputs
thalf = 1e6; %years
dt_3d = 1; t_on_end = 50; t_off_end = 100;
%Infinite series input
inf_end = 40; %need to optimize time for 30 terms, 101010 case
%water properties
%Units: D - m2/yr, C0 - g/l or kg/m3, R,phi,tau - unitless, Vpf - m/
    yr
D = 0.0315576; C0 = 0.1; %Vpf = 100;
tau_l = 0.1; R_l = 1; phi_l = 0.1;
%Conc inputs
```

```
C0 = 0.1; %kg/m3
%%%%%%%%%%%%%%%%%%%%%%%%%%%%%% COMPUTE
    %%%%%%%%%%%%%%%%%%%%%%%%%%%%%%%%%%%%%%%%
%Compute half volume for use in ana sol
V = a.*b.*c;
%Compute t array
t_on = dt_3d:dt_3d:t_on_end;
t_off = t_on(end)+dt_3d:dt_3d:t_off_end;
t_3d = [t_on';t_off'];
%decay rate, 1/yr
decaym = log(2)./thalf; %same as RC input
%Compute l,m,n for infinite series
l = 0:inf_end; m = 0:inf_end; n = 0:inf_end;
kappa = D*tau_l/R_l; %m2/yr
%%Compute infi arrays
[L,M,N] = meshgrid(l,m,n); L = L(:); M = M(:); N = N(:);
tab_lmn = [L,M,N];
% Matrix Mass ON
alpha = (pi^2*kappa/4)*( ((2*L+1)./a).^2+((2*M+1)./b).^2+((2*N+1)./c
    ).^2 );
deno = ( (2*L+1).^2.*(2*M+1).^2.*(2*N+1).^2 );
% Begin computing analytical solution
eterm = ( decaym + ...
alpha.*exp( -t_on.*(decaym + alpha) ) )./...
(decaym + alpha);
masstermsON = eterm./deno;
massON = C0*phi_l*R_l*V*(8 - (64/pi^3)^2*sum(masstermsON,1));
dmdttermsON = alpha.*masstermsON;
dmdtON = (64/pi^3)^2*C0*phi_l*R_l*V*(sum(dmdttermsON,1));
% Matrix Mass OFF
```

```
eterm2 = ( decaym + ...
alpha.*exp( -(t_off - t_on_end).*(decaym + alpha) ) )./...
(decaym + alpha);
masstermsOFF1 = eterm2./deno;
eterm3 = ( decaym + ...
alpha.*exp( -t_off.*( decaym + alpha ) ) )./...
(decaym + alpha);
masstermsOFF2 = eterm3./deno;
massOFF = (64/pi^3)^2*C0*phi_l*R_l*V*...
(sum(masstermsOFF1,1) - sum(masstermsOFF2,1));
% Discharge OFF
dmdtOFF = (64/pi^3)^2*C0*phi_l*R_l*V.*...
(sum(alpha.*masstermsOFF2,1) - ...
sum(alpha.*masstermsOFF1,1));
% Tabulate
mass3d = [massON, massOFF];
dmdt3d = [dmdtON(2:end), dmdtOFF(2:end)];
toc;
%% save results for a single case
save(['mass3d_thalf=' num2str(thalf) 'yrs_Rl=' num2str(R_l)...
'_run' num2str(rcruns) '.txt'],'mass3d','-ascii','-double');
save(['dmdt3d_thalf=' num2str(thalf) 'yrs_Rl=' num2str(R_l)...
'_run' num2str(rcruns) '.txt'],'dmdt3d','-ascii','-double');
```

Bibliography

Non-software Sources

Adams, E. E., & Gelhar, L. W. (1992). Field study of dispersion in a heterogeneous aquifer: 2. spatial moments analysis. *Water Resources Research*, *28*, 3293–3307. https://doi.org/10.1029/92wr01757

Allwright, A., & Atangana, A. (2018). Fractal advection-dispersion equation for groundwater transport in fractured aquifers with self-similarities. *European Physical Journal Plus*, *133*(2), 1–20. https://doi.org/10.1140/epjp/i2018-11885-3

Allwright, A., & Atangana, A. (2019). Upwind-based numerical approximation of a space-time fractional advection-dispersion equation for groundwater transport within fractured systems. Springer International Publishing. https://doi.org/10.1007/978-3-030-11662-0_18

Allwright, A., Atangana, A., & Mekkaoui, T. (2021). Fractional and fractal advection-dispersion model. *Discrete and Continuous Dynamical Systems - Series S*, *14*(7), 2055–2074. https://doi.org/10.3934/dcdss.2021061

Anderson, M. P. (1992). *Applied groundwater modeling*. Academic Press Inc.

Ball, W. P., Liu, C., Xia, G., & Young, D. F. (1997). A diffusion-based interpretation of tetrachloroethene and trichloroethene concentration profiles in a groundwater aquitard. *Water Resources Research*, *33*, 2741–2757. https://doi.org/10.1029/97wr02135

Barenblatt, G. I., Zheltov, I. P., & Kochina, I. N. (1960). Basic concepts in the theory of seepage of homogeneous liquids in fissured rocks [strata]. *Journal of Applied Mathematical Mechanics*, *24*, 1286–1303. https://doi.org/10.1016/0021-8928(60)90107-6

Bear, J., & Cheng, A. H.-D. (2010). *Modeling groundwater flow and contaminant transport* (First). Springer Dordrecht. https://doi.org/10.1007/978-1-4020-6682-5

Berkowitz, B., Bear, J., & Braester, C. (1988). Continuum models for contaminant transport in fractured porous formations. *Water Resources Research*, *24*, 1225–1236. https://doi.org/10.1029/wr024i008p01225

Blessent, D., Therrien, R., & MacQuarrie, K. (2009). Coupling geological and numerical models to simulate groundwater flow and contaminant transport in fractured media. *Comput Geosci*, *35*, 1897–1906. https://doi.org/10.1016/j.cageo.2008.12.008

Boggs, J. M., & Adams, E. E. (1992). Field study of dispersion in a heterogeneous aquifer: 4. investigation of adsorption and sampling bias. *Water Resources Research*, *28*, 3325–3336. https://doi.org/10.1029/92wr01759

Boggs, J. M., Young, S. C., Beard, L. M., Gelhar, L. W., Rehfeldt, K. R., & Adams, E. E. (1992). Field study of dispersion in a heterogeneous aquifer: 1. overview and site description. *Water Resources Research*, *28*, 3281–3291. https://doi.org/10.1029/92wr01756

Carslaw, H. S., & Jaeger, J. C. (1959). *Conduction of heat in solids* (Second). Clarendon Press.

Chapman, S. W., & Parker, B. L. (2005). Plume persistence due to aquitard back diffusion following dense nonaqueous phase liquid source removal or isolation. *Water Resources Research*, *41*(12), W12411. https://doi.org/10.1029/2005wr004224

Chapman, S. W., Parker, B. L., Sale, T. C., & Doner, L. A. (2012). Testing high resolution numerical models for analysis of contaminant storage and release from low permeability zones. *Journal of Contaminant Hydrology*, *136-137*, 106–116. https://doi.org/10.1016/j.jconhyd.2012.04.006

Coats, K. H., & Smith, B. D. (1964). Dead-end pore volume and dispersion in porous media. *Society of Petroleum Engineers*, *4*, 73–84. https://doi.org/10.2118/647-pa

Corless, R. M., Gonnet, G. H., Hare, D. E. G., Jeffrey, D. J., & Knuth, D. E. (1996). On the LambertW function. *Advances in Computational Mathematics*, *5*(1), 329–359. https://doi.org/10.1007/BF02124750

Crank, J. (1975). *The mathematics of diffusion*. Clarendon Press.

Deans, H. A. (1963). A mathematical model for dispersion in the direction of flow in porous media. *Society of Petroleum Engineers*, *3*, 49–52. https://doi.org/10.2118/493-pa

de Vries, E. T., Raoof, A., & van Genuchten, M. T. (2017). Multiscale modelling of dual-porosity porous media; a computational pore-scale study for flow and solute transport. *Advances in Water Resources*, *105*, 82–95. https://doi.org/10.1016/j.advwatres.2017.04.013

Endo, H. K., Long, J. C. S., Wilson, C. R., & Witherspoon, P. A. (1984). A model for investigating mechanical transport in fracture networks. *Water Resources Research*, *20*, 1390–1400. https://doi.org/10.1029/wr020i010p01390

Esposito, S. J., & Thomson, N. R. (1999). Two-phase flow and transport in a single fracture-porous medium system. *Journal of Contaminant Hydrology*, *37*, 319–341. https://doi.org/10.1016/s0169-7722(98)00169-7

Falta, R. W. (2005). Dynamics of fluids and transport in fractured rock. John Wiley & Sons Limited. https://doi.org/10.1029/162gm15

Falta, R. W., & Wang, W. (2017). A semi-analytical method for simulating matrix diffusion in numerical transport models. *Journal of Contaminant Hydrology*, *197*, 39–49. https://doi.org/10.1016/j.jconhyd.2016.12.007

Farhat, S. K., Adamson, D. T., Gavaskar, A. R., Lee, S. A., Falta, R. W., & Newell, C. J. (2020). Vertical discretization impact in numerical modeling of matrix diffusion in contaminated groundwater. *Groundwater Monitoring and Remediation*, *40*(2), 52–64. https://doi.org/10.1111/gwmr.12373

Feehley, C. E., Zheng, C., & Molz, F. J. (2000). A dual-domain mass transfer approach for modeling solute transport in heterogeneous aquifers: Application to the Macrodispersion Experiment (MADE) site. *Water Resources Research*, *36*, 2501–2515. https://doi.org/10.1029/2000wr900148

Filippini, M., Parker, B. L., Dinelli, E., Wanner, P., Chapman, S. W., & Gargini, A. (2020). Assessing aquitard integrity in a complex aquifer – aquitard system contaminated by chlorinated hydrocarbons. *Water Research*, *171*, 115388. https://doi.org/10.1016/j.watres.2019.115388

Foster, S. S. D. (1975). The Chalk groundwater tritium anomaly – A possible explanation. *J Hydrol*, *25*(1-2), 159–165. https://doi.org/10.1016/0022-1694(75)90045-1

Freeze, R. A., & Cherry, J. A. (1979). *Groundwater*. Prentice-Hall.

Gillham, R. W., Sudicky, E. A., Cherry, J. A., & Frind, E. O. (1984). An advection-diffusion concept for solute transport in heterogeneous unconsolidated geological deposits. *Water Resources Research*, *20*(3), 369–378. https://doi.org/10.1029/WR020i003p00369

Goltz, M. N., & Roberts, P. V. (1987). Using the method of moments to analyze three–dimensional diffusion-limited solute transport from temporal and spatial perspectives. *Water Resources Research*, *23*(8), 1575–1585. https://doi.org/10.1029/WR023i008p01575

Grisak, G. E., & Pickens, J. F. (1980). Solute transport through fractured media: 1. the effect of matrix diffusion. *Water Resources Research*, *16*(4), 719–730. https://doi.org/10.1029/WR016i004p00719

Guan, J., Molz, F. J., Zhou, Q., Liu, H. H., & Zheng, C. (2008). Behavior of the mass transfer coefficient during the MADE-2 experiment: New insights. *Water Resources Research*, *44*, W02423. https://doi.org/10.1029/2007wr006120

Hadgu, T., Karra, S., Kalinina, E., Makedonska, N., Hyman, J. D., Klise, K., Viswanathan, H. S., & Wang, Y. (2017). A comparative study of discrete fracture network and equivalent continuum models for simulating flow and transport in the far field of a hypothetical nuclear waste repository in crystalline host rock. *Journal of Hydrology*, *553*, 59–70. https://doi.org/10.1016/j.jhydrol.2017.07.046

Hadley, P. W., & Newell, C. J. (2014). The new potential for understanding groundwater contaminant transport. *Groundwater*, *52*, 656–658. https://doi.org/10.1111/gwat.12246

Haggerty, R., & Gorelick, S. M. (1995). Multiple-rate mass transfer for modeling diffusion and surface reactions in media with pore-scale heterogeneity. *Water Resources Research*, *31*, 2383–2400. https://doi.org/10.1029/95wr10583

Herrera-Hernández, E. C., Aguilar-Madera, C. G., Hernández, D., Luis, D. P., & Camacho-Velázquez, R. G. (2018). Semi-numerical solution to a fractal telegraphic dual-porosity fluid flow model. *Computational and Applied Mathematics*, *37*(4), 4342–4356. https://doi.org/10.1007/s40314-018-0577-7

Huyakorn, P. S., Lester, B. H., & Mercer, J. W. (1983). An efficient finite element technique for modeling transport in fractured porous media: 1. single species transport. *Water Resources Research*, *19*, 841–854. https://doi.org/10.1029/wr019i003p00841

Hyman, J. D., Karra, S., Makedonska, N., Gable, C. W., Painter, S. L., & Viswanathan, H. S. (2015). dfnWorks: A discrete fracture network framework for modeling subsurface flow and transport. *Comput Geosci*, *84*, 10–19. https://doi.org/10.1016/j.cageo.2015.08.001

Keller, C. K., van der Kamp, G., & Cherry, J. A. (1986). Fracture permeability and groundwater flow in clayey till near Saskatoon, Saskatchewan. *Canadian Geotechnology Journal*, *23*(2), 229–240. https://doi.org/10.1139/t86-032

Keller, C. E., Cherry, J. A., & Parker, B. L. (2014). New method for continuous transmissivity profiling in fractured rock. *Groundwater*, *52*, 352–367. https://doi.org/10.1111/gwat.12064

Khuzhayorov, B., Usmonov, A., Long, N. M. A. N., & Fayziev, B. (2020). Anomalous solute transport in a cylindrical two-zone medium with fractal structure. *Applied Sciences*, *10*(15), 53491–53509. https://doi.org/10.3390/app10155349

Kulkarni, P. R., Adamson, D. T., Popovic, J., & Newell, C. J. (2022). Modeling a well-characterized perfluorooctane sulfonate (PFOS) source and plume using the REMChlor-MD model to account for matrix diffusion. *Journal of Contaminant Hydrology*, *247*, 103986. https://doi.org/10.1016/j.jconhyd.2022.103986

Li, X., Li, D., Xu, Y., & Feng, X. (2020). A DFN based 3D numerical approach for modeling coupled groundwater flow and solute transport in fractured rock mass. *International Journal of Heat and Mass Transfer*, *149*, 119179. https://doi.org/10.1016/j.ijheatmasstransfer.2019.119179

Liao, Z.-Y., Suk, H., Liu, C.-W., Liang, C.-P., & Chen, J.-S. (2021). Exact analytical solutions with great computational efficiency to three-dimensional multispecies advection-dispersion equations coupled with a sequential first-order reaction network. *Advances in Water Resources*, *155*, 104018. https://doi.org/10.1016/j.advwatres.2021.104018

Liu, C., & Ball, W. P. (1998). Analytical modeling of diffusion-limited contamination and decontamination in a two-layer porous medium. *Advances in Water Resources*, *21*, 297–313. https://doi.org/10.1016/s0309-1708(96)00062-0

Liu, C., & Ball, W. P. (2002). Back diffusion of chlorinated solvent contaminants from a natural aquitard to a remediated aquifer under well-controlled field conditions: Predictions and measurements. *Ground Water*, *40*(2), 175–184. https://doi.org/10.1111/j.1745-6584.2002.tb02502.x

Liu, L., Neretnieks, I., Shahkarami, P., Meng, S., & Moreno, L. (2018). Solute transport along a single fracture in a porous rock: A simple analytical solution and its extension for modeling velocity dispersion. *Hydrogeology Journal*, *26*, 297–320. https://doi.org/10.1007/s10040-017-1627-8

Long, J. C. S., Remer, J. S., Wilson, C. R., & Witherspoon, P. A. (1982). Porous media equivalents for networks of discontinuous fractures. *Water Resources Research*, *18*(3), 645–658. https://doi.org/10.1029/wr018i003p00645

Mackay, D. M., & Cherry, J. A. (1989). Groundwater contamination: Pump-and-treat remediation. *Environ Sci Technol*, *23*(6), 630–636. https://doi.org/10.1021/es00064a001

McKay, L. D., Gillham, R. W., & Cherry, J. A. (1993). Field experiments in a fractured clay till: 2. solute and colloid transport. *Water Resources Research*, *29*, 3879–3890. https://doi.org/10.1029/93wr02069

Molins, S., Trebotich, D., Arora, B., Steefel, C. I., & Deng, H. (2019). Multi-scale model of reactive transport in fractured media: Diffusion limitations on rates. *Transport in Porous Media*, *128*, 701–721. https://doi.org/10.1007/s11242-019-01266-2

Munson, B. R., Young, D. F., Okiishi, T. H., & Huebsch, W. W. (2009). *Fundamentals of fluid mechanics* (Sixth). Don Fowley.

Muskus, N., & Falta, R. W. (2018). Semi-analytical method for matrix diffusion in heterogeneous and fractured systems with parent-daughter reactions. *Journal of Contaminant Hydrology*, *218*, 94–109. https://doi.org/10.1016/j.jconhyd.2018.10.002

Neretnieks, I. (1980). Diffusion in the rock matrix: An important factor in radionuclide retardation? *Journal of Geophysical Research*, *85*(B8), 4379–4397. https://doi.org/10.1029/JB085iB08p04379

Ngo, T. D., Fourno, A., & Noetinger, B. (2017). Modeling of transport processes through large-scale discrete fracture networks using conforming meshes and open-source software. *IFPEN - IFP Energies nouvelles*, *554*, 66–79. https://doi.org/10.1016/j.jhydrol.2017.08.052

O'Hara, S. K., Parker, B. L., Jørgensen, P. R., & Cherry, J. A. (2000). Trichloroethene DNAPL flow and mass distribution in naturally fractured clay: Evidence of aperture variability. *Water Resources Research*, *36*, 135–147. https://doi.org/10.1029/1999wr900212

Panday, S., Huyakorn, P. S., Therrien, R., & Nichols, R. L. (1993). Improved three-dimensional finite-element techniques for field simulation of variably saturated flow and transport. *Journal of Contaminant Hydrology*, *12*, 3–33. https://doi.org/10.1016/0169-7722(93)90013-i

Pankow, J. F., Johnson, R. L., Hewetson, J. P., & Cherry, J. A. (1986). An evaluation of contaminant migration patterns at two waste disposal sites on fractured porous media in terms of the equivalent porous medium (EPM) model. *Journal of Contaminant Hydrology*, *1*(1), 65–76. https://doi.org/10.1016/0169-7722(86)90007-0

Parker, B. L., Chapman, S. W., & Guilbeault, M. A. (2008). Plume persistence caused by back diffusion from thin clay layers in a sand aquifer following TCE source-zone hydraulic isolation. *Journal of Contaminant Hydrology*, *102*, 86–104. https://doi.org/10.1016/j.jconhyd.2008.07.003

Parker, B. L., Cherry, J. A., & Chapman, S. W. (2012). Discrete fracture network approach for studying contamination in fractured rock. *AQUA mundi*, *3*(2), 101–116.

Parker, B. L., Cherry, J. A., & Chapman, S. W. (2004). Field study of TCE diffusion profiles below DNAPL to assess aquitard integrity. *Journal of Contaminant Hydrology*, *74*, 197–230. https://doi.org/10.1016/j.jconhyd.2004.02.011

Parker, B. L., Gillham, R. W., & Cherry, J. A. (1994). Diffusive disappearance of immiscible-phase organic liquids in fractured geologic media. *Ground Water*, *32*(5), 805–820. https://doi.org/10.1111/j.1745-6584.1994.tb00922.x

Parker, B. L., McWhorter, D. B., & Cherry, J. A. (1997). Diffusive loss of non-aqueous phase organic solvents from idealized fracture networks in geologic media. *Ground Water*, *35*(6), 1077–1088. https://doi.org/10.1111/j.1745-6584.1997.tb00180.x

Parker, J. C., & Valocchi, A. J. (1986). Constraints on the validity of equilibrium and first-order kinetic transport models in structured soils. *Water Resources Research*, *22*(3), 399–407. https://doi.org/10.1029/WR022i003p00399

Perina, T. (2022). Semi-analytical model for solute transport in a three-dimensional aquifer with dual porosity and a volumetric source term. *Journal of Hydrology*, *607*, 127520. https://doi.org/10.1016/j.jhydrol.2022.127520

Pham, K. T., & Falta, R. W. (2022). Use of semi-analytical and dual-porosity models for simulating matrix diffusion in systems with parallel fractures. *Advances in Water Resources*, *164*, 104202. https://doi.org/10.1016/j.advwatres.2022.104202

Pierce, A. A., Chapman, S. W., Zimmerman, L. K., Hurley, J. C., Aravena, R., Cherry, J. A., & Parker, B. L. (2018). DFN-M field characterization of sandstone for a process-based site conceptual model and numerical simulations of TCE transport with degradation. *Journal of Contaminant Hydrology*, *212*(100), 96–114. https://doi.org/10.1016/j.jconhyd.2018.03.001

Powers, D. L. (1979). *Boundary value problems* (Second). Academic Press.

Pruess, K. (1985). A practical method for modeling fluid and heat flow in fractured porous media. *Society of Petroleum Engineers Journal*, *25*(1), 14–26. https://doi.org/10.2118/10509-PA

Pruess, K., & Wu, Y.-S. (1988). A semi-analytical method for heat sweep calculations in fractured reservoirs. *13th Workshop on Geothermal Reservoir Engineering*, 24463. https://www.osti.gov/biblio/5062388

Pruess, K., & Wu, Y.-S. (1993). A new semi-analytical method for numerical simulation of fluid and heat flow in fractured reservoirs [Advanced Technology Series]. *Society of Petroleum Engineers*, *1*(2), 63–72. https://doi.org/10.2118/18426-PA

Quinn, P. M., Parker, B. L., & Cherry, J. A. (2011). Using constant head step tests to determine hydraulic apertures in fractured rock. *Journal of Contaminant Hydrology*, *126*, 85–99. https://doi.org/10.1016/j.jconhyd.2011.07.002

Rao, P. S. C., Rolston, D. E., Jessup, R. E., & Davidson, J. M. (1980). Solute transport in aggregated porous media: Theoretical and experimental evaluation. *Soil Science Society of America Journal*, *44*, 1139–1146. https://agris.fao.org/agris-search/search.do?recordID=US19810643426

Rasa, E., Chapman, S. W., Bekins, B. A., Fogg, G. E., Scow, K. M., & Mackay, D. M. (2011). Role of back diffusion and biodegradation reactions in sustaining an MTBE/TBA plume in alluvial media. *Journal of Contaminant Hydrology*, *126*, 235–247. https://doi.org/10.1016/j.jconhyd.2011.08.006

Rasmuson, A. (1984). Migration of radionuclides in fissured rock: Analytical solutions for the case of constant source strength. *Water Resources Research*, *20*(10), 1435–1442. https://doi.org/10.1029/WR020i010p01435

Roubinet, D., de Dreuzy, J.-R., & Tartakovsky, D. M. (2012). Semi-analytical solutions for solute transport and exchange in fractured porous media. *Water Resources Research*, *48*, W01542. https://doi.org/10.1029/2011wr011168

Sale, T. C., Zimbron, J. A., & Dandy, D. S. (2008). Effects of reduced contaminant loading on downgradient water quality in an idealized two-layer granular porous media. *Journal of Contaminant Hydrology*, *102*(1), 72–85. https://doi.org/10.1016/j.jconhyd.2008.08.002

Schwartz, F. W., & Smith, L. (1988). A continuum approach for modeling mass transport in fractured media. *Water Resources Research*, *24*(8), 1360–1372. https://doi.org/10.1029/wr024i008p01360

Schwartz, F. W., Smith, L., & Crowe, A. S. (1983). A stochastic analysis of macroscopic dispersion in fractured media. *Water Resources Research*, *19*, 1253–1265. https://doi.org/10.1029/wr019i005p01253

Seyedabbasi, M. A., Newell, C. J., Adamson, D. T., & Sale, T. C. (2012). Relative contribution of DNAPL dissolution and matrix diffusion to the long-term persistence of chlorinated solvent

source zones. *Journal of Contaminant Hydrology*, *134-135*, 69–81. https://doi.org/10.1016/j.jconhyd.2012.03.010

Singh, V. P., Jain, S. K., & Tyagi, A. K. (2007). *Risk and reliability analysis*. American Society of Civil Engineers. https://doi.org/10.1061/9780784408919

Starr, R. C., Gillham, R. W., & Sudicky, E. A. (1985). Experimental investigation of solute transport in stratified porous media: 2. the reactive case. *Water Resources Research*, *21*, 1043–1050. https://doi.org/10.1029/wr021i007p01043

Sudicky, E. A., & Frind, E. O. (1982). Contaminant transport in fractured porous media: Analytical solutions for a system of parallel fractures. *Water Resources Research*, *18*(6), 1634–1642. https://doi.org/10.1029/WR018i006p01634

Sudicky, E. A., Gillham, R. W., & Frind, E. O. (1985). Experimental investigation of solute transport in stratified porous media: 1. the nonreactive case. *Water Resources Research*, *21*, 1035–1041. https://doi.org/10.1029/wr021i007p01035

Sudicky, E. A., & McLaren, R. G. (1992). The Laplace Transform Galerkin Technique for large-scale simulation of mass transport in discretely fractured porous formations. *Water Resources Research*, *28*(2), 499–514. https://doi.org/10.1029/91WR02560

Swami, D., Sharma, P. K., Ojha, C. S. P., Guleria, A., & Sharma, A. (2018). Asymptotic behavior of mass transfer for solute transport through stratified porous medium. *Transport in Porous Media*, *124*, 699–721. https://doi.org/10.1007/s11242-018-1090-6

Tang, D. H., Frind, E. O., & Sudicky, E. A. (1981). Contaminant transport in fractured porous media: Analytical solution for a single fracture. *Water Resources Research*, *17*, 555–564. https://doi.org/10.1029/wr017i003p00555

Therrien, R., & Sudicky, E. A. (1996). Three-dimensional analysis of variably-saturated flow and solute transport in discretely-fractured porous media. *Journal of Contaminant Hydrology*, *23*(1-2), 1–44. https://doi.org/10.1016/0169-7722(95)00088-7

Toran, L. (2000). CRAFIT: A computer program for calibrating breakthrough curves of CRAFLUSH, a one-dimensional fracture flow and transport model. *Ground Water*, *38*(3), 430–434. https://doi.org/10.1111/j.1745-6584.2000.tb00229.x

Trinchero, P., Painter, S. L., Poteri, A., Sanglas, J., Cvetkovic, V., & Selroos, J.-O. (2020). A particle-based conditional sampling scheme for the simulation of transport in fractured rock with diffusion into stagnant water and rock matrix. *Water Resources Research*, *56*(4), e2019WR026958. https://doi.org/10.1029/2019wr026958

van Genuchten, M. T. (1985). A general approach for modeling solute transpot in structured soils. *Proc. 17th International Congress*, *17 (2)*, 513–526.

Vinsome, P. K. W., & Westerveld, J. (1980). A simple method for predicting cap and base rock heat losses in thermal reservoir simulators. *Journal of Canadian Petroleum Technology*, *19*. https://doi.org/10.2118/80-03-04

Xu, P., Li, C., Qiu, S., & Sasmito, A. P. (2016). A fractal network model for fractured porous media. *Fractals*, *24*(2), 1650018. https://doi.org/10.1142/S0218348X16500183

Xu, P., Liu, H., Sasmito, A. P., Qiu, S., & Li, C. (2017). Effective permeability of fractured porous media with fractal dual-porosity model. *Fractals*, *25*(4), 1740014. https://doi.org/10.1142/S0218348X1740014X

Yang, M., Annable, M. D., & Jawitz, J. W. (2015). Back diffusion from thin low permeability zones. *Environ Sci Technol*, *49*, 415–422. https://doi.org/10.1021/es5045634

Yang, M., Annable, M. D., & Jawitz, J. W. (2017). Field-scale forward and back diffusion through low-permeability zones. *Journal of Contaminant Hydrology*, *202*, 47–58. https://doi.org/10.1016/j.jconhyd.2017.05.001

Yang, M., McCurley, K. L., Annable, M. D., & Jawitz, J. W. (2019). Diffusion of solutes from depleting sources into and out of finite low-permeability zones. *Journal of Contaminant Hydrology*, *221*, 127–134. https://doi.org/10.1016/j.jconhyd.2019.01.005

Yates, S. R. (1990). An analytical solution for one-dimensional transport in heterogeneous porous media. *Water Resources Research*, *26*, 2331–2338. https://doi.org/10.1029/wr026i010p02331

Zheng, C., & Bennett, G. D. (2002). *Applied contaminant transport modeling* (Second). Wiley-Interscience.

Software

Aquanty Inc. (2021). HydroGeoSphere - Integrated Hydrologic Models. https://www.aquanty.com/hydrogeosphere

Aquaveo. (2019). Groundwater Modeling System - GMS 10.4.2. https://www.aquaveo.com/software/gms-groundwater-modeling-system-introduction

Carle, S. F. (1999). *T-PROGS: Transition Probability Geostatistical Software - Version 2.1*. University of California, Davis. Lawrence Livermore National Laboratory, L-206, P.O. Box 808, Livermore, CA 94551. https://www.aquaveo.com/software/gms-tprogs

Chapman, S. W. (2021). Subject: Recreating DFN Model in 2018 Paper.

Farhat, S. K., Newell, C. J., Falta, R. W., & Lynch, K. (2018). User's Manual: A practical approach for modeling matrix diffusion effects in REMChlor. *SERDP ESTCP*. https://www.serdp-estcp.org/Program-Areas/Environmental-Restoration/Contaminated-Groundwater/Persistent-Contamination/ER-201426/ER-201426

Farhat, S. K., Newell, C. J., Sale, T. C., Dandy, D. S., Wahlberg, J. J., Seyeddabbasi, M. A., McDade, J. M., & Mahler, N. T. (2012). Matrix Diffusion Toolkit, developed for the Environmental Security Technology Certification Program (ESTCP). https://www.serdp-estcp.org/Tools-and-Training/Environmental-Restoration/Groundwater-Plume-Treatment/Matrix-Diffusion-Tool-Kit

Harbaugh, A. W. (2005). MODFLOW-2005: The U.S. Geological Survey modular ground-water model—the ground-water flow process. https://www.usgs.gov/software/modflow-2005-usgs-three-dimensional-finite-difference-ground-water-model

Tecplot Inc. (2020). Tecplot 360. https://www.tecplot.com/products/tecplot-360/

Walton, K. M. (2021). 2D and 3D Random Fracture Generators. https://community.aquanty.com/topic/674/2d-and-3d-random-fracture-generators/4

Zheng, C., & Wang, P. P. (1999). A modular three-dimensional multispecies transport model (MT3DMS) for simulation of advection, dispersion and chemical reactions of contaminants in groundwater systems. https://hydro.geo.ua.edu/mt3d/index.htm